ABSTRACT

STUDY OF MAGNETIC HELICITY IN SOLAR ACTIVE REGIONS AND ITS RELATIONSHIP WITH SOLAR ERUPTIONS

by
Sung-Hong Park

It is generally believed that eruptive phenomena in the solar atmosphere such as solar flares and coronal mass ejections (CMEs) occur in solar active regions with complex magnetic structures. The magnetic complexity is quantified in terms of twists, kinks, and interlinkages of magnetic field lines. Magnetic helicity has been recognized as a useful measure for these properties of a given magnetic field system. Magnetic helicity studies have been naturally directed to the energy buildup and instability leading to solar eruptions. However, in spite of many years of study, detailed aspects of initiation mechanisms of eruptive events are still not well understood. The objective of this dissertation is to understand a long-term (a few days) variation of magnetic helicity in active regions and its relationship with flares and CMEs.

The research presented in this dissertation benefited significantly from the comprehensive data now available, including *SOHO*/MDI full-disk longitudinal magnetograms, *Hinode*/SOT/SP vector magnetograms, and *GOES* soft X-ray data. In addition, several advanced data analysis tools were utilized such as local correlation tracking, differential affine velocity estimator, Stokes inversion, 180° ambiguity resolution, and nonlinear force-free magnetic field extrapolation. Statistical studies of flare productivity and magnetic helicity injection in ∼400 active regions were carried out. The time profile of the coronal magnetic helicity in the active region NOAA 10930 was also investigated to find its characteristic variation related to the X3.4 flare on 2006 December 13. In addition, the temporal varia-

tion of magnetic helicity injected through the photosphere of active regions was examined related to 46 CMEs and two active-region coronal arcades building up to CMEs.

The main findings in this dissertation are as follows: (1) the study of magnetic helicity for active regions producing major flares and CMEs indicates that there is always a significant helicity injection of 10^{42}–10^{43} Mx^2 through the active-region photosphere over a long period of $\sim$0.5–a few days before the flares and CMEs; (2) the study of the 2006 December 13 X3.4 flare shows that the flare is preceded by not only a large increase of negative helicity in the corona over $\sim$1.5 days but also a noticeable injection of oppositely-signed helicity though the photospheric surface around the flaring magnetic polarity inversion line; (3) the gradual inflation stage of the two arcades is temporally associated with helicity injection from the active-region photosphere; and (4) for the 30 CMEs under investigation, it is found that there is a fairly good correlation (linear correlation coefficient of 0.71) between the average helicity injection in the CME-productive active regions and the CME speed.

Beside the scientific contribution, a major broader impact of this dissertation is the observational discovery of a characteristic variation of the pattern of magnetic helicity injection in flare/CME-productive active regions, which can be used for the improvement of solar eruption forecasting. An early warning sign of flare-CME occurrence could be implemented based on tracking of a period of monotonically increasing helicity because there was always a significant amount of helicity accumulation in active regions a few days before the major flares and CMEs under investigation.

STUDY OF MAGNETIC HELICITY IN SOLAR ACTIVE REGIONS AND ITS RELATIONSHIP WITH SOLAR ERUPTIONS

by
Sung-Hong Park

A Dissertation
Submitted to the Faculty of
New Jersey Institute of Technology and
Rutgers, the State University of New Jersey - Newark
in Partial Fulfillment of the Requirements for the Degree of
Doctor of Philosophy in Applied Physics

Federated Physics Department

August 2010

APPROVAL PAGE

STUDY OF MAGNETIC HELICITY IN SOLAR ACTIVE REGIONS AND ITS RELATIONSHIP WITH SOLAR ERUPTIONS

Sung-Hong Park

Dr. Haimin Wang, Dissertation Co-Advisor — Date
Distinguished Professor of Physics, Director of Space Weather Research Laboratory, NJIT

Dr. Wenda Cao, Dissertation Co-Advisor — Date
Assistant Professor of Physics, NJIT

Dr. Dale E. Gary, Committee Member — Date
Distinguished Professor of Physics, Director of Owens Valley Solar Array, NJIT

Dr. Jeongwoo Lee, Committee Member — Date
Research Professor of Physics, NJIT

Dr. Martin Schaden, Committee Member — Date
Associate Professor of Physics, Rutgers University, Newark

BIOGRAPHICAL SKETCH

Author: Sung-Hong Park

Degree: Doctor of Philosophy

Date: August 2010

Date of Birth: January 14, 1983

Place of Birth: Jeonju, South Korea

Undergraduate and Graduate Education:

- Doctor of Philosophy in Applied Physics,
  New Jersey Institute of Technology, Newark, New Jersey, 2010
- Dual Bachelor of Science in Physics and Astronomy,
  Chungnam National University, Daejeon, South Korea, 2005

Major: Applied Physics

Journal Publications:

Park, S.-H., Chae, J., Jing, J., Tan, C., & Wang, H. "Time Evolution of Coronal Magnetic Helicity in the Flaring Active Region NOAA 10930" 2010, *The Astrophysical Journal*, in press.

Park, S.-H., & Fleishmann, G. "Radio Emission from Masuda Sources" 2010, *Solar Physics*, in press.

Park, S.-H., Chae, J., & Wang, H. "Productivity of Flares and Magnetic Helicity Injection in Active Regions" 2010, *The Astrophysical Journal*, 718, 43.

Park, S.-H., Lee, J., Choe, G. S., Chae, J., Jeong, H., Yang, G., Jing, J., & Wang, H. "The Variation of Relative Magnetic Helicity Around Major Flares" 2008, *The Astrophysical Journal*, 686, 1397.

Liu, R., Liu, C., Park, S.-H., & Wang, H. "Gradual Inflation of Active-Region Coronal Arcades Building up to Coronal Mass Ejections" 2010, *The Astrophysical Journal*, in revision.

Jing, J., Chen, P. F., Wiegelmann, T., Xu, Y., Park, S.-H., & Wang, H. "Temporal Evolution of Free Magnetic Energy Associated with Four X-Class Flares" 2009, *The Astrophysical Journal*, 696, 84.

Tan, C., Jing, J., Abramenko, V. I., Pevtsov, A. A., Song, H., Park, S.-H., & Wang, H. "Statistical Correlation between Parameters of Photospheric Magnetic Field and Coronal Soft X-ray Brightness" 2007, *The Astrophysical Journal*, 665, 1460.

Presentations:

Park, S.-H., Chae, J., Jing, J., Tan, C., & Wang, H. "Time Evolution of Coronal Magnetic Helicity in the Flaring Active Region NOAA 10930", AAS/Solar Physics Division Meeting, Miami, Florida, May 23–27, 2010.

Park, S.-H., Jing, J., & Wang, H. "Three-Dimensional Structure Analysis of Electric Current Helicity in AR NOAA 10930 Associated with the X3.4 Flare of 2006 December 13", AAS/Solar Physics Division Meeting, Boulder, Colorado, June 14–18, 2009.

Park, S.-H., & Wang, H. "Analysis of Magnetic Helicity Injection for Use in Forecasting of Solar Flares", AAS/Solar Physics Division Meeting, Fort Lauderdale, Florida, May 27–30, 2008.

Park, S.-H., Lee, J., Choe, G. S., Chae, J., Jeong, H., Yang, G., Jing, J., & Wang, H. "Two Phases of Helicity Variation Around Major Flares", AAS/Solar Physics Division Meeting, Durham, New Hampshire, June 25–30, 2006.

To my family,

for their endless love and support

ACKNOWLEDGMENT

This dissertation would not have been possible without the grace of God given me in Christ Jesus and also without the people behind my life for inspiring, guiding, and accompanying me through up and down. I am very thankful for all the help I have received throughout my Ph.D. studies.

First of all, I would like to thank my supervisor, Dr. Haimin Wang, for his continuous support during all my graduate work. Haimin is most responsible for helping me complete the writing of this dissertation. He taught me how to write academic papers, made me a better solar physicist, and showed me how to live the good life in Jesus Christ. Without his encouragement and constant guidance, I could not have finished this dissertation. He has been a wonderful mentor and role model. I will never forget his tender loving care.

My special thanks go my Ph.D. co-advisor, Dr. Wenda Cao, for his friendship, encouragement and advice. It was a great experience for me to take a trip with Wenda for carrying out the solar observation at the National Solar Observatory on Sacramento Peak in Sunspot, New Mexico.

Besides my advisors, I am heartily grateful to Dr. Dale E. Gary, Dr. Jeongwoo Lee, and Dr. Martin Schaden for serving as members of my Ph.D. committee and commenting to improve my dissertation. I thank Dr. Dale E. Gary for providing insightful suggestions on this dissertation. My special thanks go to Dr. Jeongwoo Lee. When I first arrived in NJIT, he kindly helped me adjust myself to the student life on foreign soil in many aspects. He then helped me very much in writing my first research paper. Together with Dr. Lee, I found the long-term variation of magnetic helicity as an important property of

solar magnetic fields, contrary to previous studies focused only on short-term variations. This finding had formed the main basis of this thesis.

I am also grateful to many collaborators I've worked with and contributed to various parts of this research, particulary to Dr. Jongchul Chae, who provided the IDL codes to determine magnetic helicity injection rate and helped me to publish papers in refereed journals. Dr. Ju Jing gave a lot of help on my study and provided nonlinear force-free extrapolated magnetic field data. I am grateful to Dr. Rui Liu for his assistance and advice related to the CME study in this dissertation. I thank Dr. Changyi Tan for providing me the vector magnetic fields derived from the *Hinode* Stokes profiles. I appreciate that Dr. Gregory D. Fleishman encouraged me to study radio emission from Masuda source, which is relatively new to me. This work is leading to a publication. I also thank all the group members for every help.

I would like to thank the academic and support staff of the Center for Solar-Terrestrial Research and New Jersey Institute of Technology for providing resources and financial support. Special thanks should be given to Ms. Christine Oertel, the administrative assistant in our research center, for assisting me in many ways.

Last, but certainly not the least, I thank my parents for their constant loving support and prayer so that I could achieve this grade.

This dissertation took the advantage of comprehensive data from several solar space mission including *SOHO*, *GOES*, and *Hinode*. This work was supported by the Korean Research Foundation Grant KRF-2008-220-C00022 and by NSF under grants AGS-0548952 and AGS-0745744 and by NASA under grants NNG0-6GC81G, NNX08-AQ90G, and NNX08-BA22G.

TABLE OF CONTENTS

Chapter **Page**

TABLE OF CONTENTS
(Continued)

Chapter **Page**

LIST OF TABLES

Table **Page**

LIST OF FIGURES

Figure **Page**

LIST OF FIGURES
(Continued)

Figure **Page**

LIST OF FIGURES
(Continued)

Figure **Page**

LIST OF FIGURES
(Continued)

Figure **Page**

LIST OF FIGURES
(Continued)

Figure **Page**

LIST OF FIGURES
(Continued)

Figure **Page**

LIST OF FIGURES
(Continued)

Figure **Page**

CHAPTER 1

INTRODUCTION

Our star, the Sun, has been studied for a long time in human history, not only due to intellectual curiosity but also due to its importance for life on Earth. As a result, many outstanding findings have been obtained, and they have affected our society in many ways. For example, the apparent annual motion of the Sun on the sky was measured and used to establish a solar calendar which was necessary for planning nomadic activity, farming, sacred feasts, etc.

By the late 20th century, solar space missions (e.g., *Yohkoh*, *RHESSI*, and *SOHO*) opened up a new era in the study of the Sun by carrying out observations under conditions of atmosphere-free space and in the expanded wavelength coverage of the extreme ultraviolet, X-rays, and gamma rays. Consequently, it is now clearer that there are very dynamic and eruptive phenomena in the solar atmosphere such as solar flares and coronal mass ejections (CMEs) which can affect the Earth's environment. In addition, it was reported that enormous economic and commercial losses (Baker 2004; Schwenn 2006) can be caused by flares and CMEs. Therefore, a considerable amount of effort is recently being devoted to developing a flare/CME forecasting system as part of the study of space weather.

The main objective of this dissertation is to understand how a long-term (a few days) variation of magnetic helicity, one of the key parameters to describe evolution of surface magnetic field in an active region on the Sun, is associated with the energy buildup and instability leading to solar eruptions: flares and CMEs. Before presenting the studies and results of this dissertation in Chapters 3–6, an overview of the relevant background and

previous studies related to this dissertation will be introduced in this chapter, followed by the description of methods used for calculating the magnetic helicity in Chapter 2.

1.1 General Description of the Sun

The Sun is one of a few hundred billion stars in our Galaxy. It is located within one of the spiral arms at a distance of ∼8,500 parsecs (1 parsec = 3.0857×10^{16} m) from the center of our Galaxy, and revolves around the galactic center at a speed of ∼220 km s^{-1}. Comparing fundamental characteristics of the Sun to those of other stars in our Galaxy, astronomers found that the Sun is a very ordinary star which has typical values of mass, absolute visual magnitude, and effective temperature in the class of G-type stars.

The Sun emits energy, or radiation, in the form of electromagnetic waves that travel at the speed of light (e.g., 3×10^8 m s^{-1} in vacuum). The solar irradiance, also called the solar constant, $F_\odot$, is used to estimate the total amount of solar radiation. Its definition is the total amount of solar radiation energy, integrated over all wavelengths per unit time and unit area at the mean distance of the Earth from the Sun outside the Earth's atmosphere. The Active Cavity Radiometer Irradiance Monitor (ACRIM) aboard the Solar Maximum Mission (SMM) satellite measured $F_\odot$ from 1980 to 1989, and determined its mean value of 1367 J s^{-1} m^{-2} (or 1367 W m^{-2}) with variations of up to 0.2% over several days. In addition, Fröhlich & Lean (1998) found that the long-term variation of $F_\odot$ is *in phase* with the 11 year solar activity cycle, after investigating measurements made by five independent space-based radiometers.

The average distance of the Sun from the Earth over the Earth's orbital period around the Sun, the astronomical unit (AU), is an essential measurement because it can

be used to derive the size, mass, luminosity, and effective temperature of the Sun with other observations. In 1976, the International Astronomical Union (IAU) formally defined the astronomical unit as equal to the distance from the centre of the Sun at which a particle of negligible mass, in an unperturbed circular orbit, would have an orbital period of 365.2568983 days. The astronomical unit, therefore, is exactly 149,597,870.691 km, slightly less than the mean Sun-Earth distance.

Once the astronomical unit (AU) and the Earth's orbital period (P_E) are determined, the Sun's mass, $M_\odot$, can be estimated from Newton's formulation of Kepler's third law:

$$M_\odot \simeq 5.9165 \times 10^{11} \frac{(1\,\mathrm{AU})^3}{{P_E}^2} = 1.989 \times 10^{30}\,\mathrm{kg}. \tag{1.1}$$

Using the astronomical unit and $F_\odot$, the Sun's absolute luminosity, $L_\odot$, can be derived from:

$$L_\odot = 4\pi F_\odot (1\,\mathrm{AU})^2 = 3.85 \times 10^{26}\,\mathrm{W}. \tag{1.2}$$

The angular diameter of the visible solar disk as seen from the Earth varies in the range of 31.6–32.7 arcminutes ($'$) while the Earth revolves around the Sun in an elliptical path. In the late 20th century, several measurements of the Sun's diameter at 1 AU (Sofia et al. 1994; Wittmann 1997; Brown & Christensen-Dalsgaard 1998) were carried out, and they yielded a very similar value of around $31.99'$ which is used until today in the yearly *Astronomical Almanac*. From that, the average solar radius, $R_\odot$, is determined as 6.955×10^8 m. The effective temperature, $T_\odot$, of the visible solar disk can be obtained using the Stefan-Boltzmann law:

$$T_\odot = \left(\frac{L_\odot}{4\pi\sigma R_\odot^2} \right)^{1/4} = 5780\,\mathrm{K}, \tag{1.3}$$

where the Stefan-Boltzmann constant $\sigma = 5.670 \times 10^{-8}$ J m^{-2} K^{-4} s^{-1}. Please refer to Table 1.1 for other characteristic parameters of the Sun.

What is the chemical composition of, and physical conditions in, the Sun's atmosphere? In the 19th century, the development of spectroscopy allowed scientist to answer this question. In 1814, Joseph von Fraunhofer (1787–1826) measured the position of over 570 dark lines in the visible spectrum of the Sun, and then Gustav Robert Kirchhoff (1824–1887), in 1859, explained that the dark lines were caused by absorption of light by cooler gases in the solar photosphere. The dark absorption lines therefore were used not only to identify the chemical elements in the photosphere of the Sun but also to investigate the relative abundance of the elements in the photosphere. The solar photosphere is composed primarily of the chemical elements hydrogen and helium: hydrogen and helium account for 92.1% and 7.9% of the number of atoms in the photosphere. See Table 1.2 for the 20 most abundant elements in the photosphere.

1.2 Solar Active Regions

Solar active regions are localized volumes with intense magnetic fields in the solar atmosphere, from the photosphere to the corona. They develop when strong magnetic fields emerge from inside the Sun, and last from several hours to a few months. Sunspots, faculae, and bright points (or filigree) are observed on the photospheric surfaces of active regions, and their counterparts, plages, appear in the chromosphere. Radiation from active regions is enhanced, when compared to neighboring areas in the chromosphere and corona, over the whole electromagnetic spectrum, from X-rays to radio waves (see Figure 1.1 for maps of an active region observed at different wavelengths). Furthermore, most flares and

Table 1.1 Physical Properties of the Sun Referred from Lang (2001) and Stix (2004)

Physical Property		Value
Mean distance, AU		$1.49597870691\times10^{11}$ m
Radius, $R_\odot$		6.955×10^{8} m (109 Earth radii)
Volume		1.412×10^{27} m^3 (1.3 million Earths)
Mass, $M_\odot$		1.989×10^{30} kg (332,946 Earth masses)
Mean density		1409 kg m^{-3}
Solar irradiance, $F_\odot$		1366.2 W m^{-2}
Luminosity, $L_\odot$		3.85×10^{26} W
Pressure	(center)	2.334×10^{16} Pa
	(photosphere)	10 Pa
Temperature	(center)	1.56×10^{7} K
	(photosphere)	5780 K
	(chromosphere)	6×10^{3} – 2×10^{4} K
	(transition region)	2×10^{4} – 2×10^{6} K
	(corona)	2×10^{6} – 3×10^{6} K
Rotation period	(equator)	26.8 days
	(30° latitude)	28.2 days
	(60° latitude)	30.8 days
Magnetic Field	(sunspots)	1×10^{3} – 4×10^{3} G
	(polar)	10 G

Table 1.2 The 20 Most Abundant Elements in the Photosphere of the Sun Adopted from Lang (2001)

Element	Symbol	Atomic Number	Abundance[a]
Hydrogen	H	1	2.79×10^{10}
Helium	He	2	2.72×10^{9}
Carbon	C	6	1.01×10^{7}
Nitrogen	N	7	3.13×10^{6}
Oxygen	O	8	2.38×10^{7}
Neon	Ne	10	3.44×10^{6}
Sodium	Na	11	5.74×10^{4}
Magnesium	Mg	12	1.07×10^{6}
Aluminum	Al	13	8.49×10^{4}
Silicon	Si	14	1.00×10^{6}
Phosphorus	P	15	1.04×10^{4}
Sulfur	S	16	5.15×10^{5}
Chlorine	Cl	17	5.24×10^{3}
Argon	Ar	18	1.01×10^{5}
Potassium	K	19	3.77×10^{3}
Calcium	Ca	20	6.11×10^{4}
Chromium	Cr	24	1.35×10^{4}
Manganese	Mn	25	9.55×10^{3}
Iron	Fe	26	9.00×10^{5}
Nickel	Ni	28	4.93×10^{4}

[a]Normalized to an abundance of Silicon = 1.00×10^{6}.

CMEs occur in active regions.

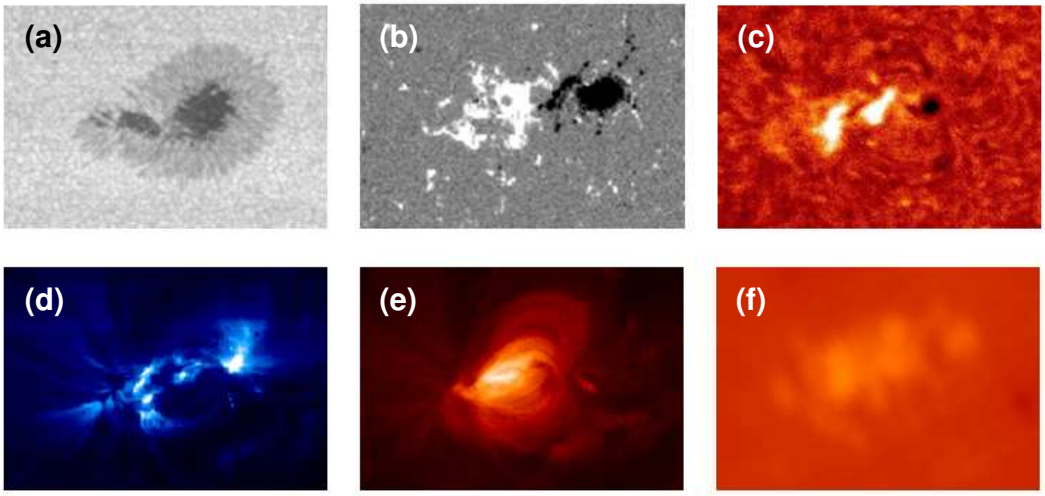

Figure 1.1 Maps of solar active region NOAA 10988 observed by (a) the Solar Optical Telescope (SOT) onboard the *Hinode* satellite (continuum intensity map), (b) the Michelson Doppler Imager (MDI) onboard the Solar and Heliospheric Observatory (*SOHO*) spacecraft (line-of-sight magnetic field map), (c) Solar Magnetic Fields Telescope at Huairou Solar Observing Station (H_α map), (d) the Extreme ultraviolet Imaging Telescope (EIT) onboard *SOHO* (171 Å EUV map), (e) the X-ray Telescope (XRT) onboard *Hinode* (soft X-ray map), and (f) Nobeyama Radio Heliograph (17 GHz map). Note that the field-of-view (FOV) and spatial resolution of the maps are different from each other.

Active regions are allocated numbers by the Space Weather Prediction Center in the US government's National Oceanic and Atmospheric Administration (NOAA) in the order of their appearance. The present numbering system started on 1972 January 5. The numbers are prefixed by AR for Active Region. Active regions that exist for more than one solar rotation are given a new number each time they reappear. Note that the active region numbers, in this dissertation, follow this NOAA active region numbering system.

1.2.1 Sunspots

Sunspots are the sites of strong magnetic fields in the Sun's photosphere that appear as dark spots compared to their surroundings. Early records of naked-eye observations of sunspots appeared in ancient history. However, sunspots had been interpreted as a transit of Mercury or Venus across the Sun until the first telescopic observations of sunspots were carried out in the early 17th century. In 1613, based on the observations of the motion of sunspots across the apparent solar disk, Galileo Galilei (1564–1642) reported that sunspots are features on the solar surface, and not little planets. He also found that sunspots, irregular in shape, form and disappear, which caused a great sensation in the traditional notion that all heavenly bodies should be unchanged, incorruptible, and perfect. In 1843, Samuel Heinrich Schwabe (1789–1875) first presented a probable 10-year periodicity in the average number of sunspots by carefully recording the occurrence of sunspots for 17 years. Thereafter, Christopher Carrington (1826-1875) found that the average latitude of sunspots observed during 1853–1861 decreases continuously from the beginning to the end of a solar cycle. By investigating all available records of sunspot observations back to the early 17th century, Rudolf Wolf (1816–1893) made the more accurate estimate of 11 years for the average duration of the sunspot cycle discovered by Schwabe and confirmed by Carrington. In the early 20th century, Hale (1908) measured magnetic fields on the Sun for the first time, and his study (Hale et al. 1919) for the magnetic polarity of sunspot pairs revealed that the Sun's magnetic field varies over a period of $\sim$22 years and it plays a fundamental role in the 11-year cycle of solar activity.

Figure 1.2 shows a typical sunspot which consists of a dark inner core (umbra) and a lighter periphery (penumbra) of narrow filaments in white light. The magnetic field in the

umbra is generally perpendicular to the solar surface and typically has a strength of 2000–3000 G (Penn & Livingston 2006). On the other hand, the penumbra shows a more inclined magnetic field with a magnitude of about 1000 G: with growing distance from the umbra, the magnetic field becomes more inclined and is nearly horizontal in the outer penumbra. The average inclination angle (the angle between magnetic field lines and the surface) of the magnetic field in the penumbra is in the range of 35–60° (Title et al. 1993; Langhans et al. 2005). A nearly horizontal plasma outflow of several km s^{-1}, the Evershed flow, occurs in the penumbra. The effective temperatures of the sunspot umbra and penumbra are ∼4000 K and ∼5500 K, respectively.

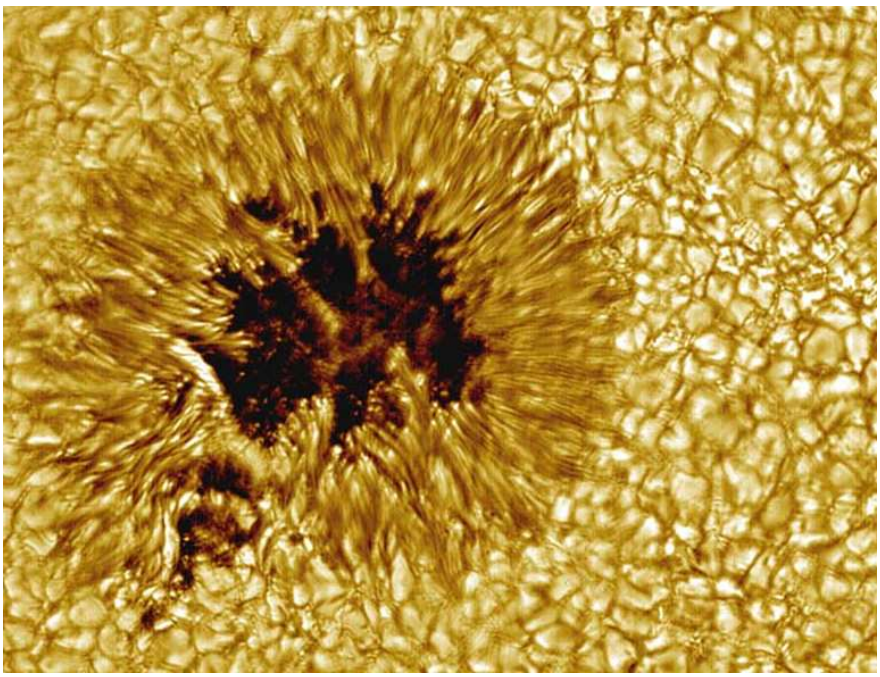

Figure 1.2 An ordinary sunspot taken with the 76-centimeter Vacuum Tower Telescope at Sacramento Peak, New Mexico. This sunspot shows a fairly regular penumbral structure, and a granulation pattern appears over a large part of the umbra. Some streamers as bright as the surrounding photosphere, called *light-bridges*, can be seen across the umbra (courtesy of National Solar Observatory).

Pores are small and short-lived dark spots in the photosphere. Sunspot groups originate as one or more sunspot pores, and develop in time. Note however that most groups usually disappear in the initial stage. Waldmeier (1955) and Kiepenheuer (1953) described a general development pattern of sunspot groups as follows: (1) on the 1st day, a sunspot group is formed from a number of pores concentrated within an area of 5–10 square heliographic degrees , (2) on the 2nd day, the individual pores in the group become larger up to the size of sunspots, and the group becomes elongated; the spots are gathered together at the preceding (west) and following (east) ends of the group, (3) in the 3rd–4th days, the spots keep on growing and the main preceding and following spots develop a penumbra; many small spots (about 20–50) appear between the two main spots, (4) in the 5th–12th days, the group reaches its maximum area during this period, (5) in the 13th–30th days, the small spots between the two main spots disappear, and the main following spot disappears usually by breaking up into several small spots which gradually decrease in size, and (6) in the 30th–60th days, the main preceding spot also becomes smaller and smaller until it disappears.

There are several schemes to classify sunspot groups. Waldmeier (1955) suggested 9 characteristic stages (known as the Zürich classification) related to the configuration and size of pores, main spots, and penumbrae in a sunspot group. This classification is based on the visual appearance of sunspot groups, and it also takes account of *evolutionary* patterns of a sunspot group during the course of its development and decay. Later on, McIntosh (1990) proposed a more sophisticated system of sunspot group classification including the modified Zürich classification. The McIntosh classification is accomplished by the following three criteria: (1) the group type based on the modified Zürich classification, (2)

the penumbra of the largest spot of the group, and (3) the compactness of the spots of the group. There is another way of classifying sunspots established by George Ellery Hale and his colleagues at the Mount Wilson Observatory in Los Angeles County, California. The Mount Wilson sunspot classification is based on the magnetic polarities of the individual spots in a sunspot group such as unipolar, bipolar, and complex groups. Refer to Table 1.4 for the detailed description of the sunspot classification.

Table 1.3: McIntosh Sunspot Classification Scheme Referred from Jenkins (2009)

Zürich class (modified)	
A	Unipolar group without penumbra
B	Bipolar group without penumbra on any spots
C	Bipolar group with penumbra on one end of group, usually surrounding largest of leading umbra
D	Bipolar group with penumbrae on spots at both ends of group and with longitudinal extent less than 10°
E	Bipolar group with penumbrae on spots at both ends of group and with longitudinal length between 10° and 15°
F	Bipolar group with penumbrae on spots at both ends of group and with longitudinal length more than 15°
H	Unipolar group with penumbra
Penumbra of Largest Spot	
x	No penumbra (class A or B)
r	Rudimentary penumbra partly surrounds largest spot
s	Small, symmetric penumbra, elliptical or circular and N–S size smaller than 2.5°
a	Small, asymmetric penumbra, irregular in outline and N–S size smaller than 2.5°
h	Large, symmetric penumbra, N–S size larger than 2.5°
k	Large, asymmetric penumbra, N–S size larger than 2.5°
Spot Compactness	
x	Assigned to (but undefined for) unipolar groups (types A and H)
o	Open– few, if any, spots between leader and follower
i	Intermediate– numerous spots between leader and follower, all without mature penumbra
c	Compact– many large spots between leader and follower, with at least one mature penumbra

1.2.2 Faculae, Bright Points, and Plages

A large number of tiny (a size of 10–100 km^2) bright features, primarily concentrated in active regions, are seen both in the continuum and in most photospheric lines (Guo et al.

2010; Zwaan 1987). Near the solar limb, they look like side-illuminated granules called "faculae" or "facular grains" (Muller 1975), and near the solar disk center mainly as "bright points" or "filigree", i.e., roundish bright features located in the intergranular downflow lanes (Dunn & Zirker 1973; Mehltretter 1974; Title et al. 1987). Faculae and bright points are considered as magnetized regions constituted of a bundle of small-scale vertical flux tubes with a magnetic field strength of a few kG. See Figure 1.3 which presents faculae near a sunspot pore.

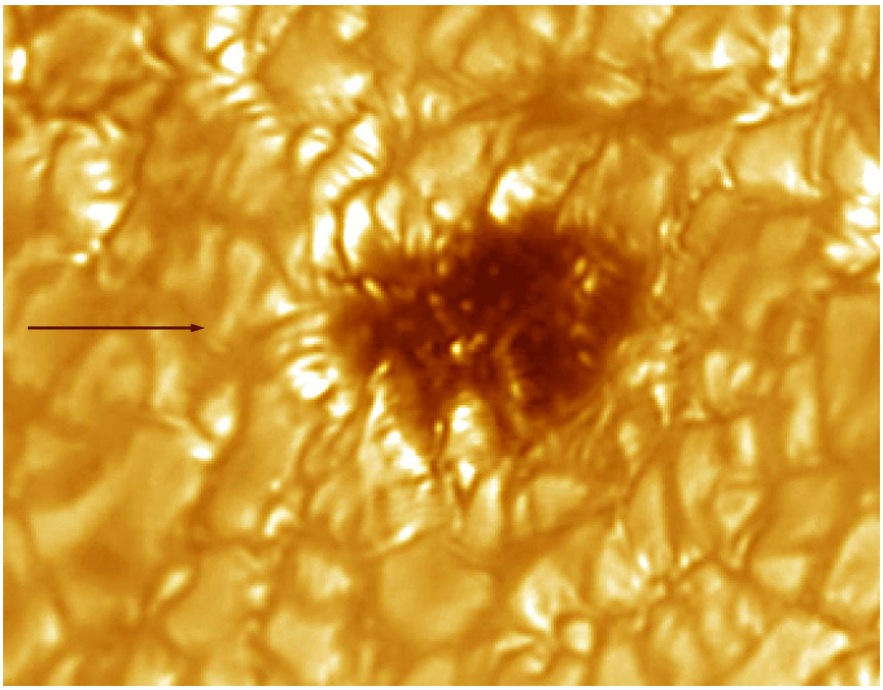

Figure 1.3 A pore with faculae was observed by the Swedish 1-m Solar Telescope (SST) on 2004 September 8 (observer Vasily Zakharov, Max Planck Institute).

Plages are bright, dense regions in the chromosphere found above sunspots or other active areas (e.g., faculae and bright points) of the solar photosphere, and they always accompany and outline sunspot groups. Figure 1.4 shows a H_α plage image near a sunspot. Plages appear much brighter in the monochromatic spectral lines (e.g., H_α, Ca II H and K,

Mg II h and k, and L_α) and in ultraviolet emission lines originating in the transition region (Zwaan 1987). Martinez Pillet et al. (1997) measured the magnetic field in plages, they found the average field strength of $\sim$1400 G inclined with respect to vertical of less than 10°.

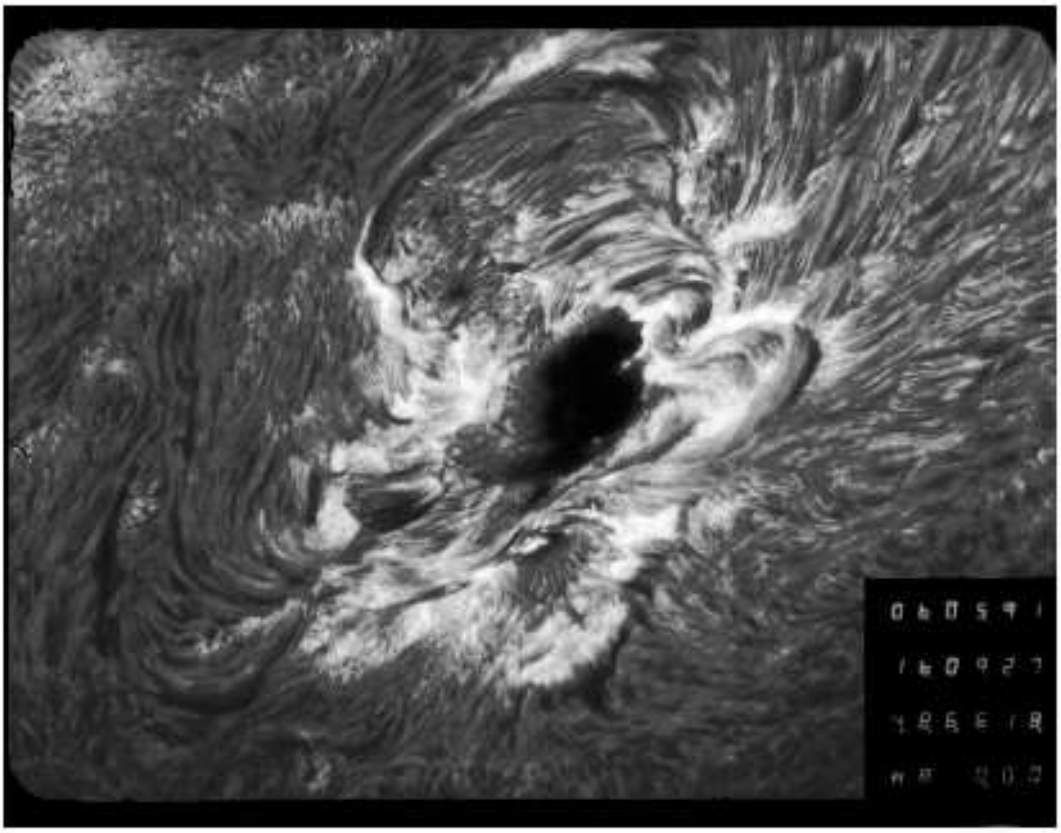

Figure 1.4 This high resolution H_α film image was taken with the 65-cm vacuum telescope of the Big Bear Solar Observatory located in Big Bear Lake, California on 1991 June 5. It has been recently digitized through the Solar Film Digitization (SFD) project of the Space Weather Research Laboratory at NJIT. Plages are shown as a white cloud-like feature around a sunspot.

1.2.3 Coronal Loops

Observations at extreme-ultraviolet (EUV) and soft X-ray wavelengths have revealed that hot and dense plasma in the corona is concentrated in magnetic loops called "coronal loops". Figure 1.5 shows coronal loops observed by the Transition Region and Coronal Explorer (TRACE) satellite in the 195 Å pass band (sensitive mostly to plasma emission around 1 MK). The electrons contained in coronal loops have temperatures of 1–10 MK and densities of 10^9–10^{11} cm^{-3}. The magnetized coronal loops are often anchored in bipolar sunspots within active regions.

Yohkoh Soft X-ray Telescope (SXT; Tsuneta et al. 1991) images showed that there are S- or inverse S-shaped coronal loops (Acton et al. 1992; Sakurai et al. 1992), called "sigmoids". Sigmoidal loops are considered as evidence for helically kinked magnetic flux ropes, which have a large amount of stored free energy (Rust & Kumar 1996). They frequently appear in active regions that have a high probability of producing flares and CMEs (Sterling & Hudson 1997; Hudson et al. 1998; Canfield et al. 1999; Glover et al. 2000). Sterling et al. (2000) found that sigmoid-associated flares usually follow the "sigmoid-to-arcade" evolution pattern, and later the same pattern was revealed in hard X-ray sigmoidal structure observed by *RHESSI* (Ji et al. 2008). Recently, several magnetohydrodynamic simulations (Magara & Longcope 2001; Kliem et al. 2004; Kusano 2005; Fan 2009) showed that a sigmoid-like current sheet can be formed due to the kink instability of an emerging flux tube. In addition, the formation and development of X-ray arcade-like loops are studied related to the occurrence of CMEs (Rust & Webb 1977; Švestka et al. 1998), and the coronal arcades are interpreted as a consequence of magnetic reconnection in the course of the eruptions (Kopp & Pneuman 1976).

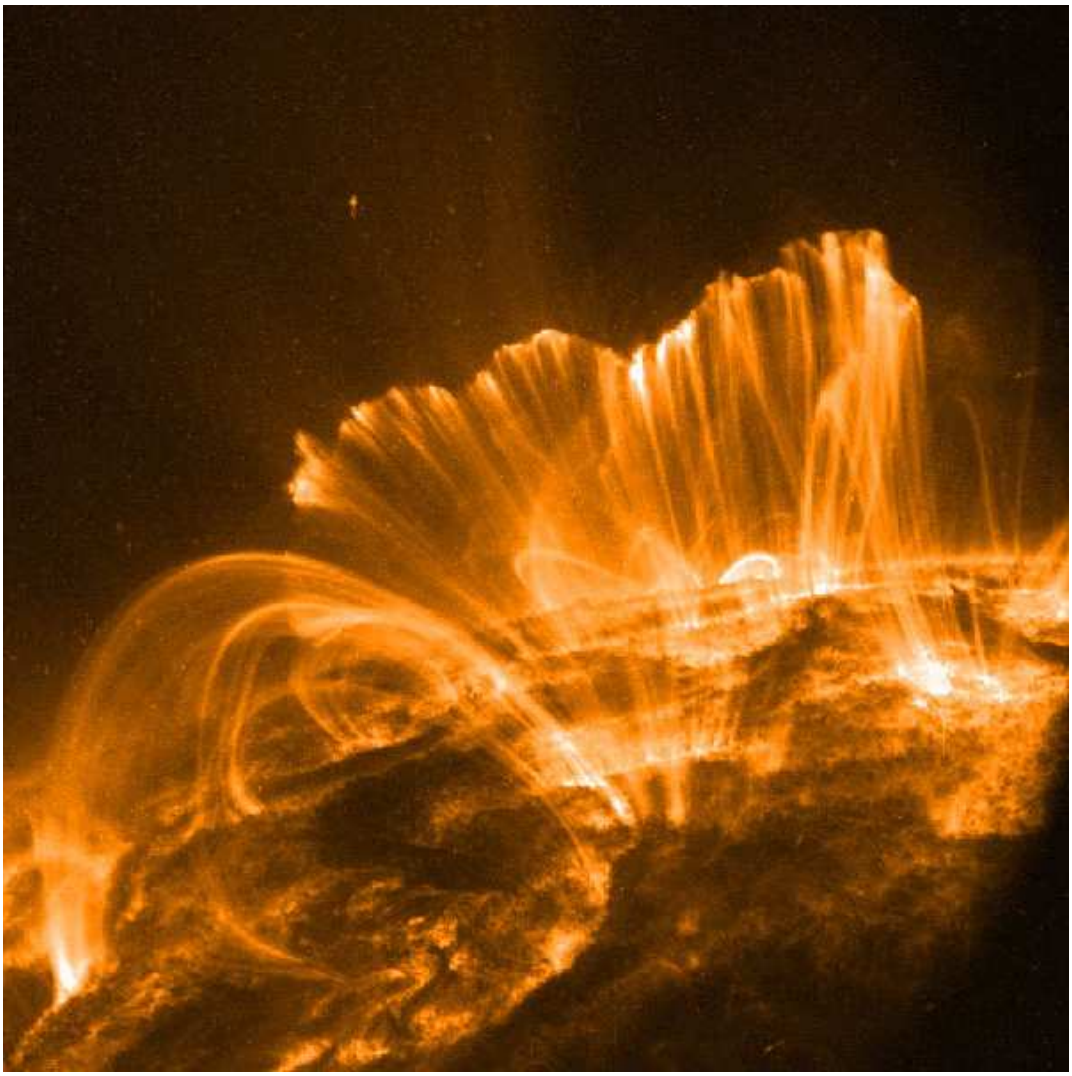

Figure 1.5 The image of coronal loops taken with NASA's Transition Region and Coronal Explorer (TRACE) satellite on November 9, 2000 (courtesy of NASA).

1.3 Solar Eruptions

1.3.1 Solar Flares

Solar flares are sudden, rapid (a few minutes to tens of minutes), and intense brightenings in the chromosphere and corona that can release up to 10^{32}–10^{33} ergs of energy. Figure 1.6 shows a large flare that occurred on 2006 December 13. Most flares occur in active regions where intense magnetic fields emerge from the Sun's surface into the corona, and it is generally thought that flare-productive active regions have complex and non-potential magnetic structures; release of the stored magnetic energy powers flares. Solar flares produce high energy particles, radiation, and erupting magnetic structures that are related to geomagnetic storms. Their strong electromagnetic radiations from gamma-rays to radio waves have direct effect on cell phones and the global positioning system and may heat up the terrestrial atmosphere within minutes so that satellites drop into lower orbits (Schwenn 2006). Enormous economic and commercial losses can be caused by these effects (Baker 2004).

In general, there are three classification methods of solar flares. First, their peak flux (in W m^{-2}) of 1–8 Å soft X-ray band measured by the *Geostationary Operational Environmental Satellite* (GOES) is used for flare classification. There are five *GOES* soft X-ray flare classes, A, B, C, M, and X in order of magnitude (see Table 1.5 for their peak flux range). A number following the letter of each class is the multiplicative factor. For example, an X5.2 event indicates a soft X-ray flare with a peak flux of 5.2×10^{-4} W m^{-2}. Second, based on the morphology of flaring site, flares are classified as compact point-like flares (Pallavicini et al. 1977; Tang 1985) and larger, longer-duration two-ribbon flares (Jing et al. 2005; Su et al. 2007). Lastly, the flares are divided into two groups by the time

Table 1.4 Mount Wilson Sunspot Classification Scheme Referred from Bray & Loughhead (1979)

Class	Description
α	Unipolar sunspot group
β	Sunspot group having both positive and negative magnetic polarities (bipolar), with a simple and distinct division between the polarities
γ	Complex sunspot group in which the positive and negative polarities are so irregularly distributed as to prevent classification as a bipolar group
$\beta\gamma$	Sunspot group that is bipolar but which is sufficiently complex that no single, continuous line can be drawn between spots of opposite polarities
δ	Sunspot group in which the umbrae of the positive and negative polarities are within 2 degrees of one another and within the same penumbra
$\beta\delta$	Sunspot group of general beta magnetic classification but containing one (or more) delta spots
$\beta\gamma\delta$	Sunspot group of beta-gamma magnetic classification but containing one (or more) delta spots
$\gamma\delta$	Sunspot group of gamma magnetic classification but containing one (or more) delta spots

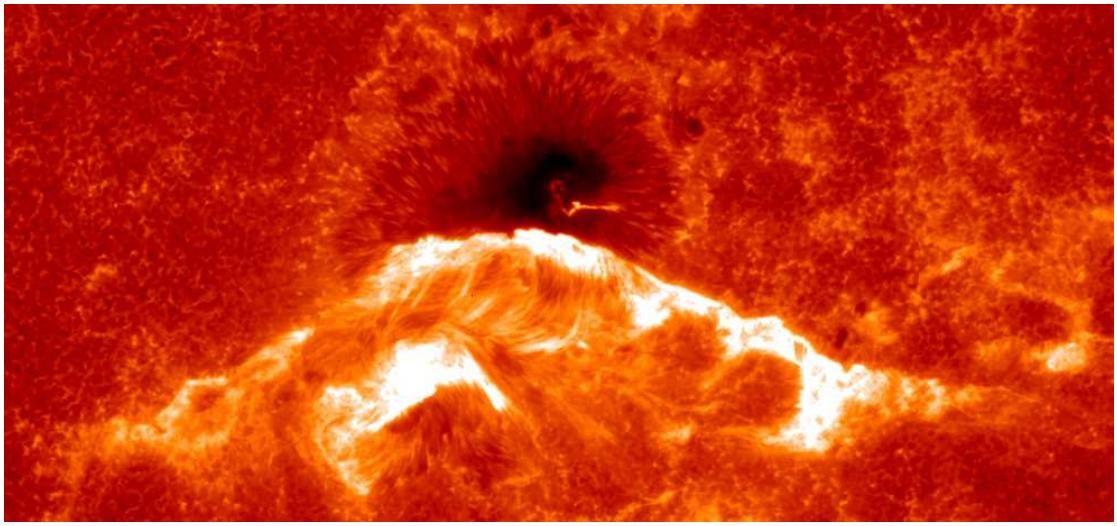

Figure 1.6 The *Hinode*/SOT Ca II H broadband image of a solar flare on 2006 December 13 (courtesy of *Hinode* Team).

profile of soft X-ray emission: single burst flare and multiple-burst flare. The multiple-burst flares include homologous flares (Waldmeier 1938; Martres 1989), sympathetic flares (Richardson 1951; Pearce & Harrison 1990), and successive flares (Liu et al. 2009).

Solar flares were first observed and carefully recorded by Carrington (1859) and independently by Hodgson (1859) who noticed localized visible brightenings of small areas near a complex sunspot group, lasting a few minutes. Since the first flare observation, there have been extensive studies to investigate an energy build-up process and a trigger mechanism of flares. From the observations of the magnetic field in active regions, considerable attention has been paid to investigating the structure of magnetic fields in the flaring site of active regions and its evolution related to flares (e.g., the temporal evolutions of magnetic shear angle the horizontal gradient of longitudinal magnetic fields). In addition, based on the reconnection of magnetic field lines in the flaring site, several flare models are developed such as CSHKP model (Carmichael 1964; Sturrock 1966; Hirayama 1974; Kopp & Pneuman 1976), emerging flux model (Heyvaerts et al. 1977), flux rope catastrophic model (Forbes & Priest 1995), magnetic breakout model (Antiochos 1998), loop-loop model (Uchida 1980) and tether-cutting model (Moore et al. 2001). However, in spite of many years of studies, there still remain many challenging and unsolved problems

Table 1.5 *GOES* Soft X-ray Classification of Flares

Class	Peak Flux[a] ($W\ m^{-2}$)
A	10^{-8}–10^{-7}
B	10^{-7}–10^{-6}
C	10^{-6}–10^{-5}
M	10^{-5}–10^{-4}
X	10^{-4} and above

[a]measured at 1–8 Å band

in understanding solar flares.

1.3.2 Coronal Mass Ejections

CMEs are the transient ejections into interplanetary space of as much as $\sim$100 billion kilograms of plasma and embedded magnetic fields from the solar corona, usually observed with white-light coronagraphs. Figure 1.7 shows a typical CME which has a three-part structure: a bright expanding loop (called front or helmet streamer), followed by a cavity embedded with a bright core of dense material (e.g., Illing & Hundhausen 1986). CMEs are propelled outward at speeds ranging from $<$20 to $\sim$3000 km s^{-1}, with an average speed of $\sim$480 km s^{-1} (Gopalswamy 2006). When fast CMEs, traveling faster than the ambient solar wind, are directed at Earth, they frequently cause intense geomagnetic storms. It has been also observed that they are often associated with eruptive prominences (Gopalswamy et al. 2003; Gilbert et al. 2000), strong flares (Moon et al. 2003; Vršnak et al. 2005), X-ray sigmoids (Sterling 2000), coronal dimmings (Zhukov & Auchère 2004), EIT and Moreton waves (Eto et al. 2002; Chen 2009), and post-eruptive arcades.

The first CME detection was made on 1971 December 14 by Tousey (1973) using white-light coronagraph data taken by the 7th Orbiting Solar Observatory (OSO-7) satellite. Since then, there have been many studies on the initiation and propagation, including the phases of slow rise, acceleration, constant velocity, and deceleration, of CMEs. From many observations and simulations for CMEs, it is generally believed that typical three-part CMEs are related to an erupting flux rope system. The overall eruption process of the flux rope can be explained well based on the classical CSHKP framework. However, a triggering mechanism, making the flux rope unstable in the initial stage of the eruption,

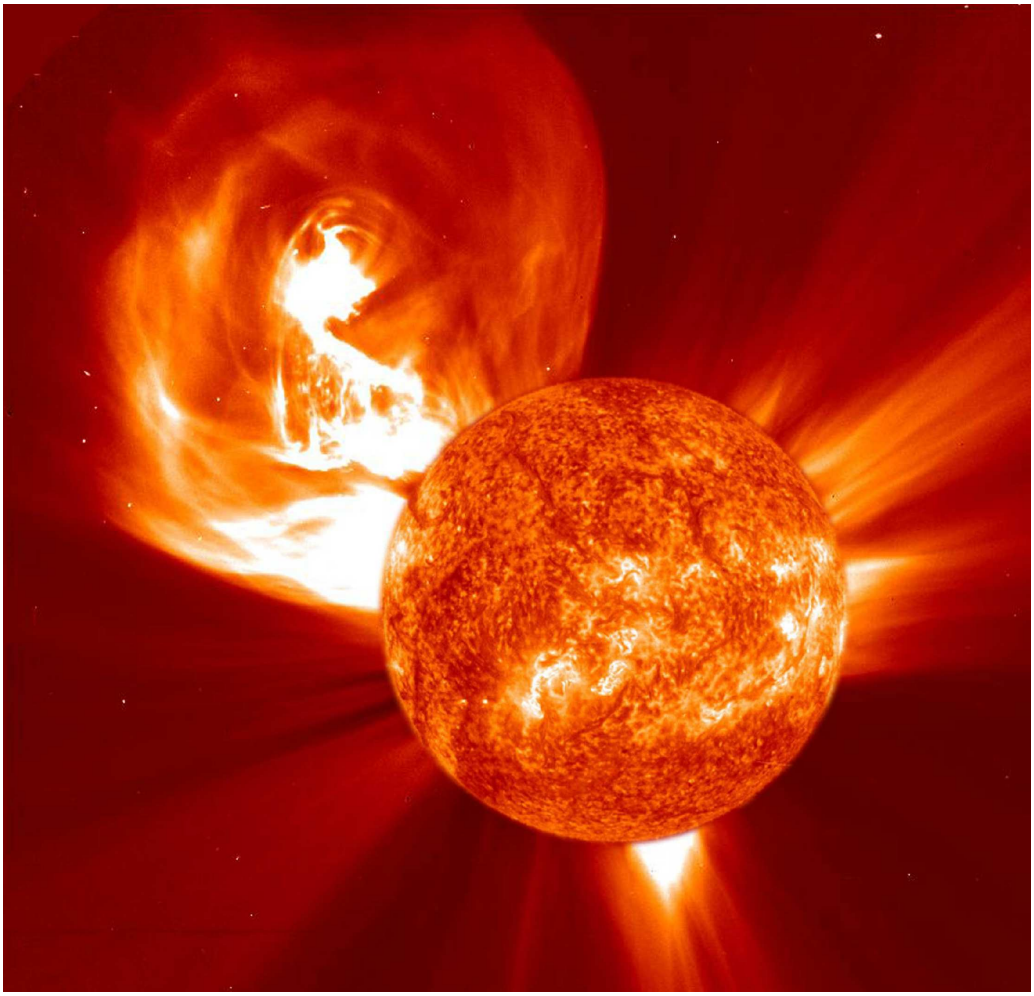

Figure 1.7 A typical CME image taken by the Large Angle and Spectrometric Coronagraph (LASCO)/C2 onboard the *SOHO* satellite on 2002 January 4. A *SOHO*/EIT image is enlarged and superimposed on the LASCO/C2 image (courtesy of *SOHO* Team).

has not been understood clearly yet. Related to the CME initiation, therefore, several triggering mechanisms are proposed based on numerical simulations of CMEs: reconnection-favorable emerging flux model (Chen & Shibata 2000; Chen 2008), flux cancelation model (van Ballegooijen & Martens 1989; Linker et al. 2001), breakout model (Antiochos et al. 1999; MacNeice et al. 2004), and kink instability by the emergence of twisted flux tube (Hood & Priest 1981; Fan & Gibson 2004; Török & Kliem 2005). More observational studies are however needed to determine and/or suggest a most convincing model which can explain the detailed processes involved in the occurrence and propagation of CMEs.

1.4 Magnetic Helicity

Magnetic helicity is a measure of the amount of twist of magnetic field lines around the tube axis in a flux tube, the amount of kink in the tube axis, and the extent of interlinking of flux tubes in a magnetic field system (Berger & Field 1984; Pevtsov 2008). Figure 1.8 shows twist, kinks, and inter-linkages of magnetic field lines which contribute to magnetic helicity. Magnetic helicity is a useful parameter to indicate topology and non-potentiality of a magnetic field system, and a quantity that is approximately conserved in real plasmas. Mathematically, magnetic helicity, H, inside a volume, V, of a magnetic field system is defined by:

$$H = \int_V \boldsymbol{A} \cdot \boldsymbol{B}\, dV, \tag{1.4}$$

where $\boldsymbol{A}$ is the vector potential of the magnetic field, $\boldsymbol{B}$, i.e., $\boldsymbol{B} = \nabla \times \boldsymbol{A}$. In addition, considering magnetic fields as a system of thin flux tubes with magnetic flux, Φ, magnetic

helicity can also be described as (Berger & Field 1984):

$$H = \sum_i (\mathrm{T}_i + \mathrm{K}_i)\Phi_i^2 + \sum_i \sum_{j \neq i} \mathrm{L}_{ij}\Phi_i\Phi_j, \tag{1.5}$$

where T_i is the twist number of field lines in the ith tube, K_i is the kink number of the ith tube axis, and L_{ij} is the inter-linkage number between the ith and the jth tubes.

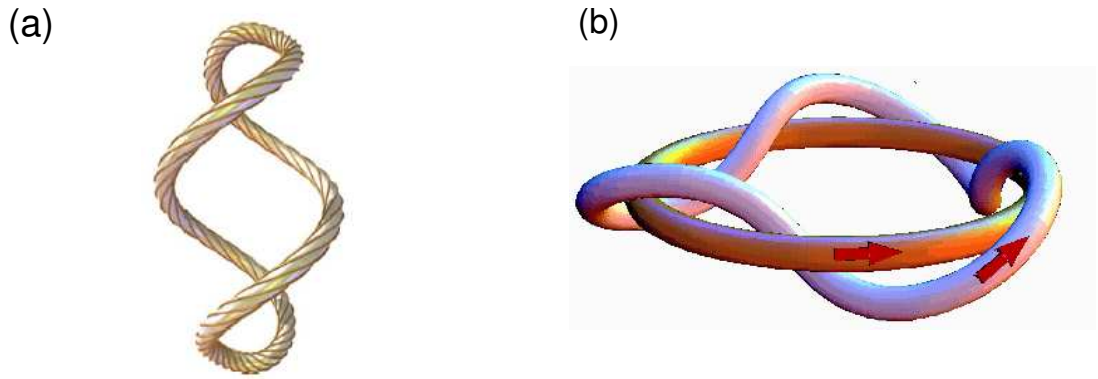

Figure 1.8 Magnetic helicity consists of: (a) twists of magnetic field lines inside a flux tube and kinks of flux tube axes, and (b) inter linkage between flux tubes. These images are adopted from Figure 2 of Berger & Prior (2006) and Figure 1 of Berger (1999).

In the last half-century, magnetic helicity has recieved the significant attention in studying the Sun. There have been studies of a "solar active-region hemispheric helicity rule", i.e., regions of negative (left-handed) helicity occur predominantly in the northern solar hemisphere and those of positive (right-handed) helicity in the southern hemisphere. Longcope et al. (1999) and Longcope & Pevtsov (2003) investigated the possible mechanisms for this hemispheric helicity rule taking into account solar differential rotation, direct action of the Coriolis force, solar dynamo, and turbulent convection in upper portion of the convection zone. Berger & Ruzmaikin (2000) showed that the magnetic helicity produc-

tion in the interior by solar differential rotation follows the hemispheric rule in the northern and southern hemispheres (refer to Figure 1.9). This hemispheric dependence extends from photospheric observations to in situ measurements of magnetic clouds in the solar wind: morphology of filaments (Martin et al. 1994), morphology of coronal loops (Rust & Kumar 1996), in situ measurements of interplanetary fields (Burlaga 1988; Bieber et al. 1987b,a). From observations of 69 active regions in solar cycle 22, Pevtsov et al. (1995) found that 76% of the regions in the northern hemisphere had negative helicity and 69% in the south had the opposite helicity. Subsequent to this study, Longcope et al. (1998) reconfirmed this hemispheric rule with a much larger data set of 203 active regions. From observations with the Huairou Solar Magnetic Field Telescope, Abramenko et al. (1996) and later Bao & Zhang (1998) found a similar tendency. Almost all existing dynamo models predict that the hemispheric helicity rule should be invariant with respect to phase of the solar cycle and is supported by observations (e.g., Hale 1927; Pevtsov et al. 1995; Abramenko et al. 1996; Bao & Zhang 1998; Longcope et al. 1998; Pevtsov et al. 2001). However, Choudhuri et al. (2004) proposed based on a dynamo model that when new cycle active regions interact with previous cycle large scale magnetic fields, the magnetic helicity may not obey the hemispheric rule. It was observationally supported by Hagino & Sakurai (2005). Therefore, it is still an important task to reveal whether the hemispheric helicity rule is independent of solar cycle or it reverses its sign during certain periods of solar activity.

In addition, magnetic helicity studies have been conducted to understand the energy buildup and instability leading to solar eruptions such as prominence eruptions (Romano et al. 2003, 2005), the occurrence of major flares (Moon et al. 2002a,b; Kusano et al. 2003b; Park et al. 2008), and CMEs (Nindos et al. 2003). This linkage was motivated by obser-

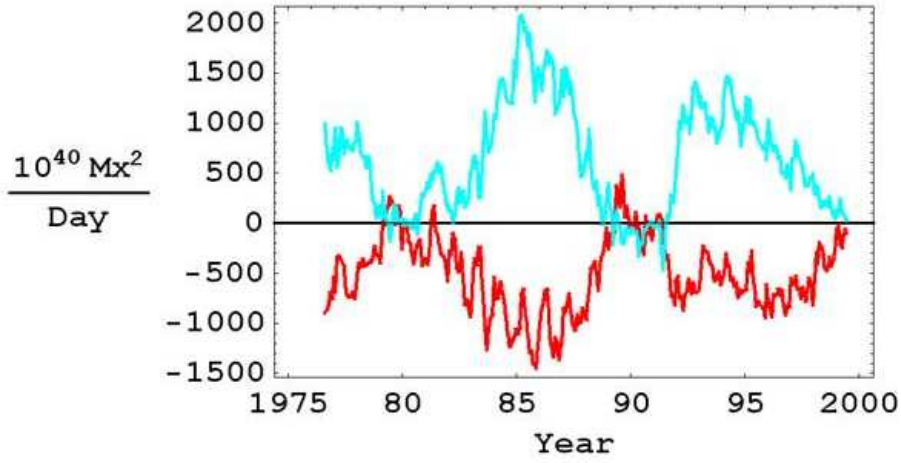

Figure 1.9 Magnetic helicity in the interior of the Sun produced by differential rotation during 1976–1998 (Berger & Ruzmaikin 2000). Negative helicity is predominantly in the northern hemisphere (red line), while positive helicity, in the southern hemisphere (blue line).

vations of solar eruptions being associated with twisted magnetic field configuration (see Figure 1.10 for a helically twisted prominence). However, we need to quantitatively investigate how magnetic helicity is related to energy storage, pre-flare conditions, and triggering mechanisms of flares with a large number sample of events. This dissertation aims at the study of magnetic helicity injection in active regions related to (1) the occurrence and intensity of flares and (2) the initiation, slow rise phase, and speed of CMEs, which not only helps to understand physical processes of energy build-up and onset of solar eruptions, but also provides a unique tool for a more reliable flare/CME predictions.

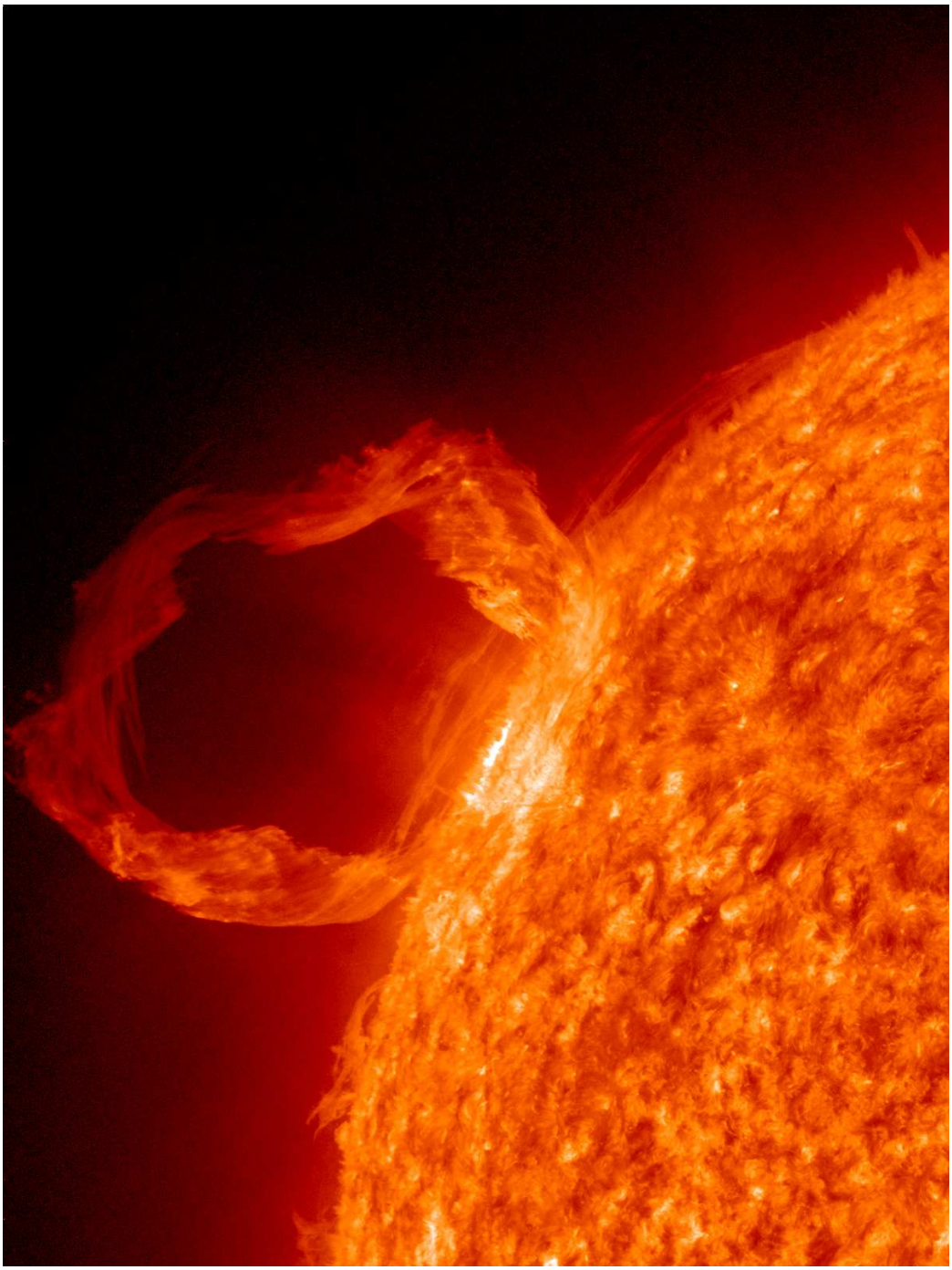

Figure 1.10 A solar eruptive prominence as seen in extreme UV light on 2010 March 30 (courtesy of *SDO* Team).

CHAPTER 2

CALCULATION OF MAGNETIC HELICITY IN ACTIVE REGIONS

Magnetic helicity inside a volume, V, of a system having magnetic field, $\boldsymbol{B}$, is defined in Equation 1.4. In principle, magnetic helicity can be derived from $\boldsymbol{B}$ and its vector potential, $\boldsymbol{A}$. However, only if magnetic field lines never pass through the boundary surface enclosing V is magnetic helicity invariant with respect to the gauge for $\boldsymbol{A}$. This condition would not be satisfied for magnetic fields in a coronal volume, $V_{\rm cor}$, where most of the field lines are anchored in the photosphere or some of them expand out into interplanetary space passing through the boundary surface, $S_{\rm cor}$, enclosing $V_{\rm cor}$. In this case, it is necessary to define a gauge-invariant formula of magnetic helicity for investigating the topology and non-potentiality of magnetic fields inside $V_{\rm cor}$.

2.1 Magnetic Helicity in a Coronal Volume

The relative magnetic helicity, H_r, derived by Finn & Antonsen (1985) is a gauge-invariant measure of helicity inside $V_{\rm cor}$:

$$H_r = \int_{V_{\rm cor}} (\boldsymbol{A} + \boldsymbol{A}_p) \cdot (\boldsymbol{B} - \boldsymbol{P})\, dV, \tag{2.1}$$

where $\boldsymbol{P}$ is the potential field having the same normal component as $\boldsymbol{B}$ on $S_{\rm cor}$, and $\boldsymbol{A}_p$ is the vector potential for $\boldsymbol{P}$. H_r represents the amount of helicity subtracted by that of the corresponding potential field $\boldsymbol{P}$.

DeVore (2000) calculated H_r in the unbounded half space, i.e., z>0 in a Cartesian domain, using the following specific vector potentials, $\boldsymbol{A}$ and $\boldsymbol{A}_p$:

$$\boldsymbol{A}(x,y,z) = \boldsymbol{A}_p(x,y,0) - \hat{\boldsymbol{z}} \times \int_0^z \boldsymbol{B}(x,y,z')\,dz', \tag{2.2}$$

$$\boldsymbol{A}_p(x,y,z) = \nabla \times \hat{\boldsymbol{z}} \int_z^\infty \phi(x,y,z')\,dz', \tag{2.3}$$

where

$$\phi(x,y,z) = \frac{1}{2\pi} \int\int \frac{B_z(x',y',0)}{[(x-x')^2 + (y-y')^2 + z^2]^{1/2}}\,dx'dy'. \tag{2.4}$$

In Chapter 5, H_r in a coronal volume of NOAA AR 10930 is calculated using Fan's code (Fan 2009) in which the vector potentials given in Equations 2.2 through 2.4 are determined by treating the photosphere as an infinite plane (z=0) in a Cartesian coordinate system. Note that outside of the coronal magnetic field domain of AR 10930 under investigation, the magnetic field is assumed to be negligible even though, on average, $\sim$30% of the photospheric unsigned magnetic flux passed through the boundary surface of the domain above the photosphere. The helicity calculation, therefore, gives an approximate value of H_r in a coronal volume above the photospheric surface of AR 10930.

2.2 Magnetic Helicity Injection through a Photospheric Surface

Magnetic helicity refers to the *relative* magnetic helicity in the rest of this Dissertation, i.e., the helicity relative to that of the potential field state. Berger & Field (1984) derived the

change rate of magnetic helicity, $\dot{H}_r$, in an open volume through a boundary surface, S:

$$\dot{H}_r = -2 \int_S [(\boldsymbol{v}_t \cdot \boldsymbol{A}_p) B_n - (\boldsymbol{B}_t \cdot \boldsymbol{A}_p) v_n] \, dS, \tag{2.5}$$

where $\boldsymbol{v}$ represents the plasma velocity, and subscripts n and t denote the vertical component and the horizontal component to S, respectively. $\boldsymbol{A}_p$ is a specific vector potential satisfying:

$$\hat{\boldsymbol{n}} \cdot \nabla \times \boldsymbol{A}_p = B_n, \tag{2.6}$$

$$\nabla \cdot \boldsymbol{A}_p = 0, \tag{2.7}$$

$$\boldsymbol{A}_p \cdot \hat{\boldsymbol{n}} = 0. \tag{2.8}$$

The first term of Equation 2.5 is related to the helicity change by horizontal motions of field lines on the surface, and the second term corresponds to the change by the transport of helical fields across the surface. Démoulin & Berger (2003) considered the velocity $\boldsymbol{u}$ of field line footpoint motion given by:

$$\boldsymbol{u} \equiv \boldsymbol{v}_t - \frac{v_n}{B_n} \boldsymbol{B}_t, \tag{2.9}$$

and consequently, the two terms in Equation 2.5 can be combined into one:

$$\dot{H}_r = -2 \int_S (\boldsymbol{u} \cdot \boldsymbol{A}_p) B_n \, dS. \tag{2.10}$$

Chae (2001) developed a practically useful way of measuring $\dot{H}_r$ from Equation 2.10 using $\boldsymbol{v}_{\rm LCT}$, the velocity of the apparent horizontal motion of field lines determined by the

technique of local correlation tracking (LCT), instead of using $\boldsymbol{u}$:

$$\dot{H}_r \simeq \int_S G_A(\boldsymbol{x})\, dS, \tag{2.11}$$

with the integrand $G_A = -2(\boldsymbol{v}_{\rm LCT} \cdot \boldsymbol{A}_p)B_n$, called magnetic helicity flux (magnetic helicity per unit area per unit time). Figures 2.1 and 2.2 present $\boldsymbol{v}_{\rm LCT}$ and $\boldsymbol{A}_p$ of AR 10930, respectively, plotted as arrows on the grayscale map of B_n derived from the *SOHO*/MDI line-of-sight magnetogram at 06:27 UT on 2006 December 10. The grayscale G_A map is also shown in Figure 2.3: positive value (i.e., helicity flux density of right-handed sign) of G_A is displayed as white tone, while negative value (i.e., helicity flux density of left-handed sign) of G_A is displayed as black tones).

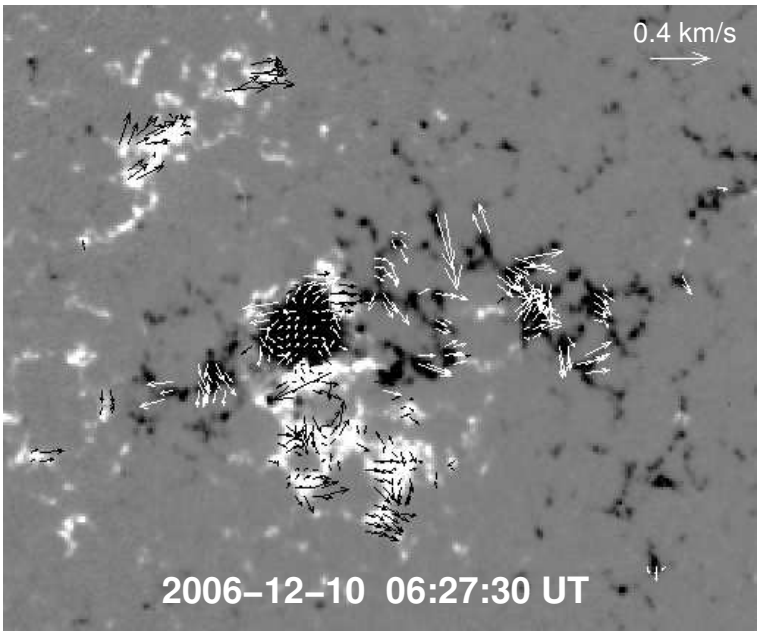

Figure 2.1 $\boldsymbol{v}_{\rm LCT}$ (arrows) of AR 10930 determined from the LCT method is superposed on the grayscale map of B_n derived from the MDI line-of-sight magnetogram at 06:27 UT on 2006 December 10.

In a following work, Chae et al. (2004) showed that $\boldsymbol{v}_{\rm LCT}$ is a good estimation for

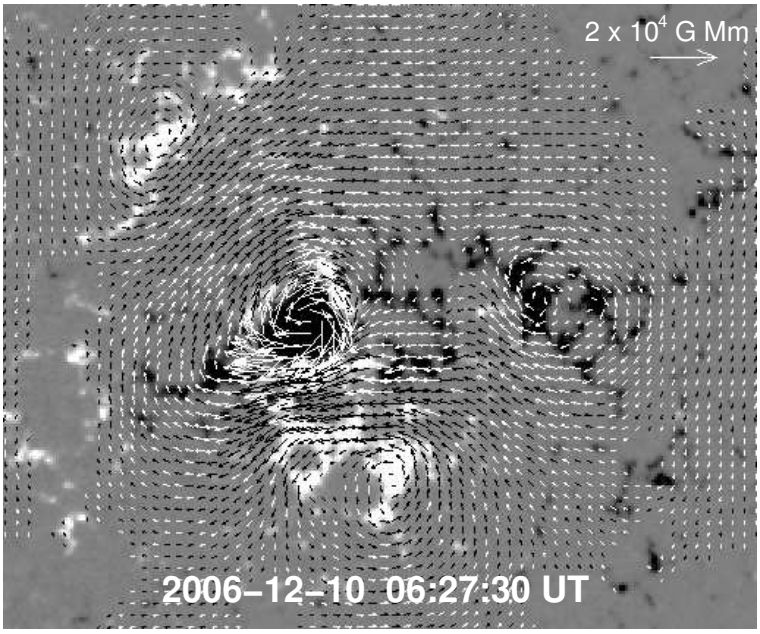

Figure 2.2 $\boldsymbol{A}_p$ (arrows) of AR 10930 is superposed on the grayscale map of B_n.

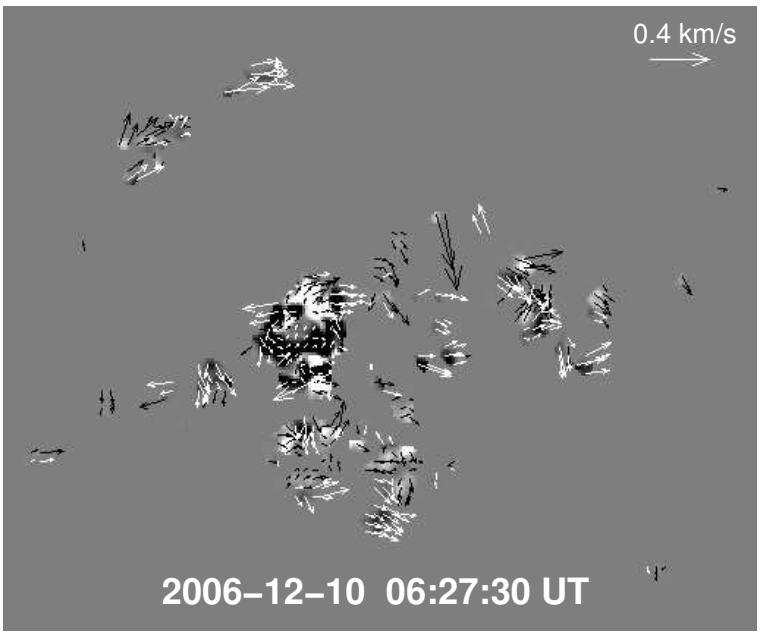

Figure 2.3 G_A map is displayed in grayscale with $\boldsymbol{v}_{\rm LCT}$ (arrows) of AR 10930. Note that the saturation level of $|G_A|$ is set as 1.67×10^6 G^2 km/s Mm for purpose of display visibility.

$\boldsymbol{u}$ when there is no significant new flux emergence. In addition, the study of Lim et al. (2007) indicated that the difference between magnetic helicity injection calculated from Equation 2.11 and coronal helicity estimated from the linear force-free field method is less than 15%. Chae's LCT method has been applied in many studies of measuring magnetic helicity injected into the corona through the photosphere by many researchers (e.g., Nindos & Zhang 2002; Moon et al. 2002a; Romano et al. 2005; Jeong & Chae 2007; LaBonte et al. 2007; Park et al. 2010), even though this method has the unavoidable limitations (Démoulin & Berger 2003; Chae et al. 2004; Kusano et al. 2004a; Schuck 2005): plasma motion along the magnetic field lines can not be detected with LCT nor can a horizontal plasma motion between areas with the same vertical magnetic field. In Chapters 3, 4, and 6, $\dot{H}_r$ is estimated using Chae's LCT method.

Recently, Chae (2007) developed a revised version of the original LCT method (Chae 2001) by adopting a better proxy, G_θ, of the helicity flux density proposed by Pariat et al. (2005):

$$G_\theta = -\frac{B_n}{2\pi}\int_{S'}\left(\frac{\boldsymbol{x}-\boldsymbol{x}'}{|\boldsymbol{x}-\boldsymbol{x}'|^2}\times[\boldsymbol{u}-\boldsymbol{u}']\right)_n B'_n\,dS', \tag{2.12}$$

where $\boldsymbol{x}$ is the position vector. In Chae's revised version (Chae 2007), the numerical integration of G_θ is carried out over all the pairs of discrete pixels so that the form of magnetic helicity flux at the ith pixel is written as:

$$G_i \equiv G_\theta(\boldsymbol{x}_i) = -\frac{B^i_n}{2\pi}\int_{S'}\left(\frac{\boldsymbol{x}_i-\boldsymbol{x}'}{|\boldsymbol{x}_i-\boldsymbol{x}'|^2}\times[\boldsymbol{u}_i-\boldsymbol{u}']\right)_n B'_n\,dS'. \tag{2.13}$$

Furthermore, G_i can be divided into two parts, G^S_i and G^M_i representing the contributions

of self helicity and mutual helicity, respectively:

$$G_i = G_i^S + G_i^M, \tag{2.14}$$

$$G_i^S = -\frac{B_n^i}{2\pi}\int_{S'}\left(\frac{\boldsymbol{x}_i - \boldsymbol{x}'}{|\boldsymbol{x}_i - \boldsymbol{x}'|^2} \times [\boldsymbol{u}_i - \boldsymbol{u}']\right)_n B_n' \, dS', \tag{2.15}$$

$$G_i^M = -\frac{B_n^i}{2\pi}\Delta S \sum_{j\neq i}\left(\frac{\boldsymbol{x}_i - \boldsymbol{x}_j}{|\boldsymbol{x}_i - \boldsymbol{x}_j|^2} \times [\boldsymbol{u}_i - \boldsymbol{u}_j]\right)_n B_n^j, \tag{2.16}$$

where ΔS is the area of each pixel. In addition, he estimated $\boldsymbol{u}$ by applying the normal component of the magnetic induction equation and the differential affine velocity estimator (DAVE) method developed by Schuck (2006). Figure 2.4 shows $\boldsymbol{u}_{\mathrm{DAVE}}$ (arrows) which is determined by the DAVE method with the same MDI magnetograms used for calculating $\boldsymbol{v}_{\mathrm{LCT}}$ in Figure 2.1. The magnitude and direction of $\boldsymbol{u}_{\mathrm{DAVE}}$ are generally similar to those of $\boldsymbol{v}_{\mathrm{LCT}}$ as shown in Figure 2.5. The linear (Pearson) correlation coefficient (CC) between $\boldsymbol{v}_{\mathrm{LCT}}$ and $\boldsymbol{u}_{\mathrm{DAVE}}$ is $\sim$0.6. However, there is a trend that $\boldsymbol{u}_{\mathrm{DAVE}}$ is a little larger than $\boldsymbol{v}_{\mathrm{LCT}}$: the average discrepancy between $\boldsymbol{v}_{\mathrm{LCT}}$ and $\boldsymbol{u}_{\mathrm{DAVE}}$ is $\sim$0.05 km/s. From $\boldsymbol{u}$ and B_n, G_i^S and G_i^M can be calculated from Equations 2.15 and 2.16, respectively, and they are shown in Figure 2.6. In Chapter 5, Chae's revised version of the $\dot{H}_r$ calculation (i.e., Equations 2.14 through 2.16) is used together with the DAVE method.

After $\dot{H}_r$ is determined as a function of time, the amount of helicity accumulation, ΔH_r, is determined by integrating $\dot{H}_r$ with respect to time:

$$\Delta H_r = \int_{t_0}^{t} \dot{H}_r \, dt, \tag{2.17}$$

where t_0 and t are the start and end time of the magnetogram data set under investigation,

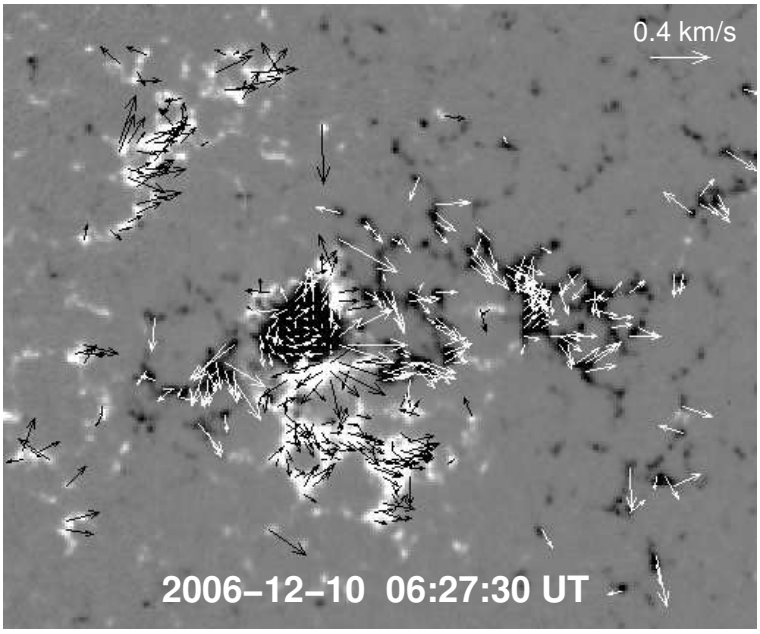

Figure 2.4 $\boldsymbol{u}$ (arrows) of AR 10930 determined from the DAVE method, is superposed on the same grayscale map of B_n in Figure 2.1.

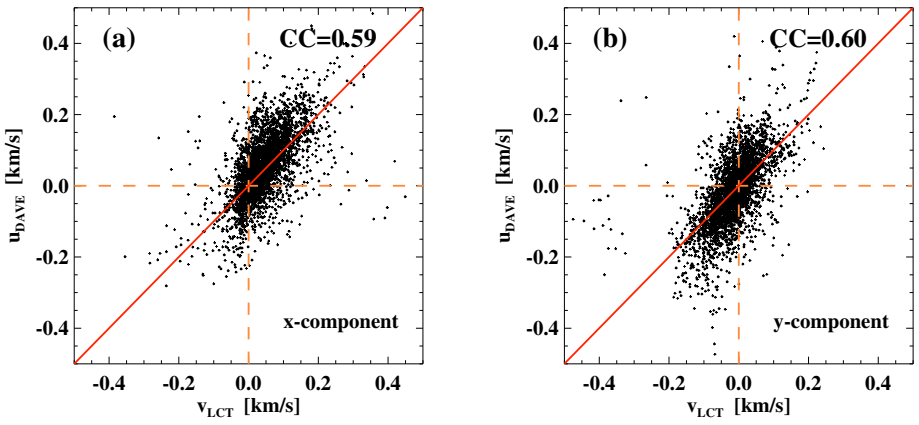

Figure 2.5 $\boldsymbol{u}_{\mathrm{DAVE}}$ vs. $\boldsymbol{v}_{\mathrm{LCT}}$ for their (a) x-components and (b) y-components. The linear CC is specified in each panel. The red line with a slope of 1 is plotted in each panel for purpose of displaying the discrepancy between $\boldsymbol{v}_{\mathrm{LCT}}$ and $\boldsymbol{u}_{\mathrm{DAVE}}$.

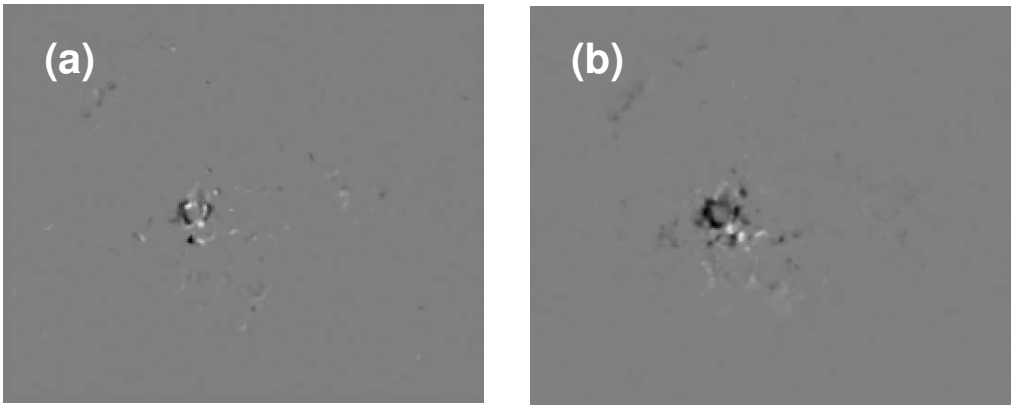

Figure 2.6 Grayscale maps of (a) G_i^S and (b) G_i^M in AR 10930 at 06:27 UT on 2006 December 10.

respectively. Figure 2.7 shows ΔH_r in AR 10930 calculated from the two different methods: (1) the original method (G_A with the LCT method) shown as cross symbols and (2) the revised method (G_θ with the DAVE method) as triangle symbols. As shown in Figure 2.7, the revised one yielded systematically higher values of helicity injection than the original one. By the comparison between these two methods of $\dot{H}_r$ calculation, Chae (2007) also found that their discrepancy is typically less than 10%.

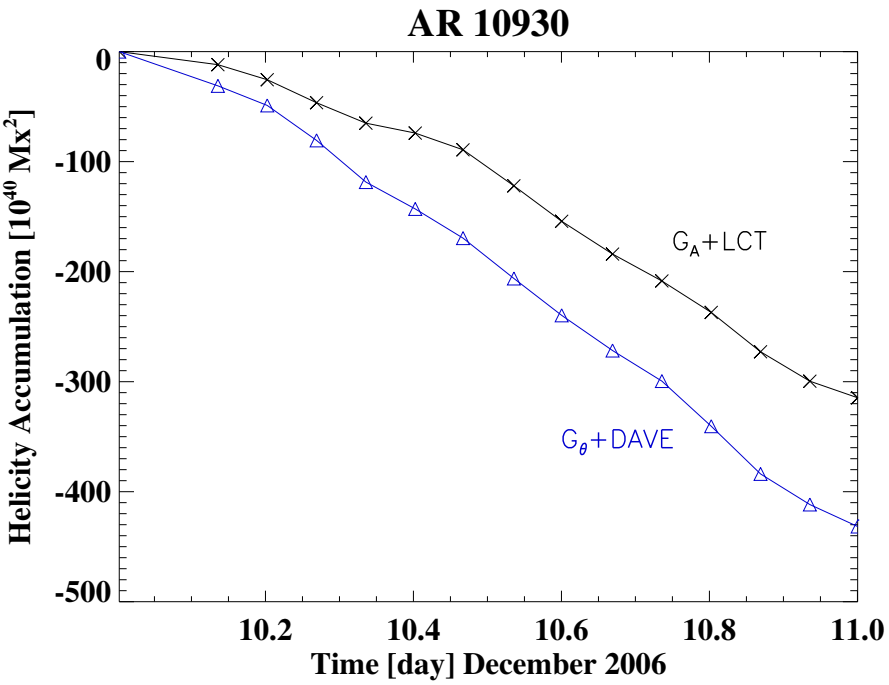

Figure 2.7 Time variations of helicity accumulation in AR 10930 calculated by the original method (G_A with the LCT method, shown as cross symbols) and the revised method (G_θ with the DAVE method, shown as triangle symbols).

CHAPTER 3

TEMPORAL VARIATION OF MAGNETIC HELICITY INJECTION IN ACTIVE REGIONS AROUND MAJOR FLARES

In this chapter[1], the variation of magnetic helicity is investigated over a span of several days around the times of 11 X-class flares which occurred in 7 active regions (AR 9672, 10030, 10314, 10486, 10564, 10696, and 10720) using the magnetograms taken by *SOHO*/MDI. As a major result, it is found that each of these major flares is preceded by a significant helicity accumulation, (1.8–16)$\times 10^{42}$ Mx^2 over a long period (0.5–a few days). Another significant finding is that the helicity accumulates at a nearly constant rate, (4.5–48)$\times 10^{40}$ Mx^2 hr^{-1}, and then becomes nearly constant before the flares. This led us to distinguish the helicity variation into two phases: a phase of monotonically increasing helicity and the following phase of relatively constant helicity. As expected, the amount of helicity accumulated shows a modest correlation with time-integrated soft X-ray flux during flares. However, the average helicity injection rate in the first phase shows even stronger correlation with the time-integrated soft X-ray flux. The physical implications of this result and the possibility that this characteristic helicity variation pattern can be used as an early warning sign for solar eruptions are discussed.

[1]This chapter is based on the following paper:
Park, S.-H., Lee, J., Choe, G. S., Chae, J., Jeong, H., Yang, G., Jing, J., & Wang, H. 2008, Astrophys. J., 686, 1397

3.1 Introduction

While the source of the magnetic helicity lies below the surface of the Sun, it was recently recognized as a useful parameter in describing solar features observed above the surface such as spiral patterns of sunspot fibrils, helical patterns in filaments and coronal mass ejections (CMEs; for a review, see Rust 1999). Naturally magnetic helicity studies have been directed to the energy buildup and instability leading to eruptions and CMEs (e.g., Rust 2001; Kusano et al. 2004b; Phillips et al. 2005).

More recently, several studies were carried out to relate the injection of magnetic helicity to the problem of impending or triggering solar flares. Moon et al. (2002b) studied the magnetic helicity injection around major flares to find its rapid helicity injection before flares, and concluded that a sudden helicity injection may trigger flares. Moon et al. (2002a) applied the same approach to 7 homologous flares in the active region, AR 8100, over a period of 6.5 hours to find a good correlation between the amount of incremental helicity and the soft X-ray flux during each homologous flare. The results from both studies thus point to the idea that the helicity injection occurring over short timescales (around a half hour) can be a significant factor in triggering flares.

Kusano et al. (2003b) proposed annihilation of magnetic helicity as a triggering mechanism for solar flares. Numerical simulations were carried, which show that, if the helicity is sharply reversed within a magnetic arcade, reconnection quickly grows in the helicity inversion layer, driving explosive dynamics. Yokoyama et al. (2003) studied flare activities in AR 8100 to find that most of the flare events occurred about half a day after the helicity injection rate changed its sign, and the positions of Hα emission in flares well correspond to the helicity inversion lines in space. Sakurai & Hagino (2003) studied two

active regions that appeared in 2001 (AR 9415 and 9661), both of which have produced X-class flares. Their finding was, on the contrary, that the magnetic helicity integrated over the regions evolved slowly and did not show abrupt changes at the time of the flares, although the distributions of magnetic helicity changed significantly over a few days in the regions.

In this chapter, long term (a few days) variations of the magnetic helicity around major X-class flares are studied. While some of the above studies suggest short-term helicity change as an important topic for flare triggering, Hartkorn & Wang (2004) found that the rapid helicity injection at the time of a flare can occur as an artifact under the influence of flare emission on the spectral line adopted in MDI measurements. This means that a short term variation during strong flares can hardly be measured with enough accuracy. This chapter is therefore focused on a long-term variation of the magnetic helicity in active regions to find a possible characteristic helicity evolution pattern that is associated with flare impending mechanisms.

3.2 Data Processing and Helicity Calculation

With the time-dependent measurement of longitudinal magnetic fields in the photosphere, the injection rate of the relative magnetic helicity can be approximately determined (Démoulin & Berger 2003). A simplified expression for the helicity injection rate (Chae 2001) given by Equation 2.11 is used to estimate helicity accumulation in active regions. In Equation 2.11, dS is the surface integral element and the integration is over the entire area of the target active region. Although this expression does not explicitly include the helicity injection by the vertical motion of field lines (see Kusano et al. 2002), Démoulin & Berger

(2003) pointed out that it actually accommodates both the vertical and horizontal motions of flux tubes as far as no flux tube newly emerges from or totally submerges into the surface. Note however that this requirement is not always met for all the active regions under investigation.

The quantities in Equation 2.11 are determined following the procedure described in Chae & Jeong (2005) with full disk MDI (Scherrer et al. 1995) magnetograms. First, B_n is approximately determined from the line-of-sight magnetic field B_l in the MDI magnetograms, simply considering the projection effect, i.e., $B_l = B_n \cos\psi$ where ψ is the heliocentric angle of the point of interest, assuming that the magnetic field on the solar photosphere is normal to the solar surface. Second, $\boldsymbol{A}_p$ is calculated from B_n by using the fast fourier transform (FFT) method as usual. The extent of the spatial domain of the FFT is taken about twice the width of the active region in order to minimize the artifacts arising from the periodic boundary condition in the fast Fourier transform (Alissandrakis 1981). Third, $\mathbf{v}_{LCT}$ is calculated using the LCT technique (November & Simon 1988). For LCT, all magnetograms are aligned in each event to the first image of the data set after correcting the differential rotation. The full width at half maximum (FWHM) of the apodizing window function and the time interval between two frames are set as $10''$ and 96 minutes, respectively. Then, LCT is performed for all pixels with an absolute flux density greater than 5 G. Only the pixels with cross correlation above 0.9 are considered. in constructing velocity maps.

In selecting data, it was found that use of 1 minute cadence full-disk MDI (Scherrer et al. 1995) magnetograms is adequate for the purpose of investigating the long-term helicity evolution. However, there are occasionally found data gaps in the 60 minute cadence

data set in which case the data gaps is supplemented with 96 minute MDI magnetograms. The time interval of the supplemented data set is therefore not longer than 96 minutes. To reduce the effect of the geometrical projection, the active regions lying within 60% of the solar radius from the apparent disk center are selected. Note that only full disk MDI magnetograms having $2'' \times 2''$ pixel size are used. Therefore the LCT velocities calculated here may have been systematically underestimated compared with the LCT velocities calculated with the higher resolution ($0.6'' \times 0.6''$) MDI data (Longcope et al. 2007).

After the helicity injection rate is determined as a function of time, the amount of helicity accumulation described in Equation 2.17 is calculated by integrating the injection rate with respect to time. If t_0 is a time when the magnetic field is in the potential state, ΔH_r is simply the helicity, $H_r(t)$, at time t. However, there is no guarantee that an active region in the potential energy state can be observed by chance. Therefore, t_0 is set as the earliest time without significant helicity accumulation at which the average value of the helicity injection rate over 4 hours is less than the nominal threshold in helicity injection rate, 1×10^{40} Mx^2 hr^{-1}. If that time cannot be determined, t_0 is defined as the time when the data set starts or when the previously accumulated helicity is released by a flare. The exact time of t_0 here is unimportant because it is only a trial value. After determining $H_r(t)$, t_0 is redefined as the time when the resulting helicity starts to increase from a nearly constant value.

3.3 Results

3.3.1 Magnetic Helicity Variation

The helicity variation calculated for the 7 active regions is presented in Figures 3.1 and 3.2. In both figures, the magnetic helicity accumulation is plotted together with the *GOES* soft X-ray light curve and magnetic flux as functions of time. The soft X-ray light curve is shown to indicate the flare times and the magnetic flux is shown to check the above-mentioned requirement for the approximation made in Equation 2.11. Note that the fluxes shown in this study are total unsigned magnetic flux, i.e., sum of the absolute amounts of positive and negative fluxes, because net magnetic flux may show little change despite significant flux change in each polarity.

For the events shown in Figure 3.1, the helicity accumulates at a monotonic rate of injection about 0.5–2 days before the flare onset, and then becomes almost constant before the flares. The magnetic helicity variation can be categorized into two stages: a phase of monotonically increasing helicity (phase I) and the following phase of relatively constant helicity (phase II). This pattern is obvious for the 4 flares (2001 October 25, 2004 November 7, and 2005 January 16 and 17). For the 2005 January 15 event, the helicity increased up to 22:00 UT on January 14 and then decreased afterward. In this case, the flare which occurred in phase II is not considered. It is then noted that these flares took place after a significant amount, $\sim(1.8\text{–}11)\times10^{42}$ Mx^2, of helicity accumulation.

Figure 3.2 shows the result for the other 4 active regions. Like the events in Figure 3.1, these flares also occurred after a significant helicity accumulation, $\sim(1.9\text{–}16)\times10^{42}$ Mx^2. However, they occurred in the middle of the continuous helicity accumulation, unlike those events shown in Figure 3.1. In other words, the flares in Figure 3.2 occurred in phase

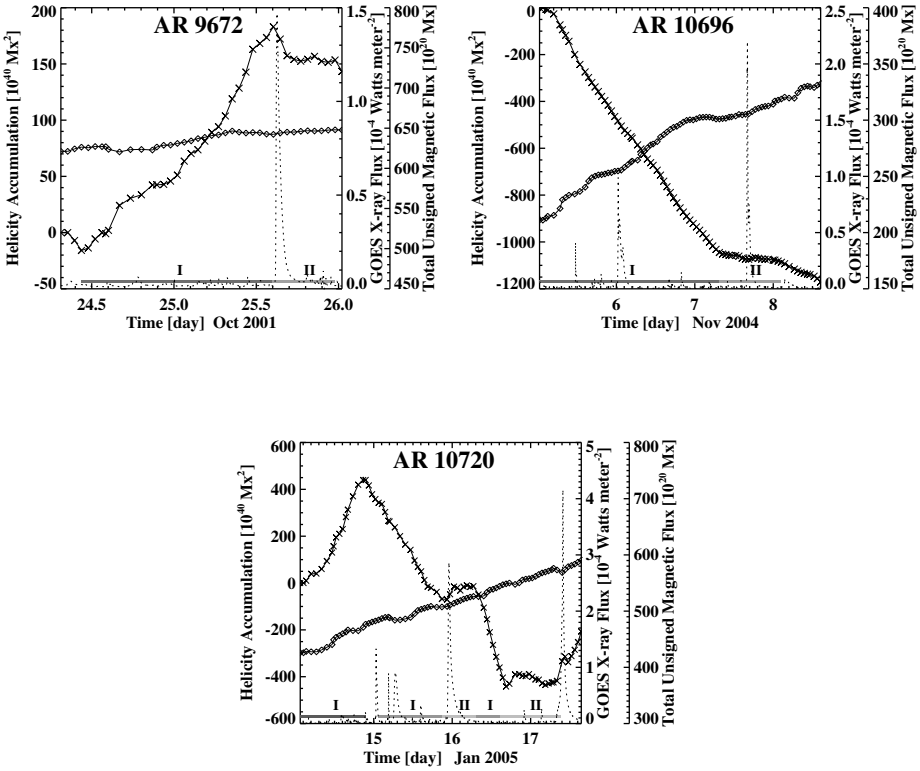

Figure 3.1 Time variations of helicity accumulation, magnetic flux, and *GOES* X-ray flux for 3 active regions. The helicity is shown as cross symbols and the magnetic flux is shown as diamonds. The *GOES* X-ray flux is shown as the dotted lines. Phase I, the interval over which the helicity accumulation is considered, and phase II, the following phase of relatively constant helicity, are marked.

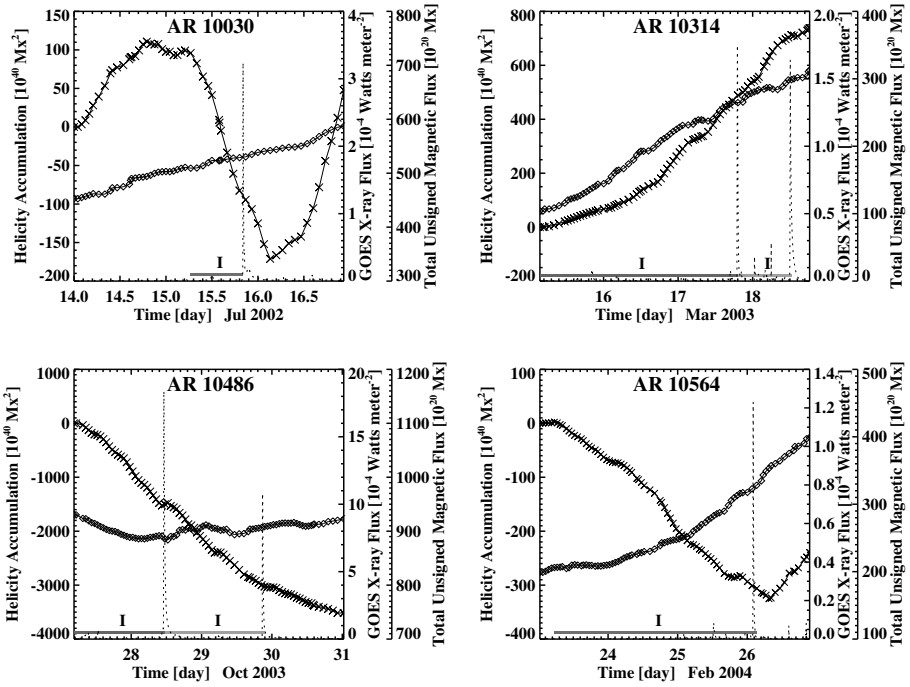

Figure 3.2 Same as in Fig. 1, but for additional events.

I, while those in Figure 3.1 occurred in phase II. One common trend is, however, that all the events are apparently associated with a considerable amount of helicity build-up before the flares, whether they occurred in phase I or in phase II. In case where flares occur in phase II, it may imply that solar active regions can wait for major flares after the helicity accumulated to some limiting amount. This is seemingly contrary to the general belief that a flare occurs as soon as the system reaches some threshold. An active region may evolve to a certain stage where the helicity no longer increases, and the system waits until it unleashes the stored energy by producing flares due to certain mechanism of triggering.

Since it is claimed that these large flares are always preceded by significant accumulation of helicity, as a reference it is required to check the corresponding helicity variation in non-flaring times. Figure 3.3 shows such data. For all active regions under investigation,

the amount of helicity injection during non-flaring periods (Figure 3.3) is much less than that around the major flare time. This convinces us that the above monotonically increasing helicity before major flares is a process associated with the flares and is not occurring in non-flare times. Another point to note in Figure 3.3 is that not only the helicity but also the total unsigned magnetic flux changes much less during the non-flaring time compared with the period before major flares. This implies that the increase of the magnetic helicity before major flares is, in part, related to the simultaneous increase of total unsigned magnetic flux.

It is also worthwhile to mention how the characteristic pattern of the helicity variation found here will depend on the sign of helicity. In the result obtained for the 7 active regions, similar amounts of both of positive and negative helicity were accumulated continuously and simultaneously during the whole time. It is therefore unlikely that counting the helicity in one and the other polarity separately yields a significantly different conclusion. On the other hand, some studies suggested that the sign-reversal of the helicity injection rate is important for flare activity so that it is needed to compare them with the present result. Kusano et al. (2003b) emphasized spatially sharp reversal of helicity sign triggers magnetic reconnection based on model simulation. In addition, Yokoyama et al. (2003) have found that flares tend to occur after reversal of helicity injection rate changed its sign. Although this is occasionally seen in the samples, (i.e., in the case of AR 10030 and AR 10720) as well, it is not always the case and it is not clear whether this is a necessary condition for the flares. More often than not, the helicity either remains constant or increases in one sign when the flare occurs. Note that this conclusion is valid only for the long term variation of helicity.

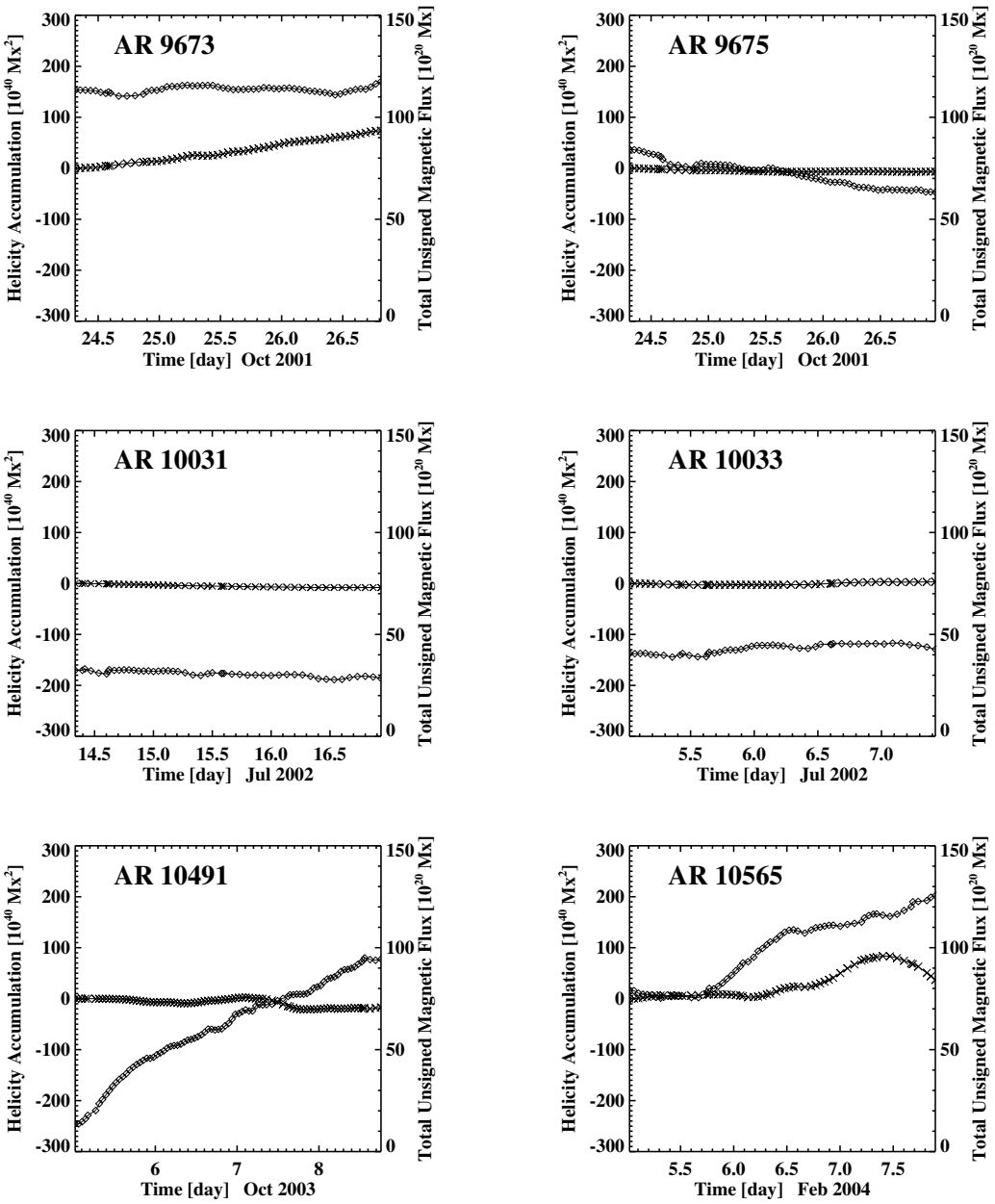

Figure 3.3 Time variations of helicity accumulation, and magnetic flux for 6 non-flare active regions. The helicity is shown as crosses, and the magnetic flux is shown as diamonds.

3.3.2 Correlation with Soft X-ray Flux

The helicity injection rate and the amount of helicity accumulation are compared with the *GOES* soft X-ray flux taken as the proxy for the flare energy release. In addition, the helicity accumulation time, $\Delta\tau$, defined as the time interval of helicity accumulation measured from t_0 and the first coming flare, is studied. Prior to making such a comparison, the range of uncertainty of each quantity needs to be known. In general it is hard to trace all the possible uncertainties involved with each quantity in Equation 2.11. Fortunately, the targeted quantity given by Equation 2.17 involves integration in space and time and the uncertainty in each measured quantity is not propagating, but rather may cancel out in the process of spatial and time integration if it is random in nature. Therefore, the uncertainty estimation is focused only on the linear approximation of the helicity variation. First, the best-fit linear function is found to the points, $\Delta H_r(t_i)$, lying in phase I (i.e., $t_0 \leq t_i \leq t_0 + \Delta\tau$) in the form of $F(t) = a(t - t_0) + F(t_0)$. Second, the standard deviation, σ, of the scatter points is calculated with respect to this linear function, and two additional lines corresponding to the $\pm\sigma$ levels of the scatter points are plotted. Finally, the y-axis and x-axis offsets of these two lines are used to determine $\sigma_{\Delta H_r}$ and $\sigma_{\Delta\tau}$, respectively. In addition, the uncertainty of the slope a itself is calculated in the form of $(\Delta H_r - \sigma_{\Delta H_r})/(\Delta\tau + \sigma_{\Delta\tau}) \leq a \leq (\Delta H_r + \sigma_{\Delta H_r})/(\Delta\tau - \sigma_{\Delta\tau})$. The center value of a here is taken as the average helicity injection rate, $|<\dot{H}_r>|$, in the rest of this chapter. Therefore, $|<\dot{H}_r>|$ is referred to as the best fit slope to ΔH_r (Equation 2.17) in phase I, but not as the average of the quantities given in Equation 2.11. The uncertainties shown in Figure 3.4 and Table 3.1 are those associated with the linear function fit only.

In Figure 3.4, the helicity parameters against the *GOES* soft X-ray fluxes integrated

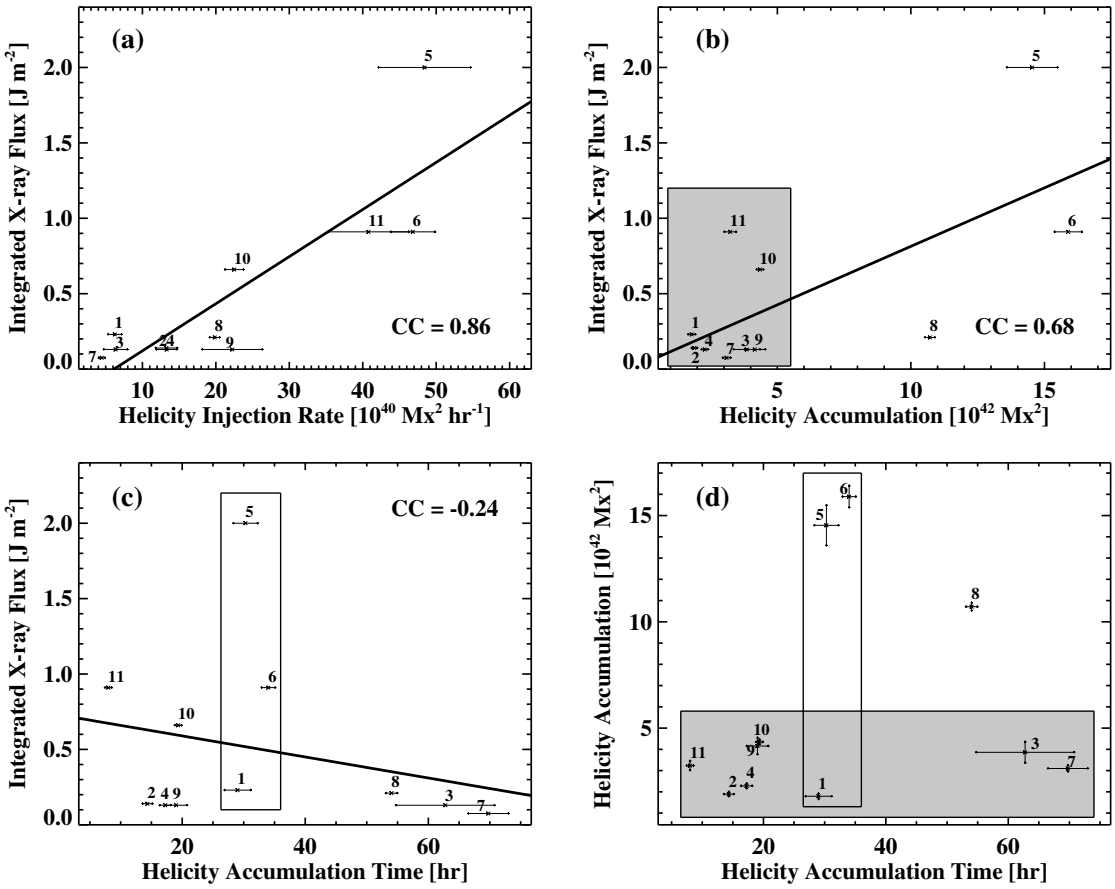

Figure 3.4 Helicity parameters with *GOES* X-ray flux integrated over the flaring time. Correlations of the integrated soft X-ray flux with (a) average helicity injection rate of phase I, (b) the amount of helicity accumulation during phase I, and (c) helicity accumulation time. The linear CC is specified in each panel. In (d), the amount of helicity accumulation is plotted as a function of the accumulation time. The uncertainties of the average helicity injection rate, the amount of helicity accumulation, and the helicity accumulation time are shown by error bars in each panel.

over the flaring time (F_X, hereafter) is plotted as cross symbols. Each symbol is identified with the event ID number in the figure together with uncertainty range represented by the bar (see also Table I). The solid lines show the least-squares linear fits to the data points. The CCs of the linear fits are also given in each panel. Figure 3.4a shows that there is a fairly good correlation (CC=0.88) between $|<\dot{H}_r>|$ and F_X. $|\Delta H_r|$ also shows a modest correlation with F_X (CC=0.69) as shown in Figure 3.4 b, although not as good as for $|<\dot{H}_r>|$. On the other hand, the correlation between $\Delta\tau$ and F_X is very poor with a weak tendency that the longer $\Delta\tau$, the weaker F_X (Figure 3.4c).

It was initially expected, on a general basis, that $|\Delta H_r|$ would strongly correlate with F_X. It is therefore puzzling why $\dot{H}_r$ shows even a better correlation with F_X in Figure 3.4. As a possibility, it is considered that $\Delta\tau$ may be a factor in complicating the relationship between $|\Delta H_r|$ and F_X. A intriguing idea is that the magnetic energy decays much faster than the magnetic helicity in the presence of magnetic diffusion (Berger 1999). If two initially identical systems have gained the same amount of magnetic helicity by the same process over different time spans, the system that acquired the helicity more quickly would then be in a higher energy state than the other. In this case, it may be that the helicity does not show a straightforward relationship with F_X depending on the accumulation time.

To check this hypothesis, $|\Delta H_r|$ is therefore compared with $\Delta\tau$ in Figure 3.4d. Two groups of events are marked as follows: one group of events with similar $|\Delta H_r|$ and different $\Delta\tau$ (marked with the gray colored box), and the other group with similar $\Delta\tau$ and different $|\Delta H_r|$ (the transparent box). The majority of the events are placed in the first group because all of them except three events numbered 5, 6, and 8, show comparable amounts of helicity change. Within this group, it can be shown that the events numbered 11, 10, 1, 3, and

7 follow the trend of increasing F_X with shorter $\Delta\tau$, as expected in the above hypothesis. However, the other events 2, 4, and 9 do not follow the trend. The second group contains only three events: 5, 6 and 1, that are selected to show a wide variation of F_X at similar $\Delta\tau$ (see the corresponding box in Figure 3.4c). If event 6 is ignored for the time being, the large difference between the integrated fluxes of the events 1 and 5 can be attributed to the corresponding difference in the accumulated helicity. Event 6 is certainly an exception to this tentative rule, but has a slightly longer $\Delta\tau$ than event 5, which is, qualitatively speaking, a condition for a smaller amount of energy for flaring. The general trend found in both groups is thus in agreement with the above hypothesis.

As a final check, an alternative grouping is considered. For instance, the events 2, 4, 9, 1, 3, and 7 are selected in Figure 3.4c as producing similar F_X over a wide range of $\Delta\tau$, which is just the opposite behavior expected under the above hypothesis. To justify such grouping the event 10 and 11 should be excluded. The events 2, 4, and 9 however show similar helicity change rate and $\Delta\tau$, and they practically represent one point in this scatter plot. On the other hand, the events 10 and 11 have helicity properties well distinguished from that of other events, and should not be excluded in search of any trend. The events 11, 10, 1, 8, 3, and 7 are responsible for the trend of increasing F_X with shorter $\Delta\tau$, and they should be grouped together. Since the events 2, 4, and 9 are exceptions to this trend, it is concluded that three out of eleven events do not agree with the hypothesis. The small number of events used in this study is another restriction for finding a trend here. With the present result alone, it is fair to presume that the weaker correlation between F_X and $|\Delta H_r|$ may arise from the inaccurate determination of the helicity accumulation amount due to the unknown initial time of helicity build-up.

3.4 Summary

The variation of magnetic helicity has been investigated over a time span of several days around the times of 11 X-class flares which occurred in the 7 active regions using MDI magnetograms. The major findings of this study are as follows.

First, a substantial amount of helicity accumulation is found before the flare in all the events. The helicity increases at a nearly constant rate, $(4.5–48)\times10^{40}$ Mx^2 hr^{-1}, over a period of 0.6–a few days, resulting in total amount of helicity accumulation in the range of $(1.8–16)\times10^{42}$ Mx^2. Such a wide range of helicity accumulation indicates that each active region has its own limit of helicity storage to keep a stable magnetic structure in the corona. The finding of a monotonically increasing phase is similar to the earlier one by Sakurai & Hagino (2003) that the magnetic helicity integrated over the regions evolved slowly and did not show abrupt changes at the time of the flares. The helicity increase over days before the flares reconfirms the conventional idea that helicity accumulation by a certain amount is necessary for a large flare to occur (Kusano et al. 1995; Choe & Lee 1996).

Second, there is a strong positive correlation between $|<\dot{H}_r>|$ of phase I and the corresponding F_X. $|\Delta H_r|$ also correlates with F_X, as expected, but the correlation between $|<\dot{H}_r>|$ and F_X is stronger than that between $|<\dot{H}_r>|$ and F_X. This result probably implies that the helicity injection rate is more accurately determined than the amount of helicity injection itself as the initial time of helicity build-up is poorly determined.

If the above correlations hold for a large number of events, it may be possible to predict the flare strength (e.g., F_X) based on the helicity injection rate. Monitoring of helicity variation in target active regions may also aid the forecasting of flares. A warning sign of flares can be given by the presence of a phase of monotonically increasing helicity,

as it is found that all the major flares occur after significant helicity accumulation. As a reference, it has been checked that the 6 active regions in non-flaring times have much lower helicity injection rates compared with those of the 7 active regions around the major flares. Therefore, it is concluded that the magnetic helicity can be a powerful tool for predicting major flares. This motivates the further statistical study in the next chapter.

Table 3.1 List of Flares, Helicity and Accumulation Time

ID	Flares	AR Number	Peak time (UT)	F_X[a] (10^{-1} J m^2)	$\lvert<\dot{H}_r>\rvert$[b] (10^{40} Mx^2 hr^{-1})	$\lvert\Delta H_r\rvert$[c] (10^{42} Mx^2)	$\Delta\tau$[d] (hr)
1	X 1.3 on Oct 25, 2001	9672	15:02	2.3	6.2±0.9	1.8±0.1	29±2
2	X 3.0 on Jul 15, 2002	0030	20:08	1.4	13.3±1.5	1.9±0.1	14±1
3	X 1.5 on Mar 17, 2003	0314	19:05	1.3	6.4±1.6	3.9±0.5	63±8
4	X 1.5 on Mar 18, 2003	0314	12:08	1.3	13.3±1.4	2.3±0.1	17±1
5	X 18 on Oct 28, 2003	0486	11:10	20.0	48.4±6.3	14.5±0.9	30±2
6	X 10 on Oct 29, 2003	0486	20:49	9.1	46.8±3.0	15.9±0.5	34±1
7	X 1.2 on Feb 26, 2004	0564	02:03	0.75	4.5±0.4	3.1±0.1	70±3
8	X 2.2 on Nov 07, 2004	0696	16:06	2.1	19.8±0.7	10.7±0.2	54±1
9	X 1.3 on Jan 15, 2005	0720	00:43	1.3	22.2±4.1	4.2±0.4	19±2
10	X 2.8 on Jan 15, 2005	0720	23:00	6.6	22.5±1.2	4.3±0.1	19±1
11	X 4.1 on Jan 17, 2005	0720	09:52	9.1	40.8±5.5	3.2±0.2	8±1

[a] Integrated *GOES* X-ray flux.

[b] Average helicity injection rate of phase I.

[c] The amount of helicity accumulation during phase I.

[d] Helicity accumulation time.

CHAPTER 4

PRODUCTIVITY OF FLARES AND MAGNETIC HELICITY INJECTION IN ACTIVE REGIONS

The main objective of this chapter[1] is to better understand how magnetic helicity injection in an active region is related to the occurrence and intensity of solar flares. Magnetic helicity injection rate and unsigned magnetic flux, as a reference, are therefore studied. In total, 378 active regions are analyzed using *SOHO*/MDI magnetograms. The 24 hr averaged helicity injection rate and unsigned magnetic flux are compared with the flare index and the flare-productive probability in next 24 hr following a measurement. In addition, the variation of helicity is investigated over a span of several days around the times of the 19 flares above M5.0 that occurred in selected strong flare-productive active regions. The major findings of this study are as follows: (1) for a sub-sample of 91 large active regions with unsigned magnetic fluxes in the range from 3 to 5×10^{22} Mx, there is a difference in magnetic helicity injection rate between flaring active regions and non-flaring active regions by a factor of 2; (2) the *GOES* C-flare-productive probability as a function of helicity injection displays a sharp boundary between flare-productive active regions and flare-quiet ones; (3) the history of helicity injection before all the 19 major flares displayed a common characteristic: a significant helicity accumulation of $(3–45)\times10^{42}$ Mx^2 during a phase of monotonically increasing helicity over 0.5–2 days. These results support the notion that helicity injection is important in flares, but it is not effective to use it alone for the purpose

[1]This chapter is based on the following paper:
Park, S.-H., Chae, J., & Wang, H. 2010, Astrophys. J., 718, 43.

of flare forecast. It is necessary to find a way to better characterize the time history of helicity injection as well as its spatial distribution inside active regions.

4.1 Introduction

It is generally thought that flare-productive active regions exhibit complex and non-potential magnetic structures related to the stored magnetic energy to power flares. For this reason, many studies of relationship between the solar flare and photospheric magnetic field properties have been carried out since the flare was first observed and recorded by Carrington (1859) and Hodgson (1859). Some examples include the unbalanced changes in the photospheric line-of-sight magnetic field (Cameron & Sammis 1999; Spirock et al. 2002; Wang et al. 2002); rapid changes of the sunspot structure associated with a substantial fraction of flares (Liu et al. 2005; Deng et al. 2005; Wang et al. 2004a, 2005; Chen et al. 2007); the magnetic shear angle evolution (Hagyard et al. 1984; Hagyard & Rabin 1986; Sivaraman et al. 1992; Schmieder et al. 1994; Wang et al. 1994, 2004a); the horizontal gradient of longitudinal magnetic fields (Zirin & Wang 1993; Zhang et al. 1994; Tian et al. 2002); electric current (Canfield et al. 1993; Lin et al. 1993); magnetic helicity injection (Moon et al. 2002a,b; Sakurai & Hagino 2003; Yokoyama et al. 2003; Park et al. 2008). Based on the above-mentioned studies, current flare forecasting models are moving toward multiple-magnetic parameter-based approaches (Leka & Barnes 2003a,b; Li et al. 2008) from sunspot-morphological evolution-based approaches (McIntosh 1990; Gallagher et al. 2002).

Magnetic helicity studies have been carried out to understand an energy buildup process and a triggering mechanism of solar flares. There were a number of studies related

to a rapid magnetic helicity change as an impending condition or a trigger for solar flares (e.g., Moon et al. 2002a,b). LaBonte et al. (2007) surveyed magnetic helicity injection in 48 X-class flaring active regions and 345 non-X-class flaring regions, and found that a necessary condition for the occurrence of an X-class flare is that the peak helicity flux has a magnitude $> 6\times10^{36}$ Mx^2 s^{-1}. Park et al. (2008) found that a substantial amount of helicity is accumulated before the flare in all the 11 X-class flare events, and suggested a warning sign of flares can be given by the presence of a phase of monotonically increasing helicity. Motivated by these results, in this chapter, the feasibility of using magnetic helicity to build a flare forecasting system is explored with a data sample covering almost one solar cycle.

4.2 Data and Analysis

Using a set of the full-disk 96 minute MDI (Scherrer et al. 1995) magnetogram data, 24 hr profiles of magnetic helicity injection rate and unsigned magnetic flux of an active region are determined. Note that the newly calibrated level 1.8.2 MDI magnetograms are employed in this study. The level 1.8.2 MDI data have been available since 2008 December 24, and its magnetic field value on average over the solar disk increased by a factor of $\sim$1.6 compared to that of the previous level 1.8 data (Tran et al. 2005; Ulrich et al. 2009). A total of 378 active regions were selected during the time period from mid-1996 to 2006, almost the entire duration of Solar Cycle 23. Normally each data set corresponding to a given active region has around 15 MDI magnetograms covering 24 hr during its disk passage. To reduce the effect of the geometrical projection in calculation of the normal component of the magnetic field, the start time of each data is set as the time when the corresponding active region appears or rotates to a position within 0.6 of a solar radius from the apparent

disk center.

The unsigned magnetic flux, Φ, of the entire area of a given active region is defined by:

$$\Phi = \int_s |B_n| \, dS, \tag{4.1}$$

where dS is the surface integral element and the integration is over the entire area of the target active region. B_n is approximately determined from B_l in the MDI magnetograms, assuming that the magnetic field on the solar photosphere is normal to the solar surface, i.e., $B_l = B_n \cos\psi$ where ψ is the heliocentric angle of the point of interest. $\dot{H}_r$ and ΔH_r of an entire active region are calculated from Equations 2.11 and 2.17 following the same procedure described in Section .

For each of the 378 active region data sets, the uncertainty of the helicity injection rate corresponding to measurement uncertainty ($\sim$20 G) of MDI magnetograms is estimated as follows. First, pseudo-random noise is added to each magnetogram. The noises have normal distribution with the standard deviation of 20 G. Then $\dot{H}_r$ described in Equation 2.11 is calculated. The same process is repeated 10 times for the same active region domain with different sets of errors to calculate the standard deviations of $\dot{H}_r$. Finally, the average of the standard deviations during the entire 24 hr period is considered as the uncertainty of the helicity calculation for each active region data set. It is found that the average uncertainty of $\dot{H}_r$ is around 5% so that it does not significantly affect the helicity calculation and conclusion of the study.

From the time profiles of $\dot{H}_r$ and Φ, the two average parameters are defined to investigate their feasibility for flare forecasting as follows. The first parameter is the absolute value of the average helicity injection rate, $|<\dot{H}_r>|$, which indicates the average amount of

injected helicity per unit time to an entire active region defined by:

$$|<\dot{H}_r>| = \frac{\sum_{t_0}^{t_1} |\dot{H}_r|}{N}, \tag{4.2}$$

where t_0 is the start of each data set under investigation, t_1 is 24 hours after t_0, and N is the total number of MDI magnetograms in each data set during the time period, Δt, between t_0 and t_1. As for the second parameter, the average unsigned magnetic flux, $<\Phi>$, is used with:

$$<\Phi> = \frac{\sum_{t_0}^{t_1} \Phi}{N}, \tag{4.3}$$

where t_0, t_1, and N are the same as defined Equation 4.2. These parameters were studied by many authors before so that it is used as a reference in this study. Please refer to the other two helicity parameters which are the maximum values of the data sets of absolute helicity injection rate, $|\dot{H}_r|$, and absolute helicity accumulation, $|\Delta H_r|$. They show a similar correlation result with flare productivity as $|<\dot{H}_r>|$ so that in this study $|<\dot{H}_r>|$ is only represented as a helicity parameter.

To investigate a relationship between these two parameters of an active region and flares occurred in the region for the following day of the parameters' measurement, the flare index, F_{idx}, which represents each active region's average daily *GOES* soft X-ray peak flux is used. F_{idx} was first introduced by Antalova (1996) and was later applied by Abramenko (2005):

$$F_{idx} = \left(100S^{(X)} + 10S^{(M)} + 1.0S^{(C)} + 0.1S^{(B)}\right)/\tau, \tag{4.4}$$

where τ is the time interval (measured in days) and $S^{(i)}$ is the sum of *GOES* flare significants in the ith *GOES* class over τ. This flare index is calculated for each active region, and

τ is selected to be 1 to evaluate the flare productivity of a given region for the time window of the next day following Δt. Note that in the *GOES* soft X-ray flare catalog, there are some X-ray events of which locations (indicated as NOAA active region numbers) are unknown so that it might affect the results; however, these are typically weaker events. Wheatland (2001) reported that of the C-class flares in the catalog during the period 1981–1999, 61.5% are identified with an active region, while of the M- and X-class flares the fractions are 82% and 94%, respectively.

4.3 Results

Figure 4.1 presents 24 hr profiles of $\dot{H}_r$ and Φ for all the 378 active regions with three different groups classified by the flare index ranges which are $F_{idx} \geq 10$ (51 samples, left column), $1 \leq F_{idx} < 10$ (74 samples, middle column), and $F_{idx} < 1$ (253 samples, right column). Note that F_{idx} values of 1, 10, and 100 are equivalent to the specific flare productivity of one C 1.0, M 1.0, and X 1.0 flare per day, respectively. The dotted lines show the average of the maximum values for $|\dot{H}_r|$ (top panels) and Φ (bottom panels) of the samples in each panel. As it is anticipated, there is a general trend that the larger F_{idx} an active region has, the larger values of helicity injection rate and unsigned magnetic flux it represents. This trend is more evident in the case of $\dot{H}_r$; the average value (46×10^{40} Mx^2 hr^{-1}) of the samples for $F_{idx} \geq 10$ is almost twice greater than that (25×10^{40} Mx^2 hr^{-1}) of the samples for $1 \leq F_{idx} < 10$ and about 4.5 times greater than that (10×10^{40} Mx^2 hr^{-1}) of the samples for $F_{idx} < 1$. For the active regions having the large F_{idx}, it is found that although the magnetic flux does not change too much in time, the helicity, however, accumulates significantly and consistently. This finding agrees with the previous study by Park et al. (2008) that 11 X-

class flares are preceded by a monotonically significant helicity accumulation, 10^{42}–10^{43} Mx^2 over a period of half to a few days.

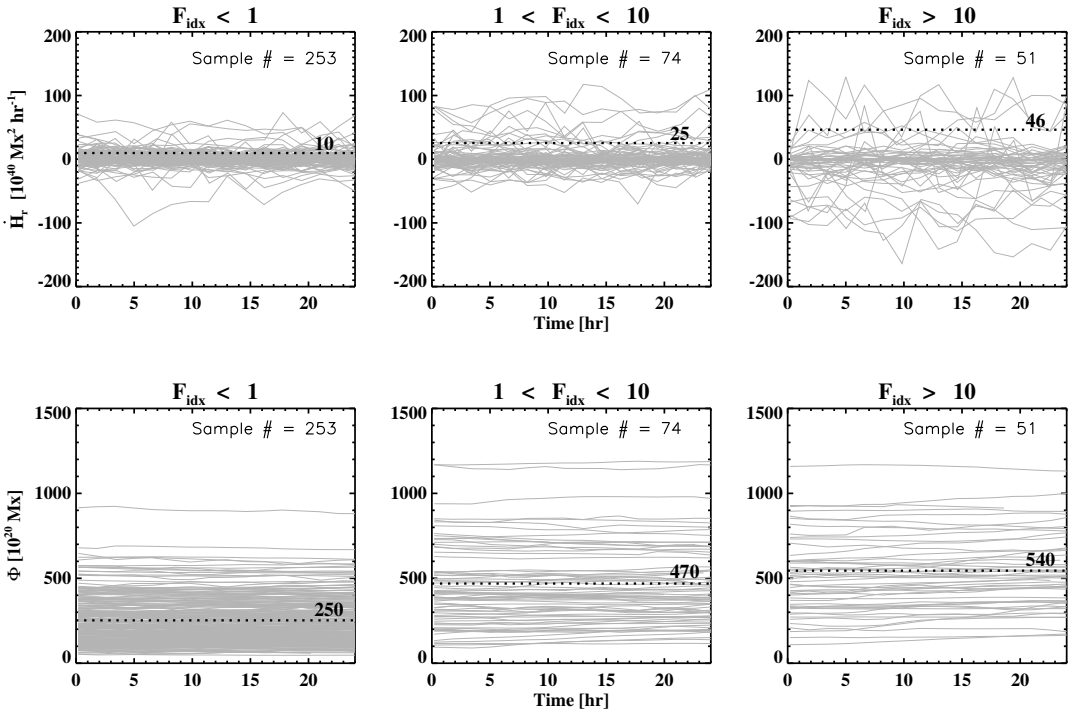

Figure 4.1 24 hr profile of magnetic helicity injection rate, $\dot{H}_r$, and unsigned magnetic flux, Φ. It shows three different groups classified by the ranges of flare index, F_{idx}, which are $F_{idx}<1$ (left column), $1\leq F_{idx}<10$ (middle column), and $F_{idx}\geq 10$ (right column). The number of samples in the three groups is specified in each panel. The average maximum values for $|\dot{H}_r|$ (top panels) and Φ (bottom panels) of the samples in each panel are plotted as dotted lines.

To examine how $\dot{H}_r$ and Φ are related to flare productivity, the two average parameters ($|<\dot{H}_r>|$ and $<\Phi>$) are studied in more detail for the 378 active regions (see Table 4.1 for the statistical properties of the parameters) and compared with F_{idx} taken as the proxy for the flare productivity in the next day following the measurement of the parameters. By only considering the 153 samples with non-zero flare index, in Figure 4.2, F_{idx} versus $|<\dot{H}_r>|$ and $<\Phi>$ are plotted, as cross symbols, in a logarithmic scale. The solid and dotted lines show the least-squares linear fit and its standard deviation to the data points. The

CCs and the power law index of the linear fits are also given in each panel. While the data points are widely scattered, there is a moderate correlation between the parameters and the flare index with a tendency that the larger the parameters the larger the flare index. CCs of F_{idx} versus $|<\dot{H}_r>|$ and $<\Phi>$ are 0.42 and 0.43, respectively. In Figure 4.2, the other 225 samples with zero flare index are marked as square symbols using F_{idx} = 0.05 for the plotting purpose only. Note that the zero flare index samples are excluded from the linear fit. In the rescaled range of each parameter (the maximum value of the samples is considered as 1 and the minimum as 0), most of the data samples of the helicity parameter are distributed in the range less than 0.2 with flare indexes near zero values, and a few samples are scattered in the range greater than 0.2 with relatively high flare indexes. Instead, $<\Phi>$ has well-distributed data samples. This difference would make it easier to define a critical value for the helicity parameter to forecast flare-active or flare-quiet conditions.

Furthermore, it is interesting to investigate why some of the samples with the large parameters do not produce major flares. Therefore, two groups of samples were selected and their average values for each of the two parameters were compared. The first group contains the samples with $F_{idx} \geq 1$ and the relatively large parameters (hereafter, *flaring* group), and the samples in the second group are picked out from the same range of the parameters as those in the *flaring* group but produced no flares (hereafter, *non-flaring*

Table 4.1 Statistical Properties of the Two Magnetic Parameters

X	$X_{\min}$	$X_{\max}$	X_{med}[a]	X_{avg}[b]	X_{stv}[c]
$\lvert<\dot{H}_r>\rvert$ (10^{40} Mx^2 hr^{-1})	0.011	94.6	2.15	7.42	14.9
$<\Phi>$ (10^{20} Mx)	51.5	1180	274	320	206

[a]The median value of X

[b]The average value of X

[c]The standard deviation of X

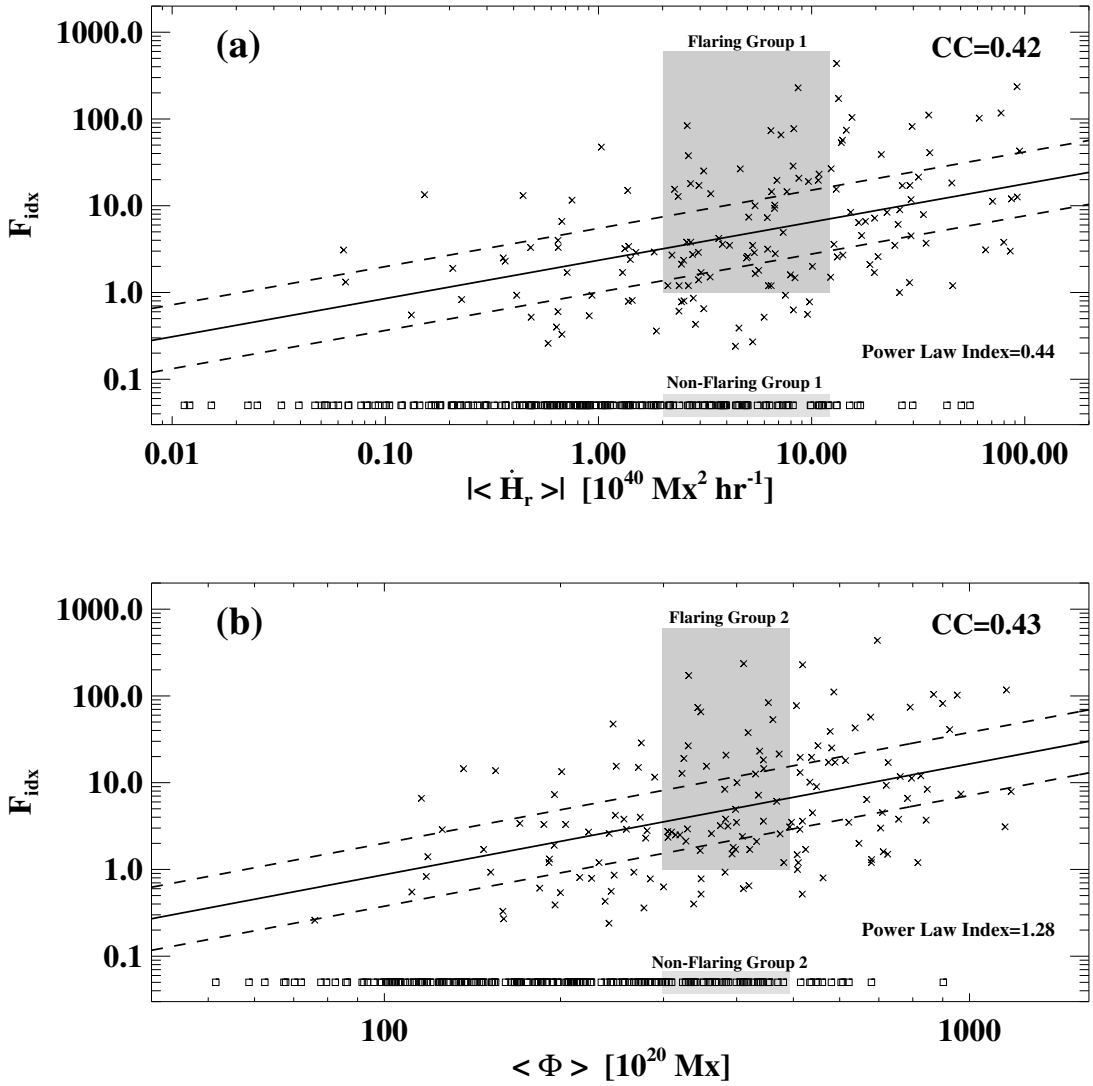

Figure 4.2 Flare index, F_{idx}, vs. magnetic parameters. Correlations of F_{idx} with (a) the absolute average helicity injection rate, $|<\dot{H}_r>|$, and (b) the average unsigned magnetic flux, $<\Phi>$, in a logarithmic scale. The solid and dotted lines show the least-squares linear fit and its standard deviation to the data points. The linear CC is specified in each panel. The total number of samples used for the correlation studies is 153 marked as cross symbols. The other 225 samples with zero flare index are marked as square symbols with a small value F_{idx} = 0.05 for the plotting purpose only.

group). For the comparison, the *flaring* and *non-flaring* groups for the parameters of $|<\dot{H}_r>|$ and $<\Phi>$ are considered. The samples in the *flaring* and *non-flaring* groups are marked with the gray boxes in each panel of Figures 4.2a and 4.2b. First, for a sub-sample of 118 active regions with large $|<\dot{H}_r>|$ in the range from 2 to 10×10^{40} Mx^2 hr^{-1} (Figure 4.2a), the *flaring* group has the average unsigned magnetic flux of 3.7×10^{22} Mx, greater than that of the *non-flaring* group, 3×10^{22} Mx. This difference is not significant. However, for a sub-sample of 91 active regions in the range, (3–5)$\times10^{22}$ Mx, of large $<\Phi>$ (Figure 4.2b), the *flaring* group has $|<\dot{H}_r>|$ about twice greater than that of the *non-flaring* group. This indicates that in an active region with large flux, a large amount of consistent helicity injection is essential to the occurrence of flares. Please refer to Table 4.2 for the detailed values of these comparisons.

Table 4.2: Comparison of the Two Magnetic Parameters for *Flaring* Groups and *Non-flaring* Groups

	Flaring Group 1	*Non-flaring* Group 1	*Flaring* Group 2	*Non-flaring* Group 2
Sample Number	56	62	44	47
$\lvert<\dot{H}_r>\rvert$ (10^{40} Mx^2 hr^{-1})	4.68	4.73	6.85	3.48
$<\Phi>$ (10^{20} Mx)	368	297	385	377

In Figure 4.3, $<\Phi>$ versus $|<\dot{H}_r>|$ is plotted in a logarithmic scale for the 378 samples with $F_{idx}<0.1$ as plus symbols, $0.1<F_{idx}<10$ as triangle, and $F_{idx}>10$ as square. F_{idx} is derived for the three different time windows of the first day (Figure 4.3, top) following Δt, the second day (Figure 4.3, middle), and the third day (Figure 4.3, bottom). In each plot, four sections are determined by the vertical and horizontal dashed lines marking the median values of both the parameters for the samples. By only considering the samples in each of the four sections, the probability of flare occurrence classified by two groups

of criteria $F_{idx}\geq 10$ and $F_{idx}\geq 0.1$ are calculated, and they are marked as black and gray colored numbers in each section. It is found that the flaring probability in the upper right section is not only much greater than those in the upper left and lower right sections but also the probability in the lower right section is always greater than that in the upper left section except only one case for the flare criterion of $F_{idx}\geq 0.1$ in the second day; especially for the cases of the flare criterion of $F_{idx}\geq 10$, the probability in the lower right section is almost 2–5 times greater than that in the upper left section. This remarkable thing indicates that magnetic helicity injection will contribute extra weight to improve the flare prediction based on the total unsigned magnetic flux. Another finding is that the flaring probability in the upper right section shows its maximum at the first day time window and it keeps going down for the second and third days. However, for the case of the lower left section, the flaring probability indicates the minimum at the first day and the maximum at the second day. This suggests that the flare forecasting based on the parameters would be best for time window 0–24 hr after the measurement of the parameters.

To make this study more useful for flare forecasting, the probability of flare occurrence is calculated as a function of each parameter of $|<\dot{H}_r>|$ and $<\Phi>$ for the 3 day time window, $\tau_{3\text{-day}}$, following Δt. For this investigation, the flare-productive probability in the ith *GOES* class, P_i, is used with:

$$P_i(X) = \frac{S_i{}^A(\geq X)}{S^T(\geq X)}, \tag{4.5}$$

where i represents the *GOES* flare class and X is a value of each parameter. $S_i{}^A(\geq X)$ is the number of active samples producing at least one i-class flare during $\tau_{3\text{-day}}$, and $S^T(\geq X)$

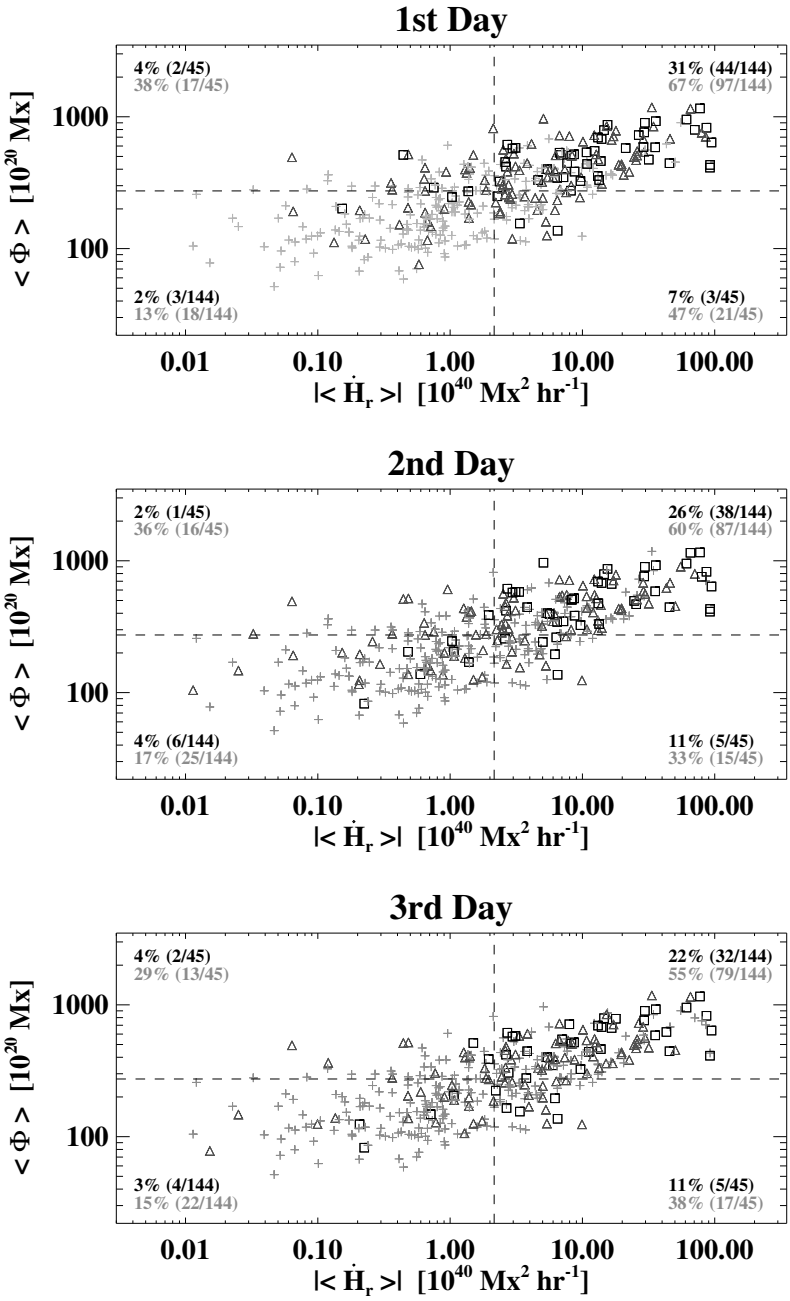

Figure 4.3 $<\Phi>$ vs. $|<\dot{H}_r>|$ for the 378 active region samples with $F_{idx}<0.1$ as plus symbols, $0.1<F_{idx}<10$ as triangle, and $F_{idx}>10$ as square. F_{idx} is calculated for the three different time windows of the first day (top) following the 24 hr period of the measurement of the parameters, second day (middle), and third day (bottom). The vertical and horizontal dashed lines, in each plot, mark the median values of both the parameters and divide the domain into four sections. For the samples in each of the four sections, the probability of flare occurrence is calculated with two criteria $F_{idx}\geq 10$ and $F_{idx}\geq 0.1$, and marked as black and gray colored numbers in each section.

is the number of the total sample in the range $[X,\infty]$. Figure 4.4 shows P_i corresponding to 14 points of the parameters for C-class as diamond symbols, M-class as triangles, and X-class as squares. Gray bars represent the number of the total $S_T(\geq X)$, and the dotted line denotes the range where $S_T(\geq X)$ is greater than 10, which maybe considered as statistically meaningful. The ratio of all the active samples in the total sample is 46%, 14%, and 3% for C-, M-, and X-classes, respectively. In case of P_i as a function of $<\Phi>$, there is a fairly good linear correlation in the range of (50–570)$\times 10^{20}$ Mx of $<\Phi>$, and the number of total samples decreases gradually. Instead, the helicity parameter shows a sharp increase in P_i and a significant decrease in the number of total samples in the rescaled range of 0–0.15 of the parameter. P_C as a function of $|<\dot{H}_r>|$, especially, quickly reaches up to $\sim$90% from 46% in the very low rescaled range, 0–0.15, of the parameter, and it retains a high value above 90% in the rest, 0.15–0.6, of the statistically meaningful range. This trend indicates that the helicity parameter can be used for differentiation between C-flare-productive and C-flare-quiet active regions. Please refer to Table 4.3 for further details.

For the evaluation of skill scores and success rates of the flare forecasting using the two magnetic parameters, a 2×2 contingency table analysis commonly used by the meteorological and space physics communities (e.g., Fry et al. 2001, 2003) is adopted. In the contingency table, there are four categories of hit, false alarm, miss, and correct null marked as *a*, *b*, *c*, and *d* in Table 4.4, respectively, and defined as follows: *a* is the number of active region samples that are predicted to produce a flare and observed with at least one flare above M-class within the 3-day time window $\tau_{3\text{-day}}$; *b* is the number of samples predicted to produce a flare but not observed with any flares within $\tau_{3\text{-day}}$; *c* is the number of samples predicted to be flare-quiet but observed with at least one flare above M-class

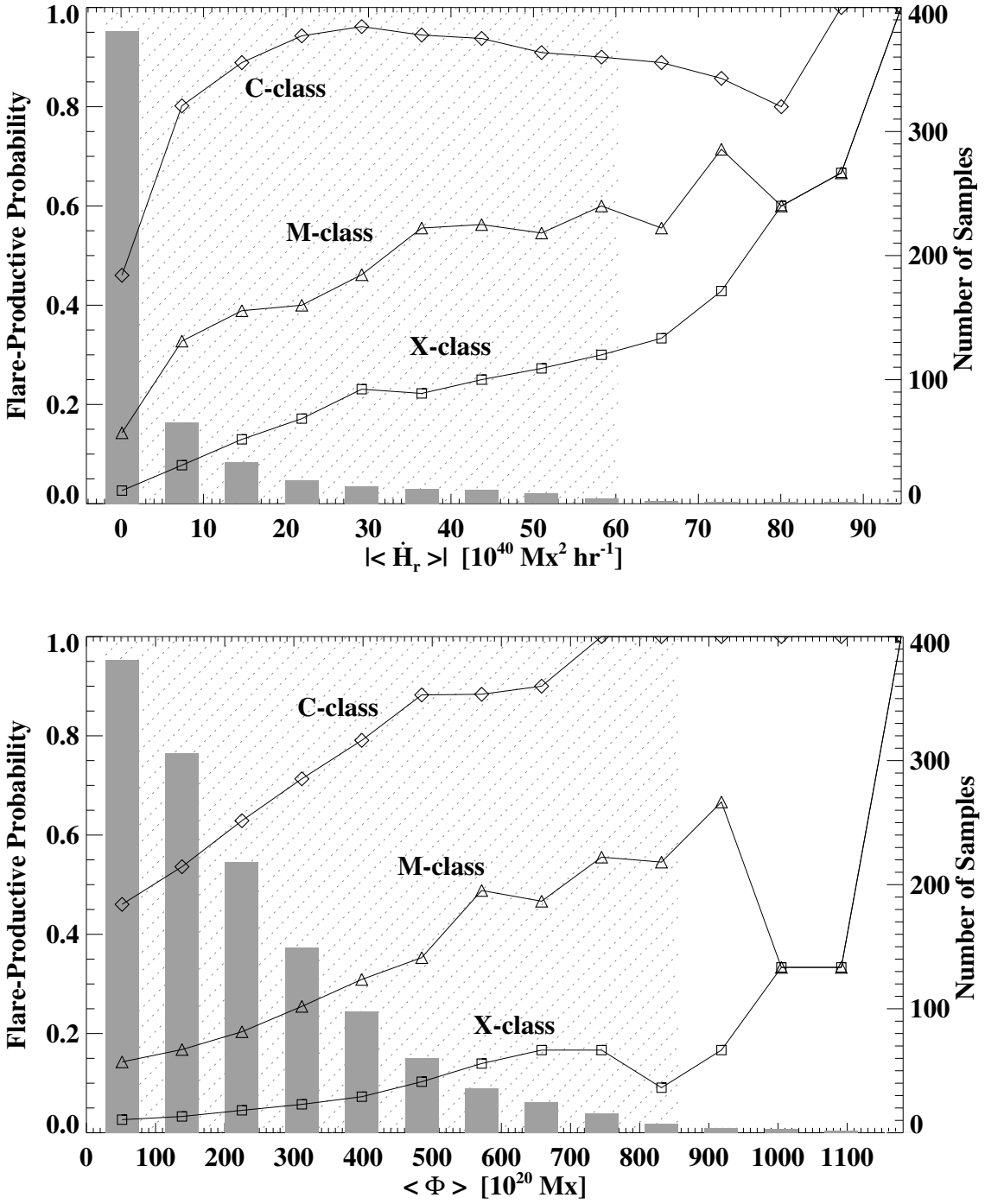

Figure 4.4 Flare-productive probability, P_i, vs. magnetic parameters. The probabilities producing at least one C-, M-, and X-class flare during $\tau_{3\text{-}day}$ are shown as diamond, triangle, and square symbols, respectively. Gray bars represent the number of samples and the dotted line denotes the range where the number of the total samples is greater than 10.

Table 4.3: Number of Active Regions Producing at Least One Flare in the *i*th *GOES* Class During $\tau_{3\text{-day}}$ as a Function of Magnetic Parameters

GOES Class	Absolute average helicity injection rate $\lvert<\dot{H}_r>\rvert$ (10^{40} Mx^2 hr^{-1})									
	≥0.1	≥7.4	≥14.6	≥21.9	≥29.2	≥36.5	≥43.7	≥51.0	≥58.3	≥65.5
C-class	174(378)	93(116)	48(54)	33(35)	25(26)	17(18)	15(16)	10(11)	9(10)	8(9)
M-class	54(378)	38(116)	21(54)	14(35)	12(26)	10(18)	9(16)	6(11)	6(10)	5(9)
X-class	10(378)	9(116)	7(54)	6(35)	6(26)	4(18)	4(16)	3(11)	3(10)	3(9)
GOES Class	Average unsigned magnetic flux $<\Phi>$ (10^{20} Mx)									
	≥52	≥138	≥225	≥312	≥398	≥485	≥572	≥658	≥745	≥832
C-class	174(378)	163(304)	139(221)	112(157)	87(110)	60(68)	38(43)	27(30)	18(18)	11(11)
M-class	54(378)	51(304)	45(221)	40(157)	34(110)	24(68)	21(43)	14(30)	10(18)	6(11)
X-class	10(378)	10(304)	10(221)	9(157)	8(110)	7(68)	6(43)	5(30)	3(18)	1(11)

Note. — Total number of samples are marked by parenthesis.

within $\tau_{3\text{-day}}$; and d is the number of samples that were predicted to remain flare-quiet and did so within $\tau_{3\text{-day}}$. In order to make a prediction on whether or not an active region will produce a flare, a threshold of each of the two parameters is determined as the value which makes the maximum of the Heidke skill score (HSS, hereafter) from the data sets:

$$\mathrm{HSS} = \frac{(a+d-e)}{(N-e)}, \tag{4.6}$$

where N=a+b+c+d is the total number of samples and e=[(a+c)(a+b)+(b+d)(c+d)]/N is the number of correct forecasts by chance. HSS measures the fraction of the correct forecasts after eliminating those forecasts which would be correct due purely to random chance (Balch 2008). The positive values of HSS indicate that the forecasting performance is better than predictions by chance, and a maximum score of +1 means all correct predictions. The maximum values of HSS for $\lvert<\dot{H}_r>\rvert$ and $<\Phi>$ are 0.32 and 0.35, respectively. In addition, by using Fisher's linear discriminant analysis, a threshold is found considering both

the parameters. However, the maximum HSS is 0.34 which is similar to that of each parameter. This is understandable because magnetic helicity and flux are dependent on each other somehow. For an additional assessment of the forecasting, the following quantities (Balch 2008; McKenna-Lawlor et al. 2006) are also considered:

$$\mathrm{POD} = \frac{a}{(a+c)}, \tag{4.7}$$

$$\mathrm{FAR} = \frac{b}{(a+b)}, \tag{4.8}$$

$$\mathrm{TCC} = \frac{a}{(a+c)} + \frac{d}{(b+d)} - 1, \tag{4.9}$$

where POD is the probability of detection, FAR is the false alarm rate, and TCC is the true skill score used to evaluate the flaring and non-flaring accuracy. PODs are 56% and 39%, FARs are 64% and 51%, and TCCs are 39% and 32% for $|<\dot{H}_r>|$ and $<\Phi>$, respectively. Please see, in Table 4.4, the details of the contingency tables for $|<\dot{H}_r>|$ and $<\Phi>$, and the combination of $|<\dot{H}_r>|$ and $<\Phi>$.

Table 4.4: Contingency Table for Evaluating the Ability of the Flare Prediction by the Two Magnetic Parameters

				$\lvert<\dot{H}_r>\rvert$		$<\Phi>$		$\lvert<\dot{H}_r>\rvert$ & $<\Phi>$	
		Forecast		Forecast		Forecast		Forecast	
		Yes	No	Yes	No	Yes	No	Yes	No
Observation	Yes	a	c	30	24	21	33	22	32
	No	b	d	53	271	22	302	26	298
Total		a+b	c+d	83	295	43	335	48	330

Finally, Figure 4.5 presents long-term (a few days) variations of the magnetic helicity calculated for 8 active regions which have the flare indexes greater than 100. The

magnetic helicity accumulation (cross symbols) is plotted together with the *GOES* soft X-ray light curve (dotted line) and unsigned magnetic flux (diamond symbols) as a function of time. In the 8 active regions, there are 19 major flares with a *GOES* peak flux greater than M5.0, and they are marked with the ID numbers of 1–19 in Figure 4.5. For the AR 10696 and 10720, the helicity evolution pattern had already been examined over a span of several days around the times of X-class flares which occurred in those regions in the previous paper (see Park et al. 2008). In that paper, Park et al. (2008) concluded that each of major flares was preceded by a significant helicity accumulation, 10^{42}–10^{43} Mx^2 over a period of half to a few days. Another finding was that the helicity accumulates at a nearly constant rate, $(4.5–48)\times10^{40}$ Mx^2 hr^{-1}, and then becomes nearly constant before the flares for 4 out of 11 events. These tendencies were checked for other active regions in this study, and the major findings are as follows. First, there was always a significant helicity accumulation of $(3–45)\times10^{42}$ Mx^2 before all the 19 major flares with a phase of monotonically increasing helicity over $\sim$0.5–2 days. In principle, an increase of magnetic helicity can be achieved without a flux emergence and it is frequently shown during post-flare periods for some of active regions in Figure 4.5. However, the increasing helicity phase before the flares always accompanied the increasing phase of magnetic flux except AR 10652, and this might be an observational result supporting the MHD simulation studies (e.g., Fan & Gibson 2004) which show that the emergence of twisted flux ropes into pre-existing overlying field plays a critical role to produce major flares. Second, of the 19 flares, four flares (1, 5, 7, and 12) occurred when helicity injection rate becomes slow or almost zero after the significant helicity accumulation with fast injection rate. These flares are the additional examples for the almost constant helicity phase before a major flare reported by Park et al. (2008). In

addition to the above two phases of helicity injection, AR 9236 and 10720 seem to have an abnormal helicity evolution pattern before the major flares compared to the monotonically increasing pattern with one sign of helicity shown in the other active regions. A remarkable feature for both active regions is that the eight major flares (2, 3, 4, 13, 14, 15, 16, and 17) occurred during the period when the helicity injection rate started to reverse its sign so that the helicity starts to accumulate with opposite sign.

4.4 Summary and Discussion

The time variations of $\dot{H}$ and Φ have been investigated in 378 solar active regions, and the two average parameters, $|<\dot{H}_r>|$ and $<\Phi>$, have been compared with F_{idx}. Although there is a large amount of scatter in the data samples, a moderate correlation between the parameters and F_{idx} is found. The larger F_{idx} an active region has, the larger values of $\dot{H}$ and Φ it presents. To improve the correlation, a new parameter has been defined as an equally weighted linear combination of the two rescaled parameters (0.5 of each). The logarithmic-scale CC of F_{idx} versus the new parameter increased slightly to 0.47. It is not surprising because $|<\dot{H}_r>|$ is well correlated with $<\Phi>$ as shown in Figure 4.3. Moreover, by considering 48 and 72 hr profiles of $\dot{H}_r$ and Φ for calculation of the two average parameters, the same correlation study have been executed between the two parameters and the next-day flare index. It was found that the longer the period is for average, the worse the correlation will be, especially in the case of $|<\dot{H}_r>|$ (CC=0.38 and 0.21 for 48 and 76 hr periods, respectively). This might be because the flaring history before or during the measurement period of the parameters is not considered, but the parameters are compared with F_{idx} calculated only for the following day of the measurement period.

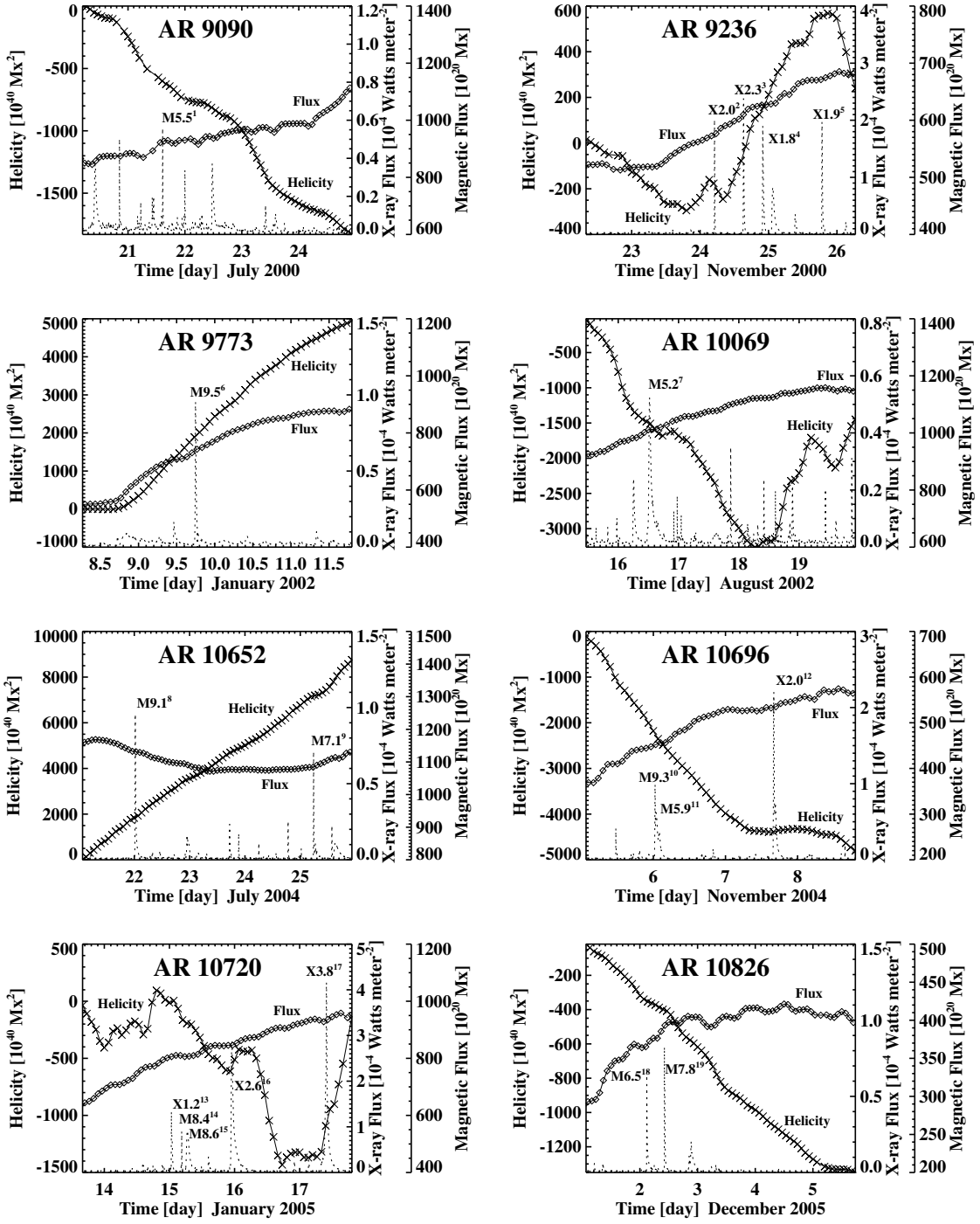

Figure 4.5 Time variations of helicity accumulation, magnetic flux, and *GOES* soft X-ray flux for 8 active regions which have the flare indexes greater than 100. The helicity is shown as cross symbols and the magnetic flux is shown as diamonds. The X-ray flux is shown as dotted lines and all the 19 flares above *GOES* M5.0 level are marked with their ID numbers.

It is understandable that no matter which method is used, the correlation between the parameters and flare index is not high. This is an intrinsic problem for flare forecasting as the occurrence of a flare depends not only on the amount of magnetic energy built up in an active region, but also on how it is triggered. For example, if new flux-rope emergence is the driver of flares (Schrijver 2009), or if a flare is exactly a result of a small and localized (quite possibly unobservable) perturbation affecting the whole system like self-organized criticality dynamics (Bak et al. 1987; Bélanger et al. 2007), then it is not feasible to carry out prediction of flare onset time and magnitude by using present-day parameters derived from photospheric magnetic field observations. More specifically, helicity accumulation might be a necessary, but not sufficient condition for flares. Perhaps a triggering mechanism is necessary even a magnetic system has enough non-potentiality to power a flare (so-called metastable state). This idea agrees with the study that a number of X-class flares occurred during the phase of almost constant helicity after the phase of 2–3 days of monotonically increasing helicity (Park et al. 2008).

Interestingly, contrary to the expectation that magnetic helicity injection is more closely related to flare productivity than to magnetic flux, the result of this study shows that the correlation between $|<\dot{H}_r>|$ and F_{idx} is not stronger than that between $<\Phi>$ and F_{idx}. The logarithmic-scale CCs of F_{idx} versus $|<\dot{H}_r>|$ and $<\Phi>$ are 0.42 and 0.43, respectively. If only the flaring groups with non-zero flare index are considered, then $|<\dot{H}_r>|$ is not better than $<\Phi>$ in predicting how strong the flares will be. This might be due to the fact that the 1 day average of $\dot{H}_r$ in the entire active region is simply used for comparison with F_{idx} without more specifically characterizing the temporal and spatial evolution of helicity in the active region related to a flaring condition. Magnetic helicity, however, is

useful in predicting whether an active region will produce flares or not. Note that predicting the occurrence of flares is different from predicting the strength of flares. By examining more careful studies such as the helicity injection difference between flare-productive and flare-quiet active regions, the flare-productive probability as a function of $|<\dot{H}>|$, and the temporal evolution of helicity in major flare-producing active regions, it has been found that magnetic helicity injection has some interesting features related to flares as follows.

1. For 91 active region samples in the range (3–5)$\times 10^{22}$ Mx of large $<\Phi>$ the *flaring* group has $|<\dot{H}_r>|$ about twice greater than that of the *non-flaring* group. On the other hand, 118 active region samples of large $|<\dot{H}_r>|$ do not show the significant difference in $<\Phi>$ between the *flaring* and *non-flaring* groups.

2. The helicity parameter $|<\dot{H}_r>|$ demonstrates a rapid increase of P_i compared to that of $<\Phi>$ in the rescaled range of 0–0.15 of the parameter. $P_C(|<\dot{H}_r>|)$, especially, quickly reaches up to $\sim$90% from 46% in the very low rescaled range, 0–0.15, of the parameter, and it retains a high value above 90% in the rest, 0.15–0.6, of the statistically meaningful range.

3. Helicity of (3–45)$\times 10^{42}$ Mx^2 accumulates significantly and consistently over 0.5–2 days for all the 19 major flares under investigation supporting the major finding of Chapter 3. More specifically, following the significant amount of long-term helicity accumulation with fast injection rate, 4 and 8 flares occurred when helicity injection rate starts to become slow (sometimes almost zero) and reverse its sign, respectively.

Based on these results, the magnetic helicity can be used for the improvement of flare forecasting. First of all, when an active region has large $<\Phi>$, it might be better de-

termined whether or not it will produce a flare by considering $|<\dot{H}_r>|$ of the active region. Second, the helicity parameter $|<\dot{H}_r>|$ would allow to establish a better defined cutoff between C-flare-productive and C-flare-quiet active regions than $<\Phi>$ if a sharp increase of P_i in the very low rescaled range of the parameter is taken into account. Third, an early warning sign of flare occurrence could be based on tracking of a phase of monotonically increasing helicity because there is always a significant amount of helicity accumulation a few days before major flares. An urgent warning sign might be also made when helicity injection rate becomes very slow or the opposite sign of helicity starts to be injected after the significant helicity accumulation phase. The sign reversal of the magnetic helicity may support the numerical simulation model for solar flare onset proposed by Kusano et al. (2003b) in which they showed that magnetic reconnection quickly grows in the site of the helicity annihilation with different signs. Some observations of helicity inversion, similar to this result, were also reported around the time of flare onset (Kusano et al. 2003a; Yokoyama et al. 2003; Wang et al. 2004b). For more practical and advanced flare forecasting, there should be studies on how to consider the past history of flare occurrence in an active region under investigation and combine the helicity parameter with others with different weighting coefficients. Besides that it would be required to better characterize not only the time history of helicity injection but also its spatial distribution inside active regions.

Finally, this study may lead to some physical understanding of flare on-set. For example, why do only some of the samples with the large helicity injection produce major flares, but not for all? Is a significant amount of helicity accumulation necessary or sufficient conditions for flares? The study of magnetic helicity in a coronal volume of an active region will help to better explain physically for these questions and understand pre-flare

conditions and energy storage process of flares in more detail. To explore this idea further, the study of the coronal helicity by using three-dimensional nonlinear force-free magnetic field extrapolations will be discussed in the following Chapter 5.

CHAPTER 5

TIME EVOLUTION OF CORONAL MAGNETIC HELICITY IN THE FLARING ACTIVE REGION NOAA 10930

In this chapter[1], taking the advantage of unprecedented observations and coronal magnetic field modeling tools, the coronal relative magnetic helicity in the flaring active region NOAA 10930 is investigated during the time period of December 8–14 to study the three-dimensional (3D) magnetic field topology and its long-term evolution associated with the X3.4 flare of 2006 December 13. The coronal helicity is calculated based on the 3D nonlinear force-free (NLFF) magnetic fields reconstructed by the weighted optimization method of Wiegelmann (2004), and is compared with the amount of helicity injected through the photospheric surface of the active region. The helicity injection is determined from the magnetic helicity flux density proposed by Pariat et al. (2005) using *SOHO*/MDI magnetograms. The major findings of this study are: (1) the time profile of the coronal helicity shows a good correlation with that of the helicity accumulation by the injection through the surface; (2) the coronal helicity of the AR is estimated to be -4.3$\times 10^{43}$ Mx^2 just before the X3.4 flare; (3) this flare is preceded by not only a large increase of negative helicity, -3.2$\times 10^{43}$ Mx^2, in the corona over $\sim$1.5 days but also noticeable injections of positive helicity though the photospheric surface around the flaring magnetic polarity inversion line during the time period of the channel structure development. It is conjectured that the occurrence of the X3.4 flare is involved with the positive helicity injection into an existing

[1]This chapter is based on the following paper:
Park, S.-H., Chae, J., Jing, J., Tan, C., & Wang, H. 2010, Astrophys. J., in press.

system of negative helicity.

5.1 Introduction

The photospheric magnetic fields in the active region NOAA 10930 have been observed comprehensively by the MDI (Scherrer et al. 1995) aboard the *SOHO* spacecraft and the SOT (Tsuneta et al. 2008) onboard the *Hinode* satellite. In recent years, following the observations, considerable attention has been paid to investigate the structure of magnetic field lines and its evolution in AR 10930 related to the occurrence of the X3.4 flare on 2006 December 13. There were studies of sunspot rotation associated with the flare such as remarkable counterclockwise rotation of the positive polarity sunspot Yan et al. (2009), interaction between the fast rotating positive sunspot and ephemeral regions near the sunspot (Zhang et al. 2007), and non-potential magnetic stress (Su et al. 2008). AR 10930 was also investigated for a change of magnetic field lines at the flaring site before and after the flare, e.g., azimuth angle (Kubo et al. 2007). Moreover, time variations of magnetic helicity injection rate (Zhang et al. 2008; Magara & Tsuneta 2008) and intermittency (Abramenko et al. 2008) were examined over a time span of several days around the time of the flare.

To resolve limitations of using photospheric magnetic field data, some studies have been carried out on the X3.4 flare with the 3D coronal magnetic fields derived from NLFF extrapolation methods. Jing et al. (2008) reported that magnetic shear around the flaring magnetic polarity inversion line decreased after the flare at coronal heights in the range 8–70 Mm. By calculating the 3D electric current in AR 10930, Schrijver et al. (2008) showed that there are long fibrils of strong current slightly above the photosphere that almost completely disappear after the flare. Later on, Wang et al. (2008) found that the strong

current-carrying fibrils are associated with magnetic channel structure of AR 10930 and the flare occurred during the period that the channels were rapidly developed. In addition, the free energy of the NLFF fields were studied to understand energy build-up, storage and release processes in the corona for the flare. The free energy release of 2.4×10^{31} ergs during the flare was measured by Guo et al. (2008), and Jing et al. (2010) found that a significant amount of free energy is continuously built up during the 2 days prior to the flare.

Encouraged by interesting results of the previous studies with NLFF fields, in this study, the variation of the coronal relative magnetic helicity in AR 10930 is investigated over a span of several days to find its relationship with the flare. Magnetic helicty is a measure of how much magnetic field lines in a flux tube are twisted around the tube axis, how much the tube axis is kinked, and how much flux tubes are interlinked each other in a magnetic field system. It has been studied to understand an energy build-up process and a trigger mechanism for flare occurrence. It is expected that coronal magnetic helicity study will bring a better understanding of the long-term evolution of the large-scale magnetic field non-potentiality in the corona related to the X3.4 flare despite of a critical assessment (e.g., De Rosa et al. 2009) in NLFF extrapolation that existing NLFF extrapolation models are not able to accurately reproduce coronal fields and physical quantities of interest in the active-region corona due to some problematic issues such as the non-force-free nature of the photospheric magnetic field, the limited FOV and the noise level of vector magnetograms, etc. The coronal helicity will also be compared with the helicity injection through the photospheric surface to check their relationship and consistency.

5.2 Data Processing and Helicity Calculation

For the calculation of H_r in a 3D coronal volume, it is required to obtain the three components of the magnetic field in that coronal volume. Therefore, the coronal NLFF fields in AR 10930 is derived from the Stokes profiles taken by *Hinode*/SOT SP following the same way described in Jing et al. (2010). The high-resolution vector magnetic fields in the photosphere were first derived from the Stokes profiles using an Unno-Rachkovsky inversion based on the Miler-Eddington atmosphere (e.g., Lites & Skumanich 1990; Klimchuk et al. 1992); Klimchuk et al. 1992). In addition, the removal of the 180° ambiguity in the transverse magnetic fields was accomplished using the minimum energy algorithm (Metcalf et al. 2006), and the photospheric vector magnetograms were projected onto the tangent plane at the heliographic location of the center of the magnetograms. To reduce the inaccuracy of NLFF field extrapolation, it is important to derive suitable boundary fields for the NLFF field modelling from the photospheric magnetograms. Therefore, using a preprocessing method developed by Wiegelmann et al. (2006), the effect of the Lorentz force acting in the photosphere was minimized so that the NLFF boundary fields are prepared to be in the condition of the low plasma-β force-free chromosphere. Finally, the weighted optimization method (Wiegelmann 2004) was used to extrapolate the NLFF coronal fields from the photospheric magnetograms. This method has been well recognized as an outstanding performance algorithm by some model tests of NLFF fields (e.g., Schrijver et al. 2006; Metcalf et al. 2006). Refer to Figure 5.1 to see an example of 3D coronal magnetic fields extrapolated from the *Hinode*/SOT SP vector magnetogram (gray image) at 20:30 UT on 2006 December 12.

AR 10930 appeared on the east limb of the solar disk on 2006 December 6, and was

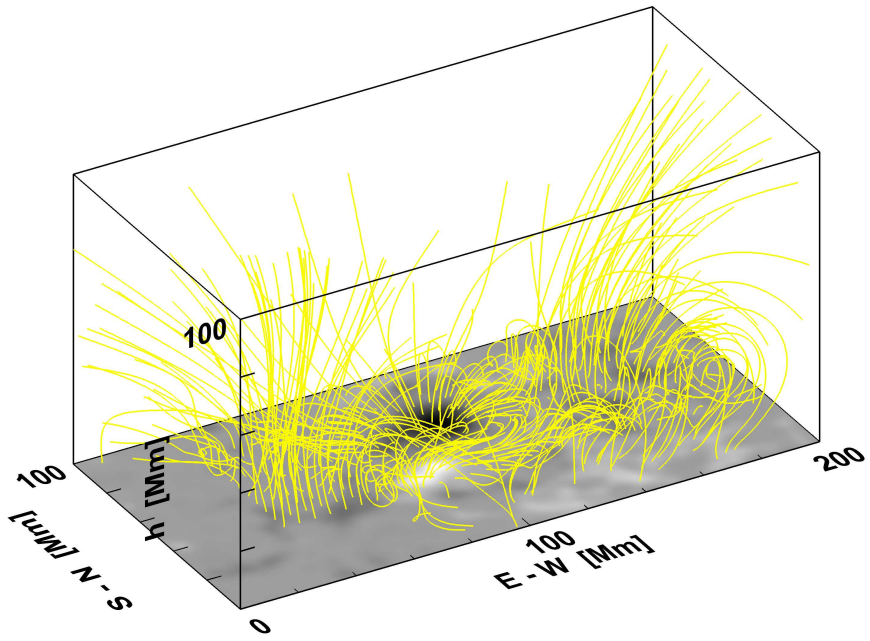

Figure 5.1 Extrapolated NLFF field of AR 10930 at 20:30 UT on 2006 December 12. The grayscale image is the normal component of the photospheric magnetic field which was taken by the *Hinode*/SOT SP and used for the extrapolation.

successfully and continuously observed during the time interval of its entire disk passage by *Hinode*/SOT and *SOHO*/MDI. In this study, H_r in AR 10930 is determined from Equations 2.1 through 2.4 described in Section 2.1 during the time span of 2006 December 8, 21:20 UT through 2006 December 14, 5:00 UT. 27 *Hinode*/SOT-SP vector magnetograms are used as the boundary fields for NLFF field extrapolation. The computational dimensions of the 3D NLFF field data were considered as $240\times132\times180$ pixel^3 corresponding to $288\times158\times216$ Mm^3. To check the influence of the preprocessing on the magnetogram data, L_1 and L_2 of the original data and those of the preprocessed data were calculated, which are associated with the force-balance condition and the torque-free condition, respectively. They were proposed by Wiegelmann et al. (2006) to investigate how well a photospheric magnetic field agrees with Aly's criteria. Refer to Wiegelmann et al. (2006) for the details of the preprocessing method and the definitions of L_1 and L_2. As shown in Table 5.1, the preprocessed data satisfy the Aly criteria much better than the original data. It has been reported that this preprocessing procedure significantly improves the boundary fields towards a force-free condition (e.g., see Wiegelmann et al. 2006, 2008). Recently, Jing et al. (2010) also showed the capability of the preprocessing method by comparing the unpreprocessed/preprocessed photospheric line of sight (LOS) magnetogram of AR 10930 with the co-aligned chromospheric LOS magnetogram. To evaluate the performance of the NLFF extrapolation, the current-weighted sine metric (CWsin) and $<|f_i|>$ metric proposed by Wheatland et al. (2000) were also calculated for each extrapolated field. CWsin and $<|f_i|>$ measure the degree of convergence to a force-free and divergence-free field, respectively. For the 27 NLFF fields under investigation, the average CWsin was estimated as $\sim$0.39 and the average $<|f_i|>$ as $\sim$0.0014 indicating that residual forces and divergences

exist in the NLFF fields.

In addition, the error estimation of H_r is carried out with a Monte Carlo method by only taking into account the sensitivity of the SP measurement as follows (e.g., see Guo et al. 2008): first, 3 sets of artificial noises are added to B_x, B_y, and B_z of the original SP vector magnetogram at 20:30 UT on 2006 December 12. Each noise set consists of pseudo-random numbers in normal distribution with the standard deviation of 5 G for B_z and 50 G for B_x and B_y. Note that these values of 5 G and 50 G are estimated as the maximum values of the SP sensitivity in the line-of-sight direction and the transverse direction, respectively (Tsuneta et al. 2008). Then, the 3D NLFF fields are extrapolated from the noise-imposed vector magnetogram following the procedure described in the above paragraph, calculate H_r, and repeat the same process 10 times. Finally, the standard deviation of 10 sets of H_r is considered as the uncertainty of the H_r calculation. The uncertainty was found as 8×10^{41} Mx^2 corresponding to 2–4% of $|H_r|$ during the measurement period.

In order to calculate $\dot{H}_r$, the data set consisting of 63 full-disk MDI magnetograms at the 96 min cadence was used in the time span of 2006 December 8, 20:51 UT through 2006 December 13, 16:03 UT. Note that the MDI magnetograms in the data set show the Zeeman saturation in the central part of the negative sunspot umbral region so that the

Table 5.1 Comparison of the Average L-values for the Original Data and Preprocessed Data of *Hinode*/SOT-SP Vector Magnetograms

	Original	Preprocessed
L_1[a](G^4)	1.12×10^{19}	9.56×10^{12}
L_2[b](G^4 Mm^2)	2.02×10^{23}	1.08×10^{19}

[a] $L_1=\left[\left(\Sigma B_x B_z\right)^2+\left(\Sigma B_y B_z\right)^2+\left(\Sigma B_z^2-B_x^2-B_y^2\right)^2\right]$

[b] $L_2=\left[\left(\Sigma x(B_z^2-B_x^2-B_y^2)\right)^2+\left(\Sigma y(B_z^2-B_x^2-B_y^2)\right)^2+\left(\Sigma y B_x B_z-xB_y B_z\right)^2\right]$

calculation of $\dot{H}_r$ might be underestimated. The window function of DAVE used in the $\dot{H}_r$ calculation is the top-hat profile which puts the same weight of unity to every pixel inside the window (e.g., Schuck 2006) and the window size is selected as 10 arcseconds. DAVE was also applied to two MDI images with the spatial derivatives being calculated from the average of the two images (e.g., Welsch et al. 2007; Chae 2007; Chae & Sakurai 2008). The uncertainty of $\dot{H}_r$ corresponding to measurement uncertainty ($\sim$20 G) of MDI magnetograms was also estimated using the same Monte Carlo method used in the error estimation of H_r. It is found that the uncertainty of $\dot{H}_r$ is 8.4×10^{39} Mx^2/hr which is equivalent to $\sim$3% of the average $\dot{H}_r$ during the measurement time. The uncertainty therefore does not significantly affect the calculation of $\dot{H}_r$ and ΔH_r.

5.3 Results and Discussion

The main objective in this study is to examine how well H_r and ΔH_r are correlated with each other and whether the H_r calculation using the NLFF coronal fields is verified by the comparison of H_r derived from *Hinode*/SOT-SP data with ΔH_r derived from *SOHO*/MDI data. In Figure 5.2, therefore, the temporal variations of H_r (black solid line) and ΔH_r (gray solid line) are plotted. The estimated error of H_r is marked with error bars. The initial value of ΔH_r is set as same as that of H_r. $|H_r|$, the absolute value of H_r, is also shown as dotted line for convenience. The day-to-day variations of H_r in AR 10930 is also investigated for a better understanding of pre-flare conditions and a trigger mechanism of the X3.4 flare. For this, H_r (black solid line) is plotted with the total unsigned magnetic flux (dashed line) and the *GOES* soft X-ray light curve (dotted line) in Figure 5.3. Note that Lim et al. (2007) have done a similar study in which they compared coronal helicity

in AR 10696 with helicity injection through the photosphere. In their study, the coronal helicity was estimated as a probable range using a linear force-free (LFF) assumption with a force-free constant which gives the best fit with each of individual coronal loops, even though the real coronal field is not LFF. The photospheric helicity injection was calculated by inferring the velocity of the apparent horizontal motion of field lines determined by the LCT technique, as originally proposed by Chae (2001), instead of using $\boldsymbol{u}$ determined by the DAVE technique. They found that the temporal variation of the coronal helicity is similar to that of the photospheric helicity injection with a discrepancy of $\sim$15%.

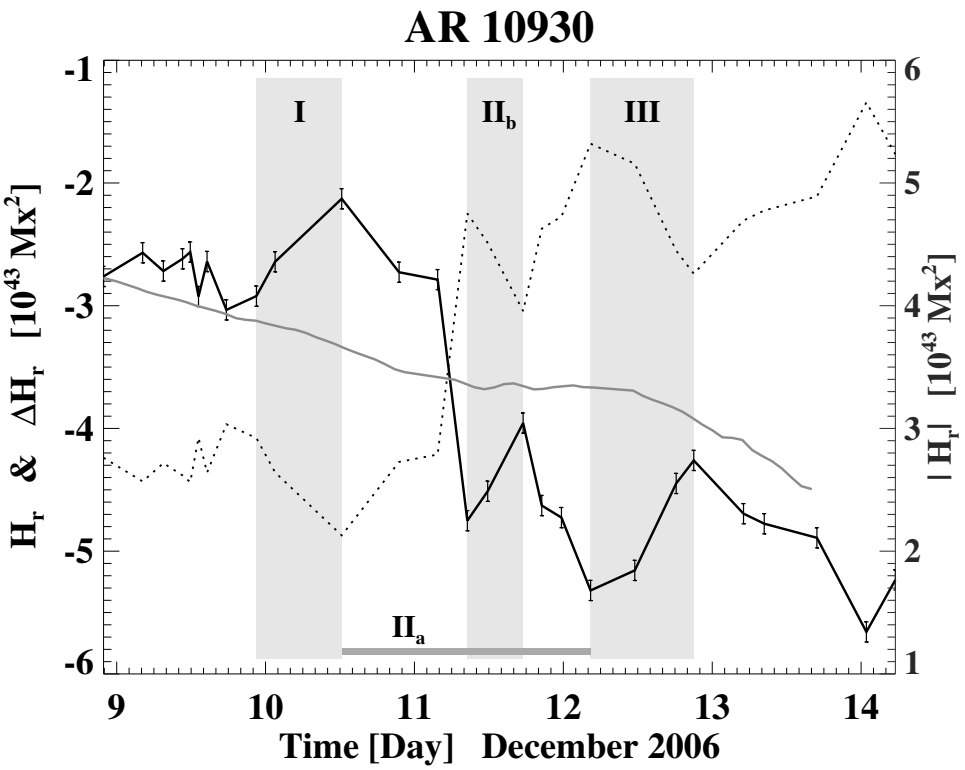

Figure 5.2 Time variations of the coronal relative magnetic helicity H_r (black solid line with error bars) and the helicity accumulation ΔH_r (gray solid line). The absolute value of H_r decreases for more than 9 hours in the periods marked as I, II$_b$, and III while it shows a significant increase of 3.2×10^{43} Mx^2 during the period of II$_a$. In general, the time profile of H_r shows a good correlation with that of ΔH_r during the entire measurement period.

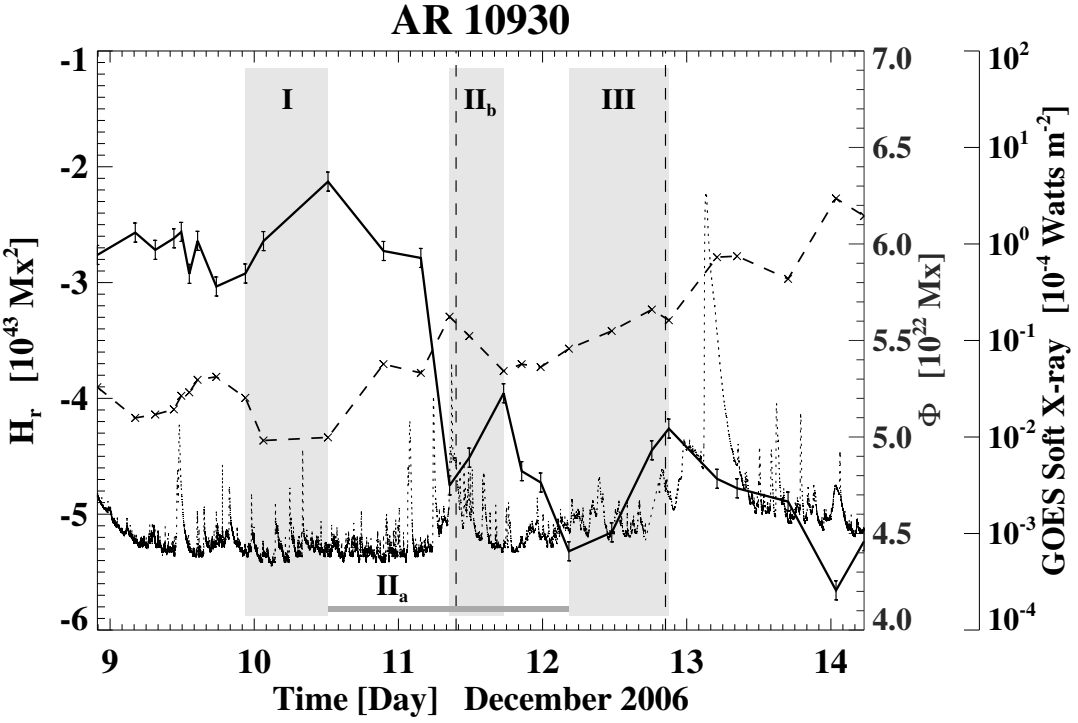

Figure 5.3 The coronal relative magnetic helicity H_r (black solid line with error bars) and the unsigned magnetic flux Φ (dashed line) of AR 10930 are plotted with and *GOES* soft X-ray flux (dotted line) during the time period of December 8, 21:20 UT through December 14, 5:00 UT. The X3.4 flare occurred in AR 10930 and peaked at 2:40 UT on 2006 December 13. During the periods of II$_b$ and III, there were two CMEs inferred to be originated from AR 10930, and their first appearance times in the LASCO/C2 FOV are marked with the black vertical dashed lines. The characteristic periods of I, II$_a$, II$_b$, and III are marked in the same way as in Figure 5.2.

During the first day of the helicity measurement, H_r showed little change from its initial value, -2.8×10^{43} Mx^2, though there were small fluctuations in the range of 2–15%. Then, $|H_r|$ decreased by 28% from 2.9×10^{43} Mx^2 to 2.1×10^{43} Mx^2 for 14 hours from December 10. Note that the decrease of $|H_r|$ could be due to: (1) a pre-existing negative helicity is expelled from the volume of the NLFF field extrapolation, e.g., via coronal mass ejections (CMEs), and/or (2) a new magnetic flux with positive helicity is injected from outside into the volume or positive helicity is produced by shearing motions of pre-existing field lines. It was found that there are three time periods (I, II$_b$, and III) over which $|H_r|$ decreases consistently for more than 9 hours, and they are shown as the shaded areas. Between periods I and III, there was a consistently large increase of negative helicity, -3.2×10^{43} Mx^2, in the corona over $\sim$1.5 days (marked as period II$_a$ in Figure 5.2). After period III, a negative helicity kept on increasing for $\sim$1 day with flux increase. The detailed information of the characteristic periods is shown in Table 5.2.

The overall pattern of the temporal evolution of H_r calculated using the NLFF fields is compared with that of ΔH_r measured using the MDI magnetograms. In general, the time profile of H_r well matches that of ΔH_r. Moreover, in both cases, the absolute amount of negative helicity accumulation during the entire measurement period of December 9–14 was similar (2.1×10^{43} Mx^2 and 1.7×10^{43} Mx^2, respectively). This gives us confidence that

Table 5.2 Characteristic Periods of the Temporal Variation of the Coronal Helicity

Periods	Duration (hr)	Initial/Final $\lvert H_r\rvert$ (10^{43} Mx^2)	$\lvert H_r\rvert$ Change (%)	Initial/Final Flux (10^{22} Mx)	Flux Change (%)
I	13.8	2.9 / 2.1	-28	5.2 / 5.0	-4
II$_a$	40.1	2.1 / 5.3	152	5.0 / 5.5	10
II$_b$	9.0	4.8 / 4.0	-17	5.6 / 5.3	-5
III	16.6	5.3 / 4.3	-19	5.5 / 5.6	2

the NLFF extrapolation and the H_r calculation are reasonably well established. However, some detailed patterns of helicity evolution show a difference between H_r and ΔH_r. For example, the temporal variation of H_r shows a rapid and large increase of negative helicity with flux increase at the time period of the fast rotational speed in the southern positive sunspot measured by Min & Chae (2009) and Yan et al. (2009). In addition, $|H_r|$ represents decreasing phases such as periods I, II_b, and III, while $|\Delta H_r|$ increases monotonically during the entire period. Note that H_r should not necessarily be exactly the same as ΔH_r: e.g., the ejection of magnetic helicity via the launch of a CME would not be detected in ΔH_r while it would be reflected in H_r.

What could cause the three periods of the remarkable $|H_r|$ decrease? To inquire this, a possibility associated with the negative helicity ejection via CMEs originated from AR 10930 was first checked. The *SOHO*/LASCO CME catalog (Yashiro et al. 2004) was used for searching all the CMEs occurred during the periods. Then, only the CMEs inferred to be produced in AR 10930 was identified with the following criterion: the position angle of a CME should be within ± 5 degrees from that of AR 10930 on the solar disk at the first appearance time of the CME in the LASCO/C2 FOV. Note that there was no AR except AR 10930 on the front side of the solar disk during the periods. Two CMEs were found, and they are shown in Figure 5.4: one in period II_b and the other in period III. Their initial appearances in the LASCO/C2 FOV were at 09:36 UT on December 11 and at 20:28 UT on December 12, respectively, which are marked with the vertical dashed lines in Figure 5.3. Although the uncertainty of the H_r calculation is estimated as 8×10^{41} Mx^2, it was found that the decrease in $|H_r|$ is 2.4×10^{42} Mx^2 between 08:31 UT and 11:48 UT on December 11 and 1.9×10^{42} Mx^2 between 18:12 UT and 21:01 UT on December 12 covering the time

of the occurrence of the first CME and that of the second CME, respectively. These values agree with the helicity content of a typical CME, 2×10^{42} Mx^2, estimated by DeVore (2000). This finding of the CME-related change of $|H_r|$ is similar to the earlier one by Lim et al. (2007) in which they found a helicity decrease of $\sim4.1\times10^{42}$ Mx^2 after the occurrence of two CMEs.

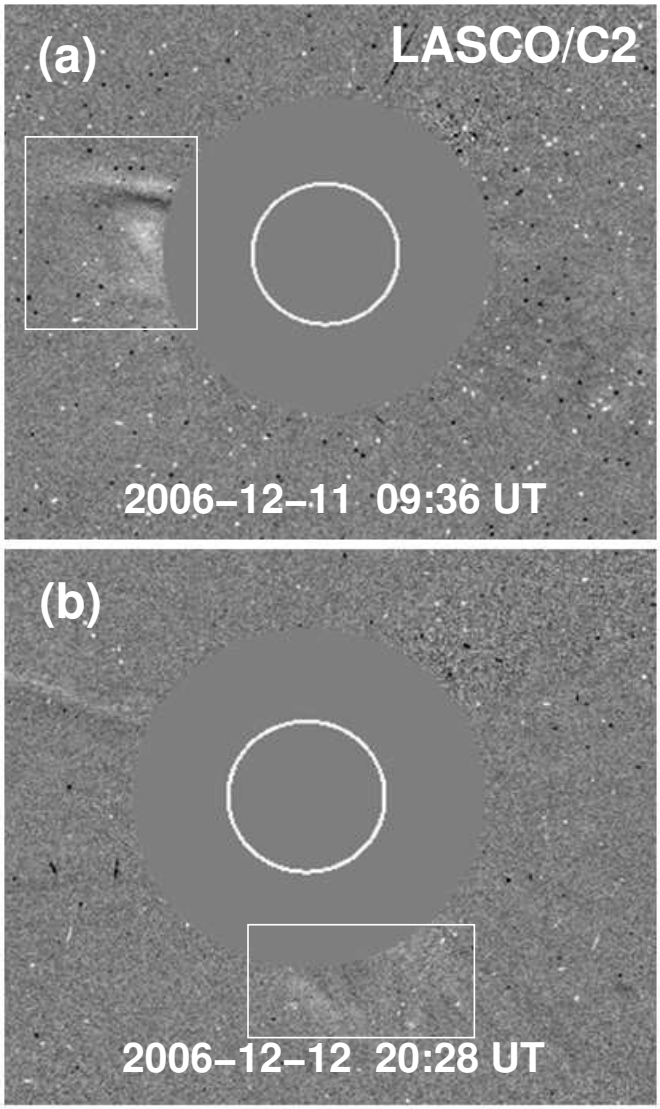

Figure 5.4 LASCO/C2 images. Two CMEs inferred to be originated from AR 10930 appeared at (a) 09:36 UT December 11, 2006 and (b) 20:28 UT December 12, 2006. They are marked in a rectangle in each panel.

The feasibility of positive helicity injection through the photospheric surface of AR 10930 into the corona was also investigated. Note that Zhang et al. (2008) have calculated $\dot{H}_r$ in AR 10930 using the LCT method (Chae 2001). They found the sign of $\dot{H}_r$ changes from negative to positive and then from positive to negative during the period (01:30 UT–04:30 UT) of the flare, while $\dot{H}_r$ is predominantly negative during 2006 December 8–14. Integrating the positive (negative) G_θ over the photospheric surface of AR 10930, $\dot{H}_r^+$ ($\dot{H}_r^-$), i.e., the injection rate of positive (negative) helicity, was determined. Figure 5.5 shows the time variations of $\dot{H}_r^+$ (diamonds), $\dot{H}_r^-$ (crosses), and $\dot{H}_r$ (solid line) during the ΔH_r measurement period. The characteristic periods are marked in the same way as in Figure 5.2, and the peak time of the X3.4 flare is shown as the vertical dotted line. It was found that a remarkable accumulation of positive helicity into the corona is established over the entire period with the average injection rate of 2.8×10^{41} Mx^2/hr, even though for the most time $\dot{H}_r^-$ is dominant with the average injection rate of -4.4×10^{41} Mx^2/hr. Especially, during the span of December 11, 12:51 UT (middle of period II$_b$) through December 12, 04:48 UT (start of period III), the average of $\dot{H}_r^+$ showed a large value of 4.5×10^{41} Mx^2/hr, and $\dot{H}_r^+$ was sometimes larger than $\dot{H}_r^-$. Additionally, the G_θ maps at several times marked with the vertical solid lines in Figure 5.5 were examined to find out how the positive G_θ is distributed and developed on the AR. Figure 5.6 shows the maps of the normal component of magnetic field, B_n, (left panels) and G_θ (right panels). Assuming that the magnetic field on the solar photosphere is normal to the solar surface, B_n was approximately determined from the MDI line-of-sight magnetograms. It was found that there are noticeable injections of positive helicity around the flaring magnetic polarity inversion line (see the three G_θ maps in Figure 4: 2006-12-11 12:51 UT, 2006-12-12 04:48 UT, and 2006-12-12 23:59

UT). In addition, the examination of the other G_θ maps during the period of December 11, 12:00 UT through December 13, 16:00 UT revealed that positive helicity is consistently injected through the polarity inversion line. The location and time span of the positive helicity injection are similar to those of the magnetic channel structure development observed by Wang et al. (2008). Note that a simulation by Régnier (2009) shows that newly injected currents from the photosphere can sensitively affect the coronal magnetic helicity in existing force-free bipolar fields: i.e., H_r is increased by 2 orders of magnitude when the current strength is increased by a factor of 2. It is therefore speculated that periods II_b and III are associated with the helicity ejection via the two CMEs and/or the supply of positive helicity from the photosphere into the corona.

Related to the occurrence of the X3.4 flare, two interesting phases of the long-term H_r evolution were found. First, there was a significant increase of negative H_r for period II_a of $\sim$1.5 days associated with the flare energy buildup. This helicity increasing phase prior to the flare is in agreement with that shown in the study of Park et al. (2008, 2010). After the middle of period II_a, a large amount of helicity of the opposite (positive) sign started to be injected through the photospheric surface around the flaring magnetic polarity inversion line during the time span (including periods II_b and III) of the channel structure development observed by Wang et al. (2008). The X3.4 flare was preceded by the two characteristic phases of H_r. These two phases have been already reported by the previous studies of major flares related to helicity injection through photospheric surfaces of ARs (Park et al. 2008, 2010; Chandra et al. 2010). Note that the finding of the long-term injection of positive helicity during $\sim$2.5 days before the flare is different from the abrupt injection of positive helicity around the start of the flare found by Zhang et al. (2008).

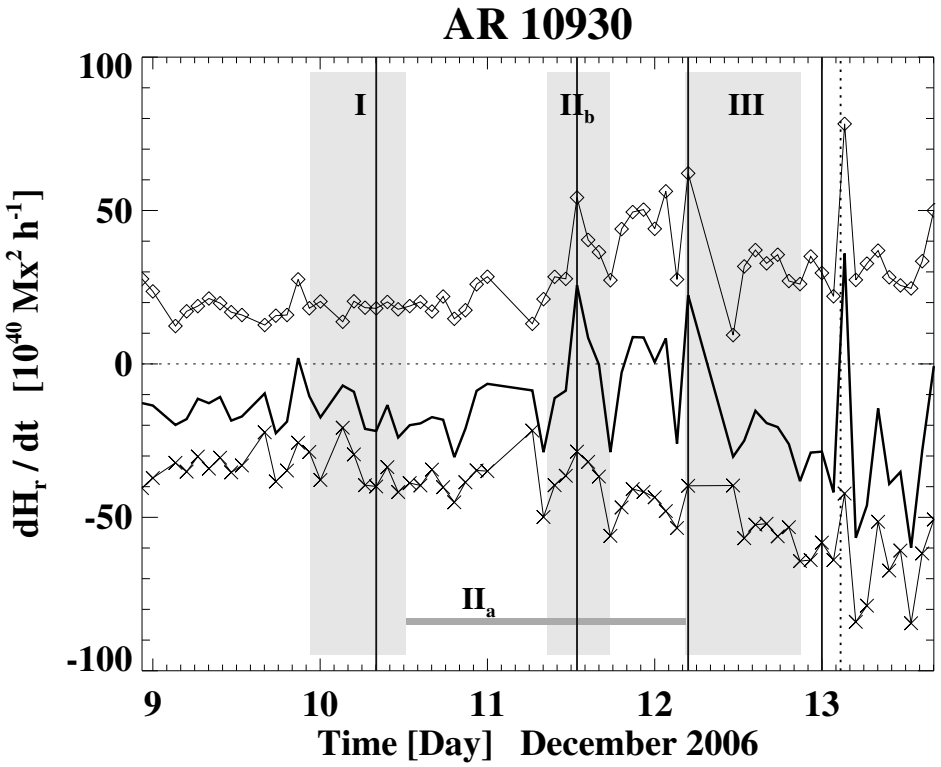

Figure 5.5 Injection rates of positive helicity (diamonds), negative helicity (corsses), and total helicity (solid line) during the time span of December 8, 20:51 UT–December 13, 16:03 UT. The characteristic periods of I, II$_a$, II$_b$, and III are marked in the same way as in Figure 5.2, and the peak time of the X3.4 flare is shown as the vertical dotted line. The vertical solid lines indicate the times for the investigation of the helicity flux density maps in Figure 5.5.

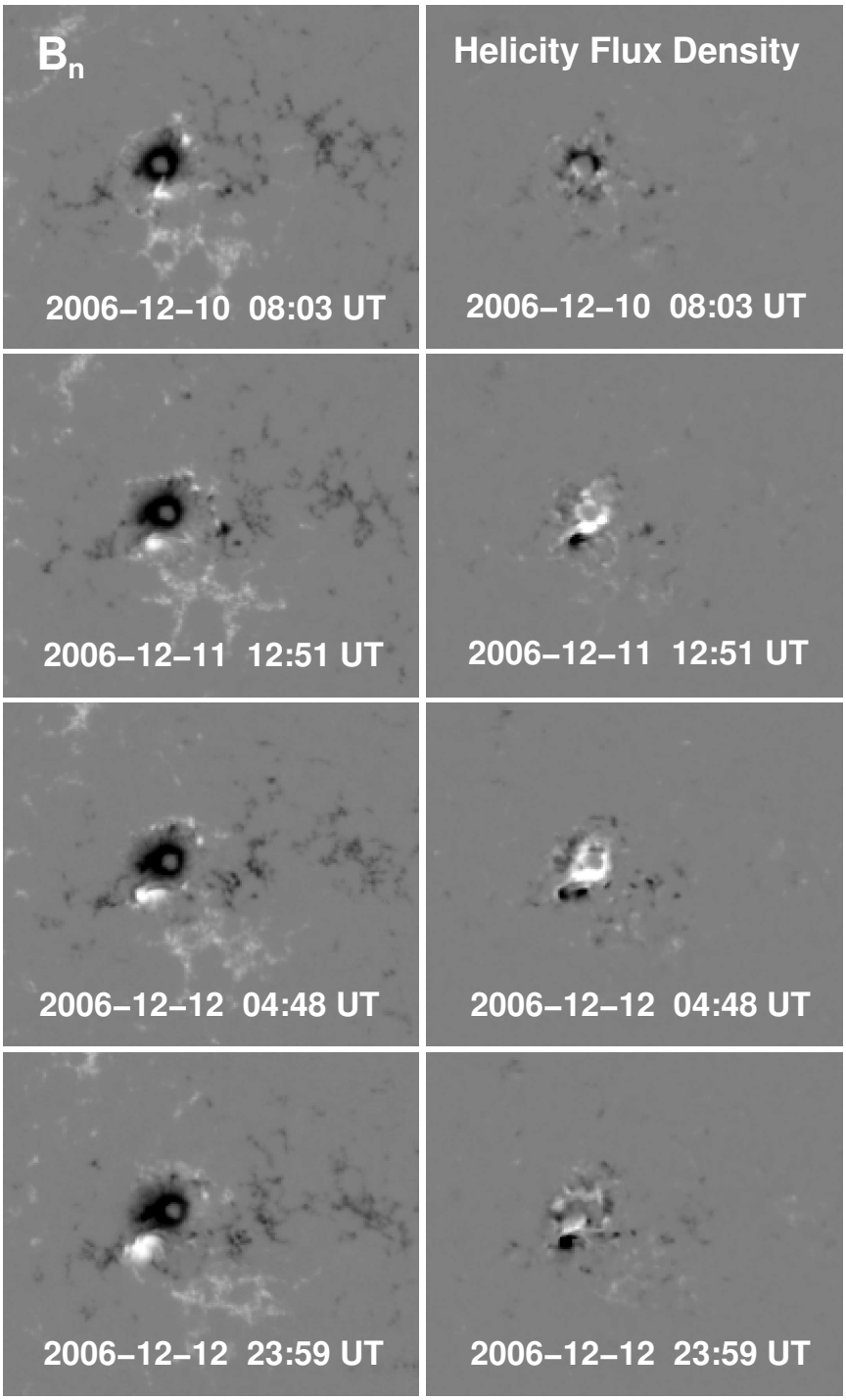

Figure 5.6 Temporal evolution of the photospheric magnetic field and of helicity injection rate in AR 10930. Left panels: the normal component of the magnetic field, B_n, derived from the MDI line-of-sight magnetograms. Right panels: helicity flux density, G_θ. Note that the median of $|G_\theta|$ is $\sim 2\times10^3$ G^2 km/s Mm, and the saturation level of $|G_\theta|$ as 2.5×10^6 G^2 km/s Mm is set for purpose of display visibility. After 12:00 UT of December 11, a large amount of positive helicity started to be injected around the flaring magnetic polarity inversion line.

It is conjectured that the occurrence of the X3.4 flare is involved with the emergence of a positive helicity system into an existing negative helicity system which may cause a reconnection between the two helicity systems. This idea is not only supported by the numerical simulation (Kusano et al. 2003b) in which magnetic reconnection quickly grows in the site of the helicity annihilation with different signs but also the observational reports for the opposite sign of helicity injection through the photosphere surface of ARs before flares (Kusano et al. 2003a; Yokoyama et al. 2003; Wang et al. 2004b).

Another interesting finding is that the temporal variation of H_r follows a similar pattern to that of the rotational speed in the southern positive sunspot. The rotational speed is referred from the study of Yan et al. (2009) in which they calculated the rotational speed from *Hinode*/SOT SP continuum intensity images. It is understandable that the counter-clockwise rotation of the positive sunspot could twist the field lines to have left-handed (negative) helicity so that the faster the southern sunspot rotates, the larger negative helicity the rotation can generate into the corona. However, instead of the sunspot rotation, the negative helicity increase might be related to the emergence of a pre-twisted flux tube because the time profile of unsigned flux is also similar to that of H_r. Note that Schrijver et al. (2008), in their NLFF field study for AR 10930, also argued that strong electric currents emerge together with magnetic flux. If so, the sunspot rotation is not the cause of helicity supply but the manifestation of the twisted flux emergence: sunspot rotation can be regarded as the simple advection of a twisted flux tube or it can be driven by the torque due to the rapid stretching of twisted field lines emerging into the corona (Longcope & Welsch 2000; Chae et al. 2003; Min & Chae 2009). In addition, the temporal variation of $|H_r|$ shows a rapid and large increase of negative helicity with flux increase at the time period

of the magnetic channel structure appearance (3:00–8:00 UT on December 11) studied by Wang et al. (2008). Note that there was a C5.7 class flare right after the rapid negative helicity injection. If the channel structure is related to the emergence of pre-twisted flux tube, then Chae's method for calculating $\dot{H}_r$ may not work effectively for the case of helicity injection due to newly emerging pre-twisted flux.

In conclusion, after analyzing H_r in the coronal volume of AR 10930 using the NLFF fields, it was found that there are two characteristic phases of day-to-day variation of helicity related to the X3.4 flare: significant helicity accumulation (period II_a) followed by opposite sign helicity injection (periods II_b and III). H_r and ΔH_r show a roughly similar variation during the entire measurement period. Further studies are needed to check whether the two characteristic phases are shown in other major flaring ARs and to investigate a short-term variation of helicity in a flaring region related to a triggering mechanism.

CHAPTER 6

MAGNETIC HELICITY INJECTION RELATED TO THE CME INITIATION AND SPEED

In this chapter, magnetic helicity injection in CME-productive active regions is investigated to find its relationships with (1) the gradual inflation of active-region coronal arcades and (2) the occurrence and speed of CMEs. Using the wavelet-enhanced EIT observations combined with the LASCO, MDI, and *GOES* soft X-ray observations, it is studied how helicity injection of $\sim$1 day from the photosphere of an active region is associated with the slow rising phase of a coronal arcade building up to a CME. Day-to-day variation of helicity is also investigated for 28 active regions producing 46 CMEs. The major findings of this study are as follows. First, the inflation stage of the coronal arcades sustains for hours at a speed of less than 5 km s^{-1}, and it is temporally associated with helicity injection from the active-region photosphere. Second, the 46 CMEs are categorized into two different groups by two characteristic evolution patterns of helicity injection in their active regions: (1) a monotonically increasing of helicity accumulation (*Group A*; 30 CMEs in 23 active regions) and (2) significant helicity injection followed by its sign reversal (*Group B*; 16 CMEs in 5 active regions). Finally, a fairly good correlation (CC=0.71) between the helicity injection rate and the CME speed is found for the 30 CME events in *Group A*.

6.1 Introduction

There have been many studies to better understand a trigger mechanism of CMEs with several numerical simulation models. Chen & Shibata (2000) showed in their simulation

that a CME can be triggered by the localized reconnection between a pre-existing coronal field and a reconnection-favorable emerging flux with observational supports (Feynman & Martin 1995; Wang et al. 2004b; Jing et al. 2004). A flux cancelation model (van Ballegooijen & Martens 1989; Linker et al. 2001), in agreement with observations (Martin 1994; Gaizauskas et al. 1997; Martin 1998), suggested that the converging motion of magnetic arcades, by which a filament may be formed, can lead to the destabilization of the filament followed by a CME. Antiochos et al. (1999) proposed a model (so-called breakout model) in which the reconnection of the overlying background magnetic field with the sheared arcade at the magnetic null point above the latter gradually remove the constraint over the sheared arcade so that a CME can occur. A kink instability by the emergence of twisted flux tube (Hood & Priest 1981; Fan & Gibson 2004; Török & Kliem 2005) was considered to explain the initiation of CMEs, e.g., Fan & Gibson (2004) performed isothermal MHD simulations of the three-dimensional evolution of the coronal magnetic field as a twisted magnetic flux tube emerges gradually into a pre-existing coronal arcade. In addition, there are other trigger mechanisms: the shear (or twist) motion of the footpoints of the magnetic arcades (Mikic et al. 1988; Kusano et al. 2004b), the decay of the background magnetic field (Isenberg et al. 1993), the buoyancy force due to filament mass drainage (Low 2001; Zhou et al. 2006), and Moreton & EIT waves generated by a remote CME (Ballester 2006).

After CMEs are initiated, they accelerate and depart from the Sun at speeds ranging from $<$20 to $\sim$3000 km s^{-1} (average speed of $\sim$480 km s^{-1}) measured from the *SOHO*/LASCO white-light images (Gopalswamy 2006). There have been some studies to find a relationship between the CME speed and several magnetic properties in the CME-productive active regions derived from photospheric magnetic fields. Qiu & Yurchyshyn

(2005) studied 13 CME events and found that there is a strong correlation (CC=0.89) between the total reconnection flux (see Forbes & Lin 2000, and references therein) estimated from photospheric magnetic fields and the velocity of CMEs, even though the number of events is not enough to make a statistically meaningful conclusion. Guo et al. (2007) examined the properties of photospheric line-of-sight magnetic fields in 55 active regions before the onset times of 86 CMEs originating from the active regions investigated. They measured four magnetic parameters, i.e., the tile angle, the total flux, the total length of strong-field and strong-gradient neutral lines, and the effective distance. They found a moderate linear correlation (CC$\sim$0.4) between the parameters and the CME speed for a sample of 86 CMEs.

In this study, magnetic helicity injected through the photosphere of CME-productive active regions is studied to better understand the pre-CME condition, the trigger mechanism and the dynamics of CMEs. In Chapter 6.3.1, two coronal arcades building up to CMEs are examined using the wavelet-enhanced EIT observations to investigate their gradual inflation in relation to helicity injection: (1) a post-eruptive arcade in AR 10720 and (2) an overlying arcade in AR 10898. In addition, day-to-day variation of helicity injection is also investigated for 28 active regions which produced 46 CMEs to find a characteristic injection pattern of helicity in relation to the CME occurrence in Chapter 6.3.2 and to carry out a correlation study between the average helicity injection rate in the active regions and the speed of the CMEs in Chapter 6.3.3.

6.2 Data Selection and Analysis

To study the gradual inflation of active-region coronal arcades prior to CMEs, two different types of events are selected from the wavelet-enhanced EIT images (Stenborg & Cobelli 2003): (1) a post-eruptive arcade (PEA) in AR 10720 which resulted from a preceding eruption and (2) an overlying arcade (OA) in AR 10898 which was located high in the corona and have existed a few days before its slow rise. Note that none of the active regions show a sigmoidal shape in *Yohkoh* SXT or *GOES* SXI soft X-ray images prior to the eruption of the arcades. Instead, the soft X-ray data indicate that there are diffuse arcades similar in morphology to the EUV arcades during the gradual inflation stage and bright flare loops in the wake of the eruption.

The measurement of the height-time profile of the rising arcades was carried out as follows: (1) a reference point on the solar surface is selected as a static feature between the two footpoints of the arcade on EIT images, (2) a fiducial line is marked out along the growing direction of the arcade, (3) the highest point of the arcade is determined as a place where the fiducial line intersects the arcade based on the assumption that the arcade is oriented vertically on the surface. Projection effects are corrected for the fiducial line considering the rotation of the reference point. If the arcade grows in the radial direction, projection effects are further corrected by dividing the projected height of the arcade with respect to the Sun center by the projected distance from the reference point to the Sun center. Both are in the solar radius unit. However, if the arcade is located on the limb, or its growth obviously departs from the radial direction, only the projected distance from the arcade apex to the reference point is recorded. The distance after adding by 1 is then regarded as the height with respect to the Sun center in the solar radius unit. The height

of the resultant CME with time in the LASCO FOV is readily available from the LASCO CME Catalogue[1]. Type II radio emission, if existent, can give some idea of the evolution of the CME in the gap between the FOV of EIT and that of LASCO/C2 (from 1.5 $R_\odot$ to 2.2 $R_\odot$), since it is generally interpreted as plasma emission near the local electron plasma frequency due to electrons accelerated by shock waves. The height of the supposed shock-front is obtained by examining the slowly drifting bands of emission in the radio dynamical spectra. The results of the measurement are listed in Table 6.1.

For the statistical study of day-to-day variation of helicity in active regions in relation to CMEs, 28 active regions which produced 46 CMEs are selected. The 46 CMEs are adopted from the CME list of Guo et al. (2007) in which the CMEs are identified with their originating active regions by investigating not only the CME position angles with respect to the originating active regions but also CME-related phenomena such as soft X-ray flares and EIT brightenings in the active regions.

$\dot{H}_r$ and ΔH_r of the active regions under investigation are calculated from Equations 2.11 and 2.17 with full-disk 96 minute MDI magnetograms following the same procedure described in Section 3.2. From the time profiles of $\dot{H}_r$ and ΔH_r, the two helicity parameters are defined to investigate their relationship with the CME velocity in Section 6.3.3. The first parameter is the absolute value of the average helicity injection rate, $|<\dot{H}_r>|$, which indicates the average amount of injected helicity per unit time to an entire active region. Its definition is described in Section 4.2. To calculate $|<\dot{H}_r>|$, t_0 is set as the start time of each MDI magnetogram data set of the active region under investigation, t_1 as the occurrence time of the CMEs from the active region under investigation, and N as the

[1] http://cdaw.gsfc.nasa.gov/CME_list/

total number of MDI magnetograms in each data set during the time period, Δt, between t_0 and t_1. As for the second parameter, the absolute amount of helicity accumulation at the time of t_1, $|\Delta H_r|$, is used.

6.3 Results

6.3.1 Gradual Inflation of Active-Region Coronal Arcades Building up to CMEs

Post-Eruptive Arcade on 2005 January 15

The PEA on 2005 January 15 was located in AR 10720. The arcade was produced by a Halo CME associated with a M8.6 flare, which peaked in soft X-rays at 06:38 UT (Figure 6.1c). Its eruption about 16 hours later resulted in a Halo CME associated with an X2.6 flare with the peak in soft X-rays at 22:25 UT. Although the arcade was formed as early as about 06:24 UT, it is only taken account into this study beyond the end of the M8.6 flare from about 12:00 UT onward, since the early rising of the PEA is largely attributed to the reconnection of magnetic field lines at higher and higher altitudes in the corona (Priest & Forbes 2002). Figure 6.1a displays a typical PEA which is composed of a series of bipolar coronal loops. The loop footpoints constitute two bright, curved flare ribbons, which are parallel to each other and aligned along the polarity inversion line of the line-of-sight photospheric field (Figure 6.1d). The gradual inflation of the arcade is clearly demonstrated in Figure 6.1a–c, but as time progressed, most loops got more and more dimmer. As of 18:24 UT (Figure 6.1e), only visible are the loops at the western end of the original arcade, whose height-time profile is measured along a fiducial as indicated by the dotted line in Figure 6.1a.

One can see that despite multiple flares occurring in the same active region (as indicated by arrows at the bottom of Figure 6.1d), the group of loops grew quasi-statically in height, at a speed of $\sim$2.6 km s^{-1}, from about 12:12 UT until 22:24 UT when the speed suddenly increased to $\sim$50 km s^{-1}, coincidence with the onset of the flare. It is temporally associated with negative helicity injection from photosphere. Note that there was a significant injection of positive helicity for $\sim$1 day on January 14–15, and then negative helicity starts to be injected with magnetic flux increase. This may suggest that a twisted emerging flux tube of negative helicity is related to the gradual inflation of the PEA. The occurrence of the small flares during the inflation phase might be a result of the magnetic reconnection between the two flux system, as simulated by Kusano et al. (2003b), i.e., the emergence of the helicity in negative sign into existing positive helicity system.

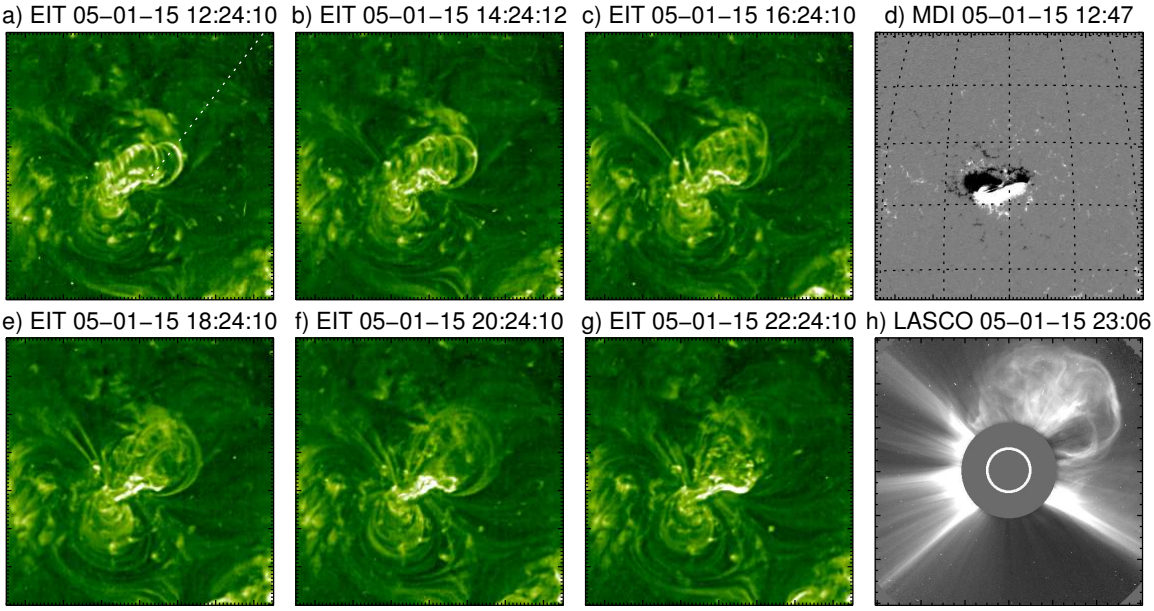

Figure 6.1 Evolution of the PEA observed on 2005 January 15. In frame (a) a fiducial is drawn along the growing direction of the arcade to measure the height of the arcade (see Section 6.2 for details). The field of view in Panels (a–g) is $700'' \times 700''$, centering at $(0'', 350'')$, with all images registered to the image in Panel (a). EIT images in this study are enhanced with a wavelet method based on Stenborg & Cobelli (2003).

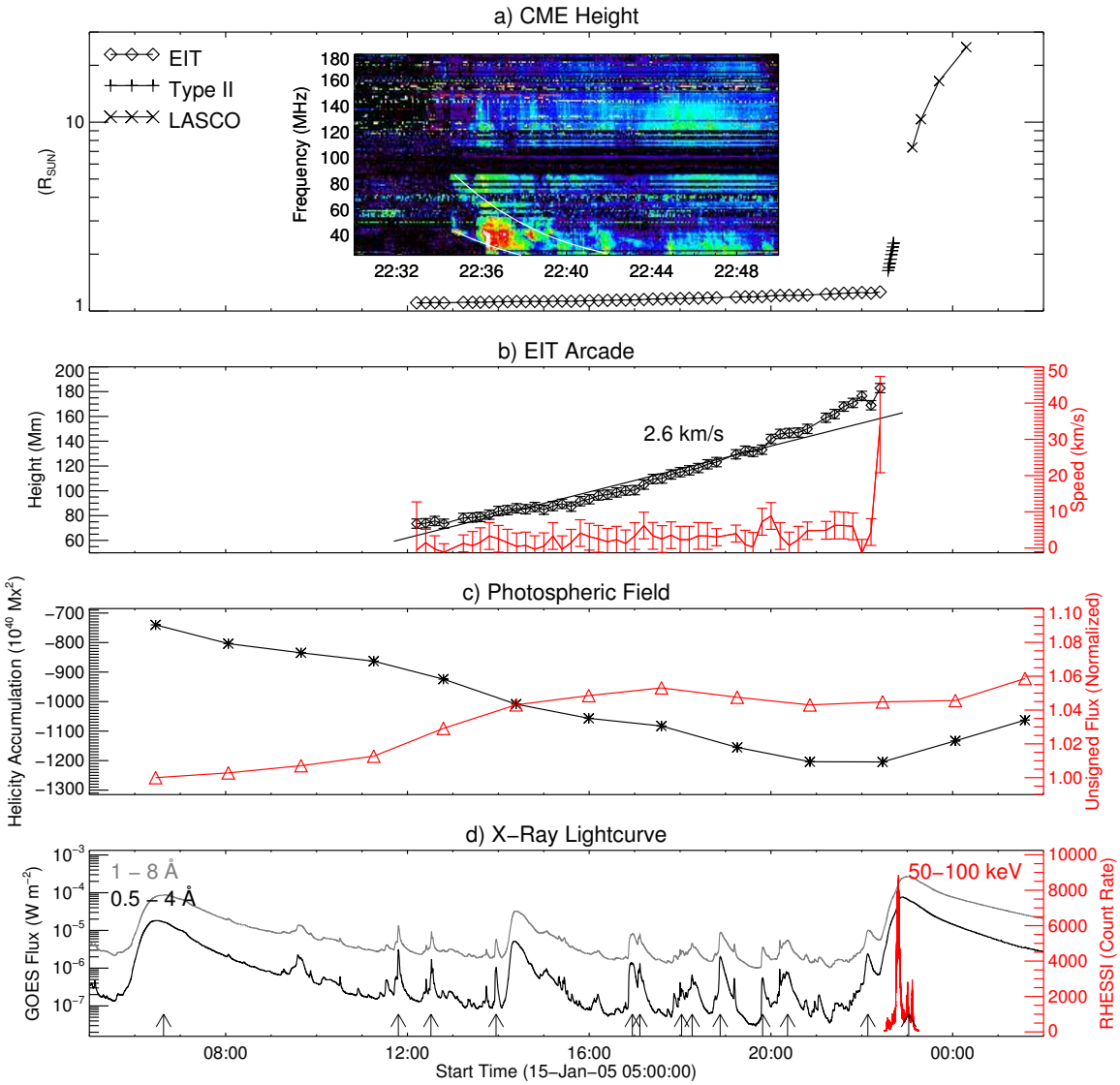

Figure 6.2 Height-time profile of the PEA and the resultant CME on 2005 January 15 in relation to the evolution of the photospheric magnetic field as well as X-ray lightcurves. Panel (a) shows the height-time profiles of the EIT arcade, the shock front obtained from Type II radio emission, and the CME front given by the LASCO CME catalogue, in the solar radius unit. The inset shows the radio dynamical spectra provided by the Radio Solar Telescope Network (RSTN), with the two drifting bands of Type II emission denoted in dashed lines. In Panel (b), the height-time profile of the EIT arcade is given in the Mm unit, and the derived velocity-time profile is displayed in red color and scaled by the y-axis on the right. Panel (c) shows with time the amount of helicity accumulation as well as the unsigned magnetic flux integrated over the active region of interest. Panel (d) shows the *GOES* soft X-ray flux in 1–8 Å (grey) and 0.5–4 Å (black), and the *RHESSI* count rate in 50–100 keV (red). Each flare of *GOES*-class C and above occurring in AR 10720 is plotted with an arrow at the bottom to indicate the soft X-ray flare peak.

Overlying Arcade on 2006 July 4

Figure 6.3 shows the eruption of the OA on the disk on 2006 July 4. The event is much less energetic than the PEA event. The arcade was overlying a decayed active region with a single sunspot, AR 10898 (Figure 6.3d). The gradual inflation of the OA is sustained for about 4.5 hours, at a speed of $<$5km s^{-1}, and the subsequent eruption only resulted in a C-class flare (Figure 6.3d). The flare was associated with a slow CME. Like the PEA event, the morphology of the resultant CME bears similarity to the inflating arcade.

In the 2006 July 4 event, the OA of interest only became illuminated at 14:48 UT, and its growth and subsequent eruption was observed henceforth. The loops on 2006 July 4 were located high in the corona from the beginning: the projected half length of the highest loop is about 0.22 R$_\odot$.

One may wonder how this bipolar, potential-like loop became eruptive and resulted in a CME. *GOES* soft X-ray images show highly complex loops underlying the inflating arcade in the active region (Figure 6.3e–g), but there is no sign of twisted or sheared fields, such as the well-known soft X-ray sigmoids. The quasi-static stage in the event was temporally associated with helicity injection. The helicity change rate displayed no obvious change throughout the flare in the 2006 July 4 event (Figure 6.3c). The short-term (several hours) profile of helicity injection is similar to the time-height profile of the OA. One remarkable thing is that there was a significant and continuous helicity injection for $\sim$2 days before the time of the OA gradual inflation study, but magnetic flux change very little in the active region.

Table 6.1 List of Gradually Erupting Coronal Arcades

No.		Arcade				Flare				CME		
	t_i[a]	Δt (hr)	r_i ($R_\odot$)	r_f ($R_\odot$)	v_q[b] (km s^{-1})	Type[c]	Location	GOES	t_a[d]	PA/AW[e] (deg)	v[f] (km s^{-1})	a[g] (m s^{-2})
1	2005-01-15 12:12	10.4	1.11	1.35	2.6	P	N15W05	X2.6	23:06	Halo/360	2861	-127.4*
2	2006-07-04 14:48	4.6	1.22	1.36	4.3	O	S13W14	C1.4	21:30	199/102	308	1.6

Note. —

[a] Measurement start time of the arcades shown in EIT images

[b] Speed obtained by linear fit of the height-time profile at the quasi-static stage.

[c] P (post-flare arcade), O (overlying arcade)

[d] First appearance time in the LASCO/C2 FOV

[e] Position Angle/Angular Width. For halo CMEs, the position angle refers to that of the fiducial adopted.

[f] Linear speed given by the LASCO CME Catalog.

[g] Acceleration given by the LASCO CME Catalog. The * symbol indicates that acceleration is uncertain due to either poor height measurement or a small number of height-time measurements.

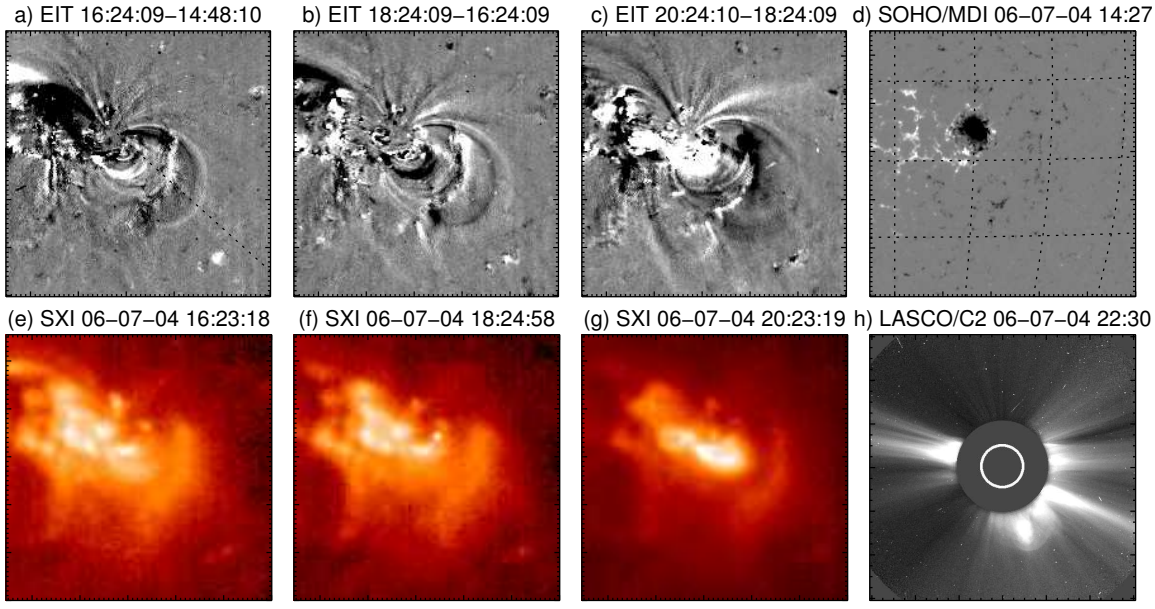

Figure 6.3 Evolution of the OA observed on 2006 July 4. The field of view in Panels (a–g) is 550 by 550 arcsecs, centering at $(225'', -225'')$, with all images registered to the image in Panel (a).

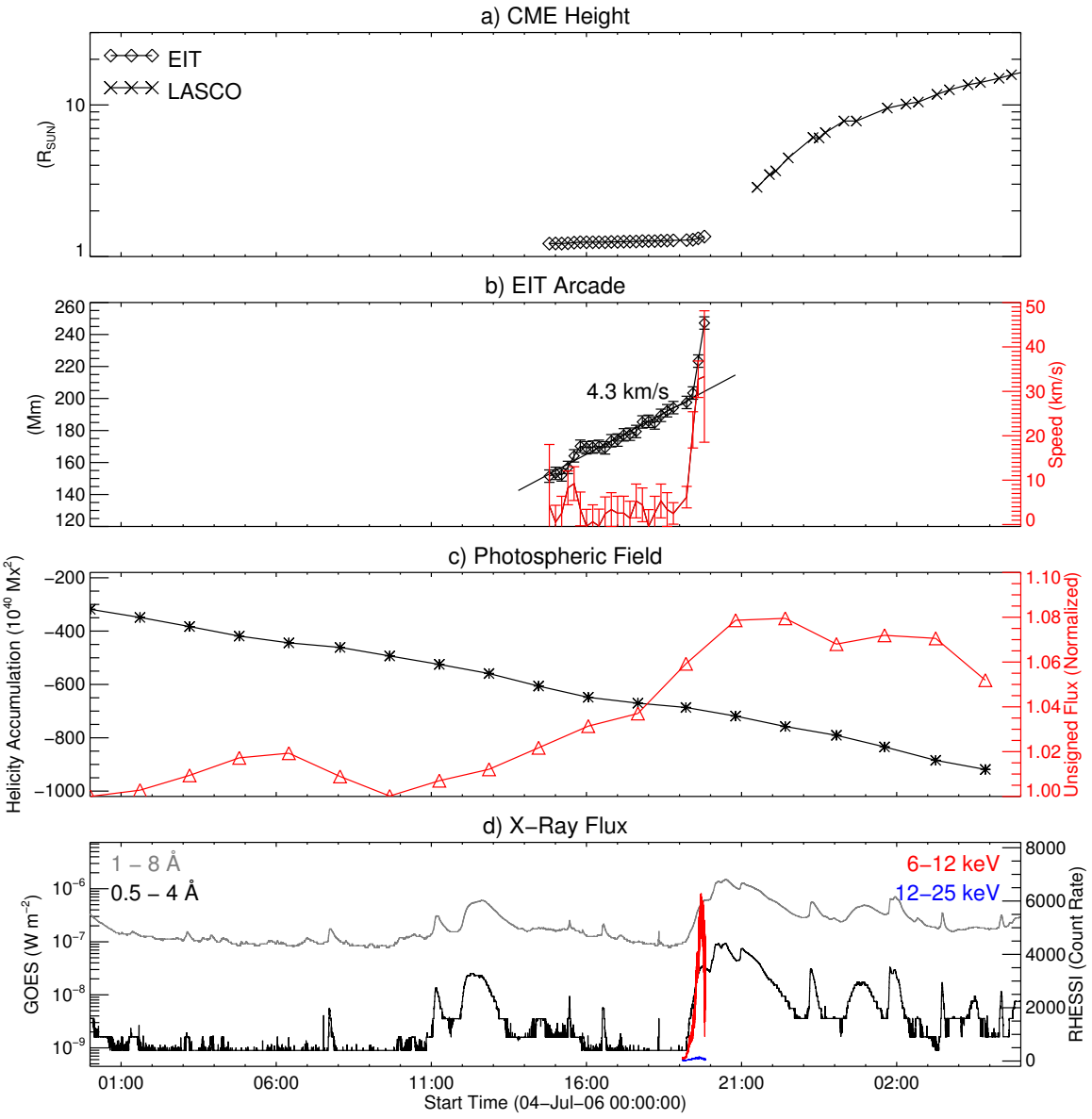

Figure 6.4 Height-time profile of the OA and the resultant CME on 2007 July 4 in relation to the evolution of the photospheric magnetic field as well as X-ray lightcurves.

6.3.2 Two Characteristic Patterns of Helicity Injection before CMEs

The 46 CMEs under investigation can be categorized into two different groups by two characteristic evolution patterns of helicity injection in their active regions: (1) monotonically increasing of helicity (*Group A*, 30 CMEs in 23 active regions) and (2) significant helicity injection followed by its sign reversal (*Group B*, 16 CMEs in 5 active regions).

Figures 6.5, 6.6, and 6.7 present long-term (a few days) variations of the magnetic helicity calculated for 23 active regions in *Group A*. The helicity injection pattern of 5 active regions in *Group B* are also shown in Figure 6.8. The average speed of CMEs in *Group A* is 870 km s^{-1} and 1330 km s^{-1} in *Group B*. The CME speed of *Group B* is much faster than that of *Group A*. There is also a significant difference in the CME acceleration between *Group A* (-24.4m s^{-2}) and *Group B* (-6.3m s^{-2}). Furthermore, the CMEs in *Group A* tend to be single events, while those in *Group B* mainly consist of successive events.

These differences may indicate different pre-CME conditions and trigger mechanisms for the two groups. CMEs in *Group A* seem to be associated with the kink instability. CMEs in *Group B* might be involved with the emergence of opposite sense of helicity into an existing helicity system, and perhaps an interaction between two helicity systems may be responsible for the CMEs in *Group B*. Further statistical studies, however, are needed to check whether the two characteristic helicity patterns are shown in other CME-productive active regions. In Table 6.2, the difference between *Group A* and *Group B* is summarized.

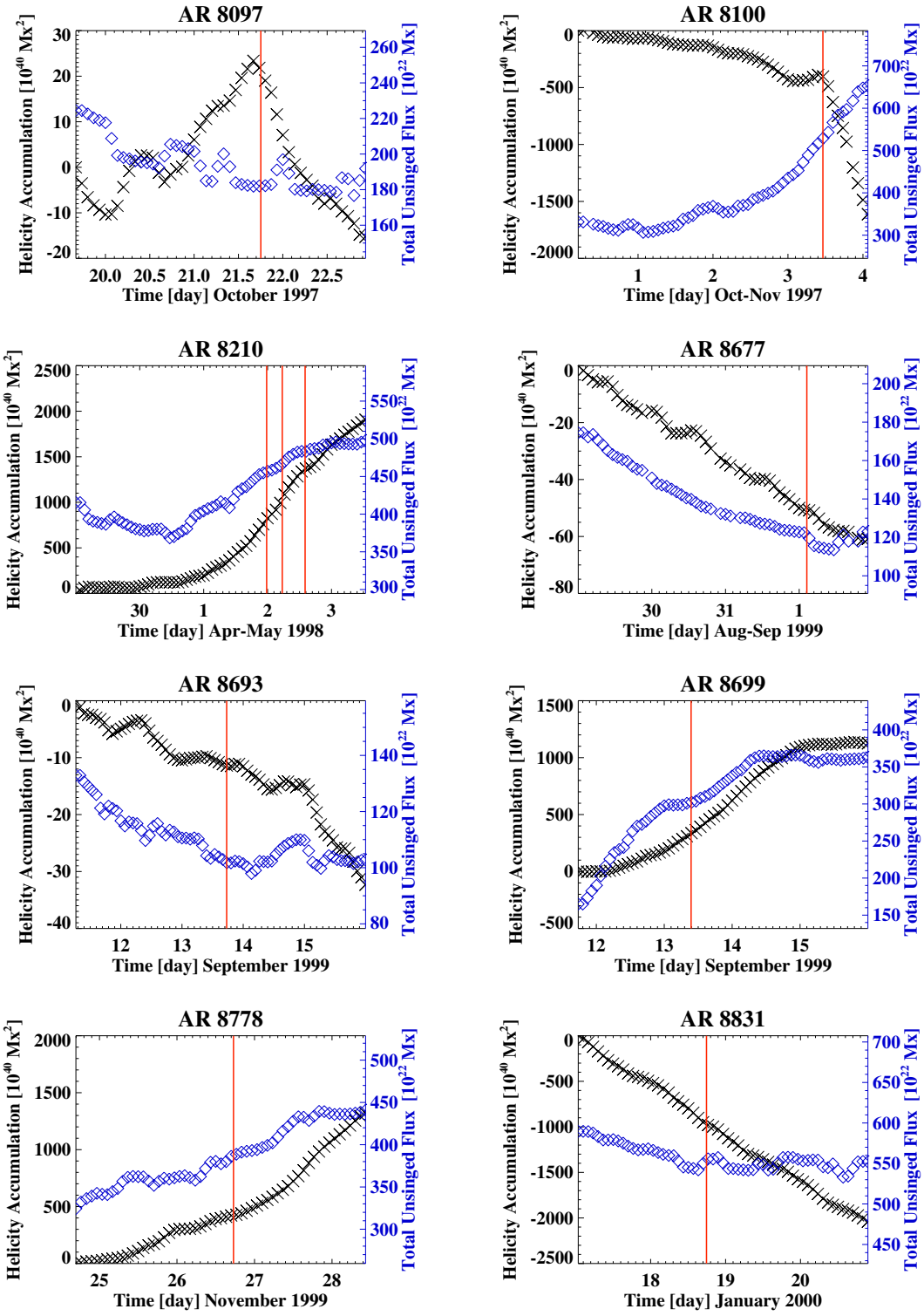

Figure 6.5 Time variation of helicity accumulation (black crosses) and unsigned magnetic flux (blue diamonds) for 8 active regions in *Group A*. The active regions in *Group A* show a monotonically increasing pattern of helicity for a few days. In each panel, the vertical red lines indicate the times when the CMEs originated from the 8 active regions first appeared in the LASCO/C2 FOV.

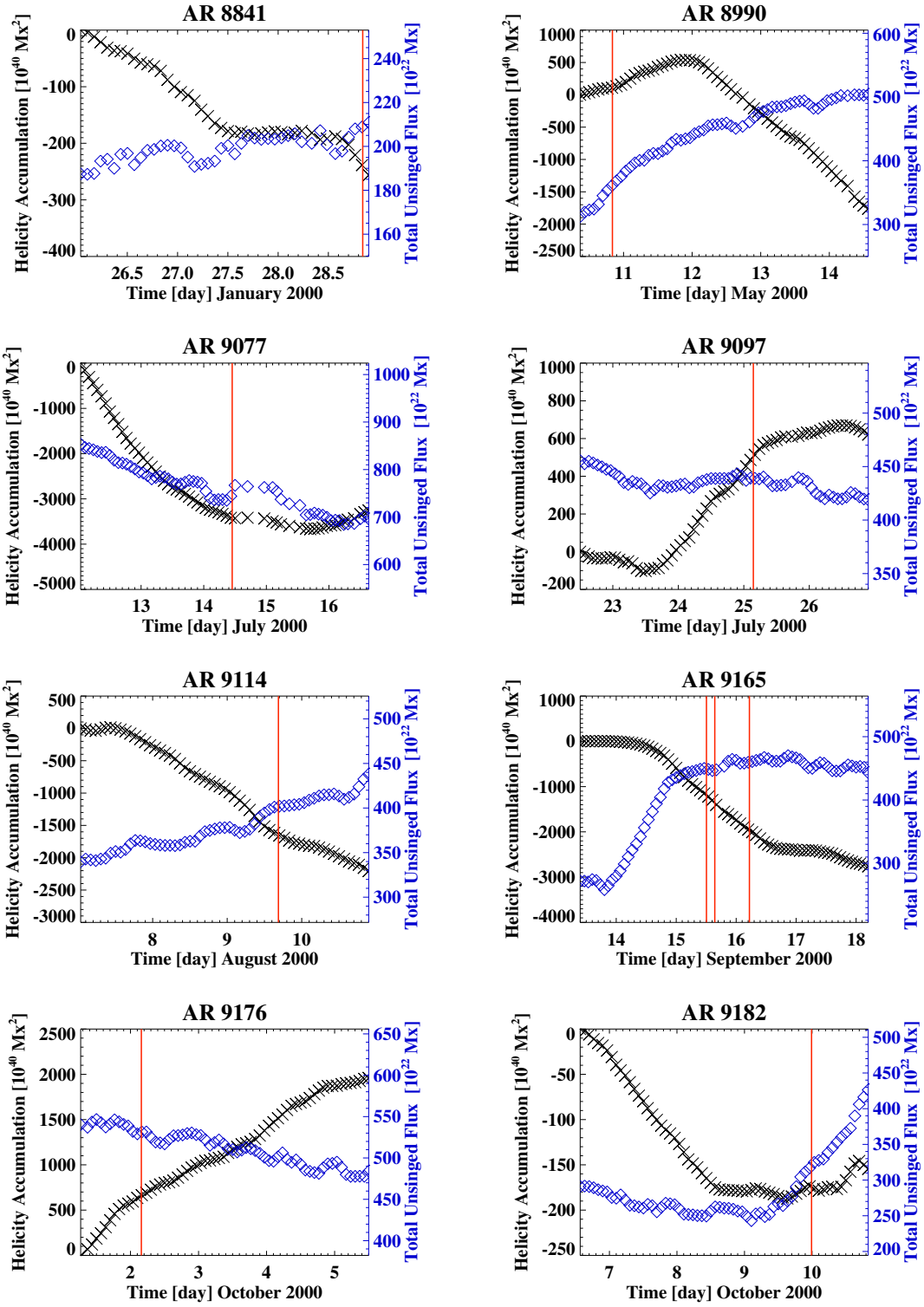

Figure 6.6 Same as in Figure 6.5, but for additional 8 active regions in *Group A*.

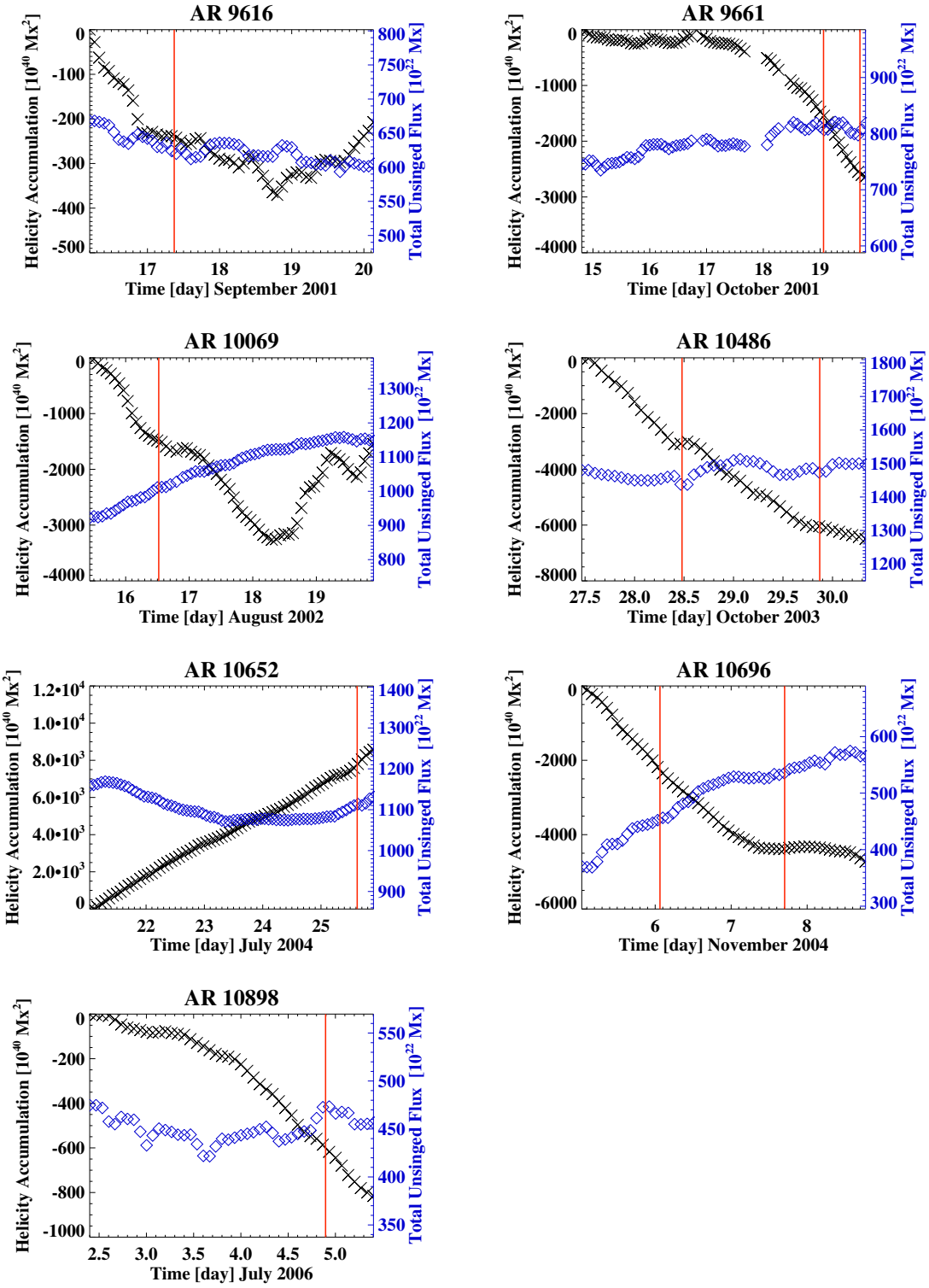

Figure 6.7 Same as in Figure 6.5, but for additional 7 active regions in *Group A*.

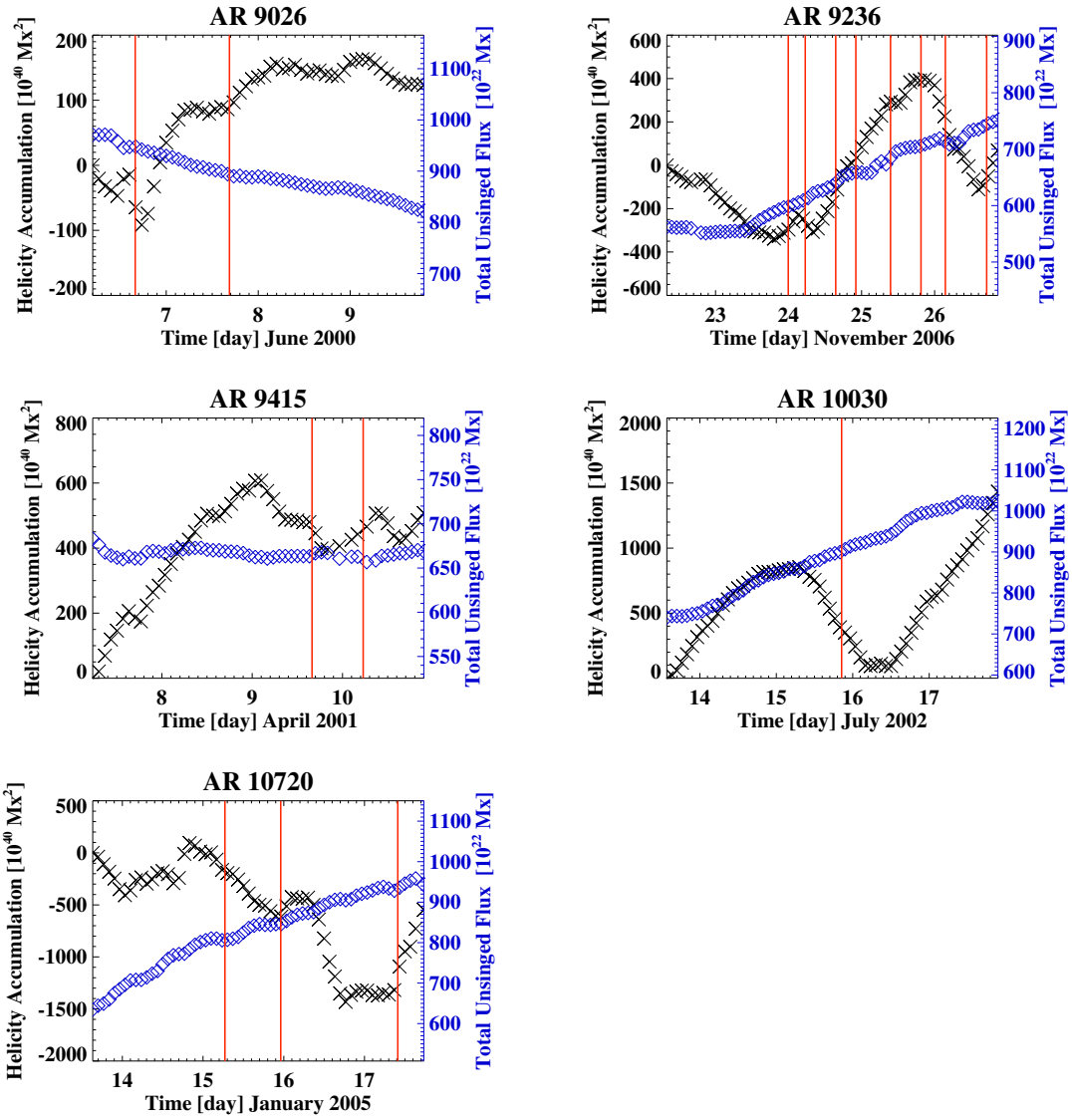

Figure 6.8 Same as in Figure 6.5, but for 5 active regions in *Group B* indicating a pattern of significant helicity injection followed by its sign reversal. A total of 16 CMEs occurred from the 5 active regions during the period when the helicity injection rate in the active regions started to reverse its sign.

6.3.3 Correlation of Helicity Injection with CME Speed

The 30 CMEs in *Group A* were used for the study of helicity injection related to the CME speed. Note however that the 16 CMEs in *Group B* were not taken account into this CME speed study because it is not easy to define a parameter of helicity injection in the active regions of *Group B* which frequently show helicity reversal during the helicity injection period before the CMEs. The two helicity parameters ($|<\dot{H}_r>|$ and $|\Delta H_r|$) defined in Section 6.2 were investigated.

Figure 6.9a and b show the CME speed versus $|<\dot{H}_r>|$ and $|\Delta H_r|$ in a logarithmic scale as cross symbols, respectively, and the solid lines indicate the least-squares linear fits to the data points. The CCs of the linear fits are also given in each panel. Figure 3.4a shows that there is a fairly good correlation (CC=0.71) between $|<\dot{H}_r>|$ and the CME velocity. $|\Delta H_r|$ also shows a modest correlation with F_X (CC=0.64) as shown in Figure 3.4b. On the other hand, the correlation between helicity parameters and the CME acceleration in Figure 3.4c and d is very poor with a weak tendency that the larger helicity injection in active regions is, the larger deceleration of high-speed CMEs is.

Table 6.2 Comparison between *Group A* and *Group B*

Group	CME Number	v_{avg}/v_{med} [a] (km s^{-1})	a_{avg}/a_{med} [b] (m s^{-2})	CME Event Type	Helicity Injection Pattern
A	30	870/700	-24.4/-8.7	Single	Continuous injection followed by no (or a little) injection for a while
B	16	1330/1150	-6.3/-0.8	Successive	Significant injection followed by its sign reversal

[a] Average Velocity/Median Velocity

[b] Average Acceleration/Median Acceleration

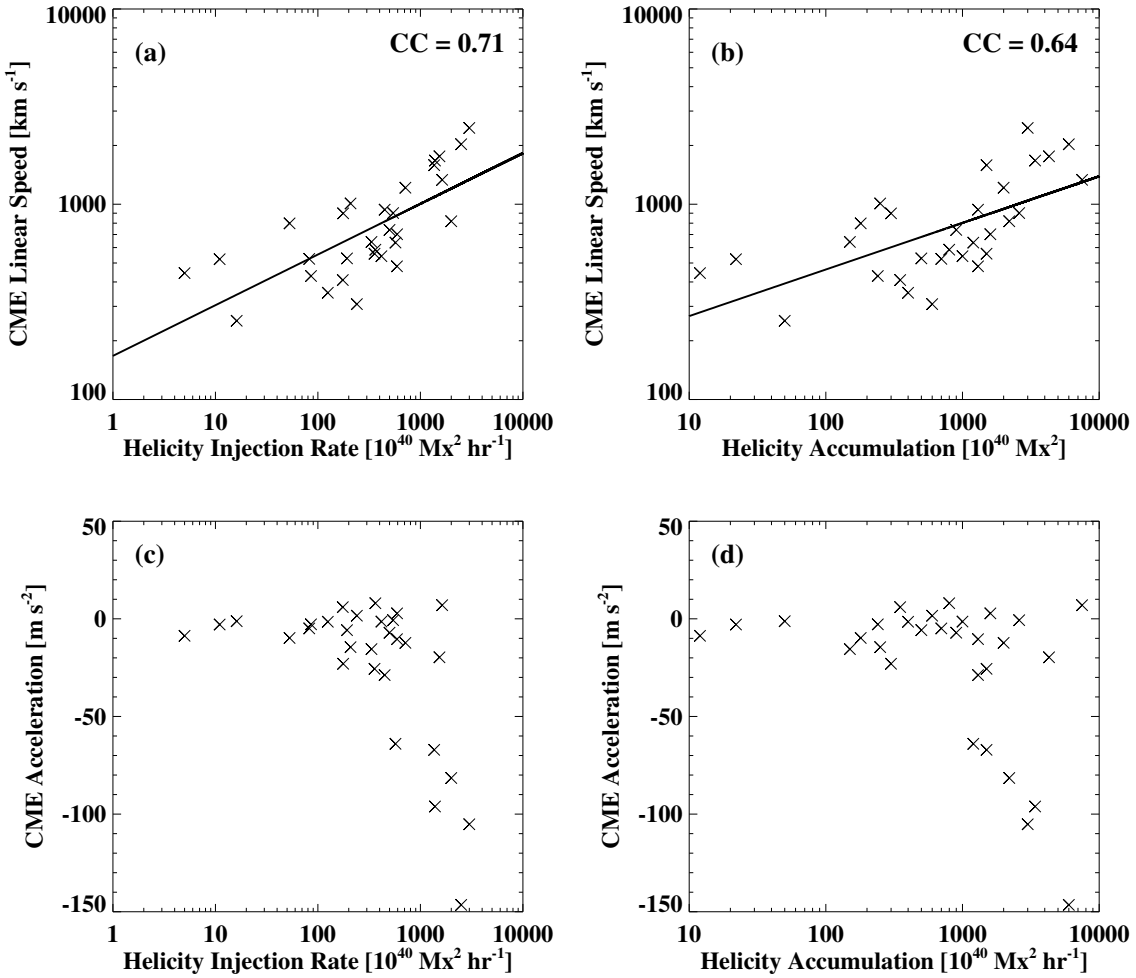

Figure 6.9 Helicity parameters with the velocity and acceleration of 30 CMEs originated from 23 active regions in *Group A*. Correlations of the CME velocity with (a) the absolute average helicity injection rate, $|<\dot{H}_r>|$, and (b) the absolute helicity accumulation $|\Delta H_r|$. The solid line indicates the least-square linear fit, and CC is specified in each panel. The CME speed shows a fairly good correlation with the helicity parameters (The linear CCs are 0.71 and 0.64 for $|<\dot{H}_r>|$ and $|\Delta H_r|$, respectively. The CME acceleration is plotted versus (c) $|<\dot{H}_r>|$, and (d) $|\Delta H_r|$. See Table 6.3 for the detailed information of the 30 CMEs.

Table 6.3 Helicity Injection in 23 Active Regions Producing 30 CMEs in *Group A*

No.	t_a	CME PA/AW (deg)	v (km s^{-1})	a (m s^{-2})	Helicity $\lvert<\dot{H}_r>\rvert$[a] (10^{70} Mx^2 hr^{-1})	$\lvert\Delta H_r\rvert$[b] (10^{40} Mx^2)	$\Delta\tau$ (day)	Flare t_s[c]	Flare GOES	AR No.
1	1997-10-21 18:03	Halo/360	523	-2.9	0.5	22	2	17:00	C3.3	8097
2	1997-11-03 11:11	232/122	352	-1.5	5.2	400	3.2	09:13	M1.4	8100
3	1998-05-01 23:40	Halo/360	585	8.0	15.2	800	2.2	21:40	C2.6	8210
4	1998-05-02 05:31	Halo/360	542	-1.4	17.4	1000	2.4	04:48	C5.4	8210
5	1998-05-02 14:06	Halo/360	938	-28.8	18.7	1300	2.9	13:31	X1.1	8210
6	1999-09-01 02:30	188/283	253	-1.2*	0.7	50	3.1	23:56⋆	C2.7	8677
7	1999-09-13 17:31	109/184	444	-8.7*	0.2	12	2.4	16:38	C2.6	8693
8	1999-09-13 09:30	0/182	898	-23	7.4	300	1.7	08:05	C4.9	8699
9	1999-11-26 17:30	228/145	409	6.0	7.3	350	2.0	17:40	C2.3	8778
10	2000-01-18 17:54	Halo/360	739	-7.1	20.8	900	1.8	17:10	M3.9	8831
11	2000-01-28 20:12	70/20	429	-2.8	3.6	240	2.8	19:45	C4.7	8841
12	2000-05-10 20:06	83/205	641	-15.5	13.9	150	0.5	19:32	C8.7	8990
13	2000-07-14 10:54	Halo/360	1674	-96.1	57.8	3400	2.5	10:03	X5.7	9077
14	2000-07-25 03:30	Halo/360	528	-5.8	8.0	500	2.6	02:47	M8.0	9097
15	2000-08-09 16:30	Halo/360	702	2.8	24.7	1600	2.7	15:33	C2.3	9114
16	2000-09-15 12:06	249/235	633	-64.0*	23.8	1200	2.1	10:54	C9.5	9165
17	2000-09-15 15:26	217/210	481	-10.4*	24.6	1300	2.2	14:31	M2.0	9165
18	2000-09-16 05:18	Halo/360	1215	-12.3	29.8	2000	2.8	04:07	M5.9	9165
19	2000-10-02 03:50	Halo/360	525	-4.9	3.4	700	8.5	02:47	C4.1	9176
20	2000-10-09 23:50	Halo/360	798	-9.8	2.2	180	3.4	23:22	C6.7	9182
21	2001-09-17 08:54	198/166	1009	-14.5	8.7	250	1.2	08:18	M1.5	9616
22	2001-10-19 01:27	Halo/360	558	-25.6	14.9	1500	4.2	00:47	X1.6	9661
23	2001-10-19 16:50	Halo/360	901	-0.7	22.6	2600	4.8	16:13	X1.6	9661
24	2002-08-16 12:30	Halo/360	1585	-67.1	56.8	1500	1.1	11:32	M5.2	10069
25	2003-10-28 11:30	Halo/360	2459	-105.2	125.0	3000	1.0	10:01	X17.2	10486
26	2003-10-29 20:54	Halo/360	2029	-146.5	104.2	6000	2.4	20:37	X10	10486

6.4 Summary

Two coronal arcade events are examined: (1) a PEA in AR 10720 and (2) an OA in AR 10898. As a result, it is found that the quasi-static inflation stage sustains for hours at a speed of less than 5 km s^{-1}, and it is temporally associated with helicity injection from the active-region photosphere. In addition, an average injection rate of helicity during a few days is also investigated for 28 active regions which produced 46 CMEs. The CMEs under investigation are categorized into two different groups by the two characteristic evolution patterns of helicity injection in their active regions: (1) a monotonically increasing pattern with one sign of helicity (*Group A*, 30 CMEs in 23 active regions) and (2) a pattern of significant helicity injection followed by its sign reversal (*Group B*, 16 CMEs in 5 active regions). It is suspected that these two groups may have different preconditions and trigger mechanisms. CMEs in Group A are associated with kink instability. CMEs in *Group B* are involved with emergence of the helicity in the opposite sign into existing helicity system. A fairly good correlation (CC=0.71) between the helicity injection and the speed of 30 CMEs in *Group A* is found.

Table 6.3—Continued

No.	t_a	CME PA/AW (deg)	v (km s^{-1})	a (m s^{-2})	Helicity $\lvert<\dot{H}_r>\rvert$[a] (10^{70} Mx^2 hr^{-1})	Helicity $\lvert\Delta H_r\rvert$[b] (10^{40} Mx^2)	$\Delta\tau$ (day)	Flare t_s[c]	Flare GOES	AR No.
27	2004-07-25 14:54	Halo/360	1333	7.0	67.9	7500	4.6	14:19	M1.1	10652
28	2004-11-06 01:31	Halo/360	818	-81.5	83.3	2200	1.1	00:44	M5.9	10696
29	2004-11-07 16:54	Halo/360	1759	-19.7	64.0	4300	2.8	15:42	X2.0	10696
30	2006-07-04 21:30	199/102	308	1.6	10.0	600	2.5	19:06	C1.4	10898

[a] The absolute value of the average helicity injection rate during the period $\delta\tau$

[b] The absolute value of helicity accumulation just during the period $\delta\tau$

[c] Flare start time. $\star$ indicates the time on the day prior to the date given in the first column of the table.

CHAPTER 7

SUMMARY OF THE DISSERTATION AND FUTURE WORK

This dissertation is focused on the magnetic helicity in solar active regions and its relationship with solar eruptions such as flares and CMEs. The injection of magnetic helicity was investigated over a span of several days around the times of: (1) flares above *GOES* B-class which occurred in a total of ∼400 active regions, (2) two active-region coronal arcades which build up to CMEs, and (3) 46 CMEs in 28 active regions. There are four major findings, as summarized below, that help to understand the long-term evolution of the large-scale magnetic field topology and non-potentiality in active regions related to solar eruptive events.

First, it is found that there are two characteristic phases in the long-term (a few days) variation of magnetic helicity related to a potential precursor of solar eruptions. The major flares and CMEs under investigation are always preceded by a significant magnetic helicity injection of 10^{42}–10^{43} Mx^2 over a long period (0.5–a few days) in the active-region corona through the photosphere. Furthermore, the magnetic helicity in the flare/CME-productive active regions accumulates at a nearly constant rate and then its injection rate starts to become slow (sometimes almost zero) or reverses its sign around the occurrence time of the flares and CMEs.

Second, statistical studies of flare productivity and magnetic helicity injection shows that the 24 hr average helicity injection rate in an active region has a good correlation with the active region's *GOES* soft X-ray peak flux in next 24 hr following the helicity measurement. The larger flare index an active region has, the larger value of the helicity injection

rate it presents. For a sub-sample of 91 large active regions in the range (3–5)$\times 10^{22}$ Mx of large unsigned magnetic flux, there is a difference in magnetic helicity injection rate between flaring active regions and non-flaring active regions by a factor of 2. On the other hand, 118 active regions in the range (2–10)$\times 10^{40}$ Mx^2 hr^{-1} of large helicity injection rate do not show the significant difference in unsigned magnetic flux between the flaring and non-flaring groups.

Third, the study of the coronal magnetic helicity in the active region NOAA 10930 indicates that the time profile of the coronal helicity roughly corresponds to that of the helicity accumulation by the injection through the photospheric surface. First time the 3D coronal helicity is calculated based on NLFF extrapolation. In addition, it is found that there are two characteristic phases of day-to-day variation of helicity related to the X3.4 flare on 2006 December 13: a large increase of negative helicity, -3.2×10^{43} Mx^2, in the corona over $\sim$1.5 days followed by a noticeable injection of positive helicity though the photospheric surface around the flaring magnetic polarity inversion line.

Finally, the study of two active-region coronal arcades shows that the gradual inflation stage of the coronal arcades sustains for hours at a speed of less than 5 km/s, and it is temporally associated with the steady injection phase of helicity from the active-region photosphere. In addition, the speed of CMEs measured at the height of 1.5–2.2 $R_\odot$ is well proportional to the average helicity injection rate in the CME-productive active regions during the period of a few days before the CMEs.

Based on these results, characteristic variation patterns and injection rates of magnetic helicity in flare/CME-productive active regions can be used for the improvement of solar eruption forecasting: (1) an early warning sign of flare/CME occurrence could be

given by the presence of a phase of monotonically increasing helicity as it is found that all the major flares and CMEs under investigation occur after significant helicity accumulation; (2) an urgent warning sign of flare/CME occurrence could be also made when helicity injection rate becomes very slow or the opposite sign of helicity starts to be injected after the significant helicity accumulation in active regions; and (3) a potential strength of future eruptions (i.e., the soft X-ray intensity of flares and the speed of CMEs) can be estimated by the statistical studies of the correlation between the average helicity injection rate in active regions and the strength of the previous eruptive events.

As a concluding remark to this dissertation, the future studies based on solid results in this dissertation are outlined below:

- *Extended study of the 3D coronal magnetic helicity in eruptive active regions should be made using full-disk photospheric vector magnetograms with high spatial and temporal resolution taken by the Helioseismic and Magnetic Imager (HMI) onboard the SDO to understand the possible triggering mechanism of flare/CMEs;*

- *Magnetic helicity injected in the deepest layers of photosphere should be investigated using infrared vector magnetograms taken by the Infra-Red Imaging vector Magnetograph (IRIM) which is being installed in the Coudé Lab of the New Solar Telescope (NST)/BBSO;*

- *For more practical and advanced flare/CME forecasting, a way to better characterize the time history of helicity injection as well as its spatial distribution inside active regions needs to be developed;*

- *Magnetic helicity injection in active regions should be examined related to the very*

initial stage of CMEs including expanding active-region coronal loops that evolve to produce CMEs (e.g., post-eruptive arcades, overlying arcades, and transequatorial loops);

- *Observational findings on this helicity study should be carefully checked with aspects shown in flare/CME numerical simulations to further understand the physics underlying solar eruption phenomena.*

REFERENCES

Abramenko, V., Yurchyshyn, V., & Wang, H. 2008, Astrophys. J., 681, 1669.

Abramenko, V. I. 2005, Astrophys. J., 629, 1141.

Abramenko, V. I., Yurchishin, V. B., & Wang, T. J. 1996, Radiophysics and Quantum Electronics, 39, 930.

Acton, L., Tsuneta, S., Ogawara, Y., Bentley, R., Bruner, M., Canfield, R., Culhane, L., Doschek, G., Hiei, E., & Hirayama, T. 1992, Science, 258, 618.

Alissandrakis, C. E. 1981, Astron. Astrophys., 100, 197.

Antalova, A. 1996, Contributions of the Astronomical Observatory Skalnate Pleso, 26, 98.

Antiochos, S. K. 1998, Astrophys. J. Lett., 502, L181.

Antiochos, S. K., DeVore, C. R., & Klimchuk, J. A. 1999, Astrophys. J., 510, 485.

Bak, P., Tang, C., & Wiesenfeld, K. 1987, Physical Review Letters, 59, 381.

Baker, D. N. 2004, Lecture Notes in Physics, 656, 3.

Balch, C. C. 2008, Space Weather, 6, 1001.

Ballester, J. L. 2006, Royal Society of London Philosophical Transactions Series A, 364, 405.

Bao, S. & Zhang, H. 1998, Astrophys. J. Lett., 496, L43.

Bélanger, E., Vincent, A., & Charbonneau, P. 2007, Sol. Phys., 245, 141.

Berger, M. A. 1999, in Magnetic Helicity in Space and Laboratory Plasmas, eds. M. R. Brown, R. C. Canfield, & A. A. Pevtsov (Washington: American Geophysical Union), 1.

Berger, M. A. & Field, G. B. 1984, Journal of Fluid Mechanics, 147, 133.

Berger, M. A. & Prior, C. 2006, Journal of Physics A Mathematical General, 39, 8321.

Berger, M. A. & Ruzmaikin, A. 2000, J. Geophys. Res., 105, 10481.

Bieber, J. W., Evenson, P., & Matthaeus, W. H. 1987a, Geophys. Res. Lett., 14, 864.

Bieber, J. W., Evenson, P. A., & Matthaeus, W. H. 1987b, Astrophys. J., 315, 700.

Bray, R. J. & Loughhead, R. E. 1979, Sunspots (New York: Dover Publications).

Brown, T. M. & Christensen-Dalsgaard, J. 1998, Astrophys. J. Lett., 500, L195.

Burlaga, L. F. 1988, J. Geophys. Res., 93, 7217.

Cameron, R. & Sammis, I. 1999, Astrophys. J. Lett., 525, L61.

Canfield, R. C., de La Beaujardiere, J., Fan, Y., Leka, K. D., McClymont, A. N., Metcalf, T. R., Mickey, D. L., Wuelser, J., & Lites, B. W. 1993, Astrophys. J., 411, 362.

Canfield, R. C., Hudson, H. S., & McKenzie, D. E. 1999, Geophys. Res. Lett., 26, 627.

Carmichael, H. 1964, NASA Special Publication, 50, 451.

Carrington, R. C. 1859, Mon. Not. R. Astron. Soc., 20, 13.

Chae, J. 2001, Astrophys. J. Lett., 560, L95.

—. 2007, Advances in Space Research, 39, 1700.

Chae, J. & Jeong, H. 2005, Journal of Korean Astronomical Society, 38, 295.

Chae, J., Moon, Y., & Park, Y. 2004, Sol. Phys., 223, 39.

Chae, J., Moon, Y., Rust, D. M., Wang, H., & Goode, P. R. 2003, Journal of Korean Astronomical Society, 36, 33.

Chae, J. & Sakurai, T. 2008, Astrophys. J., 689, 593.

Chandra, R., Pariat, E., Schmieder, B., Mandrini, C. H., & Uddin, W. 2010, Sol. Phys., 261, 127.

Chen, P. F. 2008, Journal of Astrophysics and Astronomy, 29, 179.

—. 2009, Astrophys. J. Lett., 698, L112.

Chen, P. F. & Shibata, K. 2000, Astrophys. J., 545, 524.

Chen, W., Liu, C., Song, H., Deng, N., Tan, C., & Wang, H. 2007, Chinese Journal of Astronomy and Astrophysics, 7, 733.

Choe, G. S. & Lee, L. C. 1996, Astrophys. J., 472, 372.

Choudhuri, A. R., Chatterjee, P., & Nandy, D. 2004, Astrophys. J. Lett., 615, L57.

De Rosa, M. L., Schrijver, C. J., Barnes, G., Leka, K. D., Lites, B. W., Aschwanden, M. J., Amari, T., Canou, A., McTiernan, J. M., Régnier, S., Thalmann, J. K., Valori, G., Wheatland, M. S., Wiegelmann, T., Cheung, M. C. M., Conlon, P. A., Fuhrmann, M., Inhester, B., & Tadesse, T. 2009, Astrophys. J., 696, 1780.

Démoulin, P. & Berger, M. A. 2003, Sol. Phys., 215, 203.

Deng, N., Liu, C., Yang, G., Wang, H., & Denker, C. 2005, Astrophys. J., 623, 1195.

DeVore, C. R. 2000, Astrophys. J., 539, 944.

Dunn, R. B. & Zirker, J. B. 1973, Sol. Phys., 33, 281.

Eto, S., Isobe, H., Narukage, N., Asai, A., Morimoto, T., Thompson, B., Yashiro, S., Wang, T., Kitai, R., Kurokawa, H., & Shibata, K. 2002, PASJ, 54, 481.

Fan, Y. 2009, Astrophys. J., 697, 1529.

Fan, Y. & Gibson, S. E. 2004, Astrophys. J., 609, 1123.

Feynman, J. & Martin, S. F. 1995, J. Geophys. Res., 100, 3355.

Finn, J. M. & Antonsen, T. M. 1985, Comments Plasma Phys. Controlled Fusion, 9, 111.

Forbes, T. G. & Lin, J. 2000, Journal of Atmospheric and Solar-Terrestrial Physics, 62, 1499.

Forbes, T. G. & Priest, E. R. 1995, Astrophys. J., 446, 377.

Fröhlich, C. & Lean, J. 1998, Geophys. Res. Lett., 25, 4377.

Fry, C. D., Dryer, M., Smith, Z., Sun, W., Deehr, C. S., & Akasofu, S. 2003, Journal of Geophysical Research (Space Physics), 108, 1070.

Fry, C. D., Sun, W., Deehr, C. S., Dryer, M., Smith, Z., Akasofu, S., Tokumaru, M., & Kojima, M. 2001, J. Geophys. Res., 106, 20985.

Gaizauskas, V., Zirker, J. B., Sweetland, C., & Kovacs, A. 1997, Astrophys. J., 479, 448.

Gallagher, P. T., Moon, Y., & Wang, H. 2002, Sol. Phys., 209, 171.

Gilbert, H. R., Holzer, T. E., Burkepile, J. T., & Hundhausen, A. J. 2000, Astrophys. J., 537, 503.

Glover, A., Ranns, N. D. R., Harra, L. K., & Culhane, J. L. 2000, Geophys. Res. Lett., 27, 2161.

Gopalswamy, N. 2006, Journal of Astrophysics and Astronomy, 27, 243.

Gopalswamy, N., Shimojo, M., Lu, W., Yashiro, S., Shibasaki, K., & Howard, R. A. 2003, Astrophys. J., 586, 562.

Guo, J., Zhang, H. Q., & Chumak, O. V. 2007, Astron. Astrophys., 462, 1121.

Guo, Y., Ding, M. D., Wiegelmann, T., & Li, H. 2008, Astrophys. J., 679, 1629.

Guo, Y., Schmieder, B., Bommier, V., & Gosain, S. 2010, Sol. Phys., 262, 35.

Hagino, M. & Sakurai, T. 2005, PASJ, 57, 481.

Hagyard, M. J. & Rabin, D. M. 1986, Advances in Space Research, 6, 7.

Hagyard, M. J., Teuber, D., West, E. A., & Smith, J. B. 1984, Sol. Phys., 91, 115.

Hale, G. E. 1908, Astrophys. J., 28, 315.

—. 1927, Nature, 119, 708.

Hale, G. E., Ellerman, F., Nicholson, S. B., & Joy, A. H. 1919, Astrophys. J., 49, 153.

Hartkorn, K. & Wang, H. 2004, Sol. Phys., 225, 311.

Heyvaerts, J., Priest, E. R., & Rust, D. M. 1977, Astrophys. J., 216, 123.

Hirayama, T. 1974, Sol. Phys., 34, 323.

Hodgson, R. 1859, Mon. Not. R. Astron. Soc., 20, 15.

Hood, A. W. & Priest, E. R. 1981, Geophysical and Astrophysical Fluid Dynamics, 17, 297.

Hudson, H. S., Lemen, J. R., St. Cyr, O. C., Sterling, A. C., & Webb, D. F. 1998, Geophys. Res. Lett., 25, 2481.

Illing, R. M. E. & Hundhausen, A. J. 1986, J. Geophys. Res., 91, 10951.

Isenberg, P. A., Forbes, T. G., & Demoulin, P. 1993, Astrophys. J., 417, 368.

Jenkins, J. L. 2009, The Sun and How to Observe It (Berlin: Springer Verlag).

Jeong, H. & Chae, J. 2007, Astrophys. J., 671, 1022.

Ji, H., Wang, H., Liu, C., & Dennis, B. R. 2008, Astrophys. J., 680, 734.

Jing, J., Qiu, J., Lin, J., Qu, M., Xu, Y., & Wang, H. 2005, Astrophys. J., 620, 1085.

Jing, J., Tan, C., Yuan, Y., Wang, B., Wiegelmann, T., Xu, Y., & Wang, H. 2010, Astrophys. J., 713, 440.

Jing, J., Wiegelmann, T., Suematsu, Y., Kubo, M., & Wang, H. 2008, Astrophys. J. Lett., 676, L81.

Jing, J., Yurchyshyn, V. B., Yang, G., Xu, Y., & Wang, H. 2004, Astrophys. J., 614, 1054.

Kiepenheuer, K. O. 1953, The Sun (Ann Arbor: University of Michigan Press).

Kliem, B., Titov, V. S., & Török, T. 2004, Astron. Astrophys., 413, L23.

Klimchuk, J. A., Canfield, R. C., & Rhoads, J. E. 1992, Astrophys. J., 385, 327.

Kopp, R. A. & Pneuman, G. W. 1976, Sol. Phys., 50, 85.

Kubo, M., Yokoyama, T., Katsukawa, Y., Lites, B., Tsuneta, S., Suematsu, Y., Ichimoto, K., Shimizu, T., Nagata, S., Tarbell, T. D., Shine, R. A., Title, A. M., & Elmore David. 2007, PASJ, 59, 779.

Kusano, K. 2005, Astrophys. J., 631, 1260.

Kusano, K., Maeshiro, T., Yokoyama, T., & Sakurai, T. 2002, Astrophys. J., 577, 501.

—. 2003a, Advances in Space Research, 32, 1917.

—. 2004a, in Astronomical Society of the Pacific Conference Series, Vol. 325, The Solar-B Mission and the Forefront of Solar Physics, eds. T. Sakurai & T. Sekii (San Francisco: ASP), 175.

—. 2004b, Astrophys. J., 610, 537.

Kusano, K., Suzuki, Y., & Nishikawa, K. 1995, Astrophys. J., 441, 942.

Kusano, K., Yokoyama, T., Maeshiro, T., & Sakurai, T. 2003b, Advances in Space Research, 32, 1931.

LaBonte, B. J., Georgoulis, M. K., & Rust, D. M. 2007, Astrophys. J., 671, 955.

Lang, K. R. 2001, The Cambridge Encyclopedia of the Sun (Cambridge, UK: Cambridge University Press).

Langhans, K., Scharmer, G. B., Kiselman, D., Löfdahl, M. G., & Berger, T. E. 2005, Astron. Astrophys., 436, 1087.

Leka, K. D. & Barnes, G. 2003a, Astrophys. J., 595, 1277.

—. 2003b, Astrophys. J., 595, 1296.

Li, R., Cui, Y., He, H., & Wang, H. 2008, Advances in Space Research, 42, 1469.

Lim, E., Jeong, H., Chae, J., & Moon, Y. 2007, Astrophys. J., 656, 1167.

Lin, Y., Wei, X., & Zhang, H. 1993, Sol. Phys., 148, 133.

Linker, J. A., Lionello, R., Mikić, Z., & Amari, T. 2001, J. Geophys. Res., 106, 25165.

Lites, B. W. & Skumanich, A. 1990, Astrophys. J., 348, 747.

Liu, C., Deng, N., Liu, Y., Falconer, D., Goode, P. R., Denker, C., & Wang, H. 2005, Astrophys. J., 622, 722.

Liu, C., Lee, J., Karlický, M., Prasad Choudhary, D., Deng, N., & Wang, H. 2009, Astrophys. J., 703, 757.

Longcope, D., Linton, M., Pevtsov, A., Fisher, G., & Klapper, I. 1999, in Magnetic Helicity in Space and Laboratory Plasmas, eds. M. R. Brown, R. C. Canfield, & A. A. Pevtsov (Washington: American Geophysical Union), 93.

Longcope, D. W., Fisher, G. H., & Pevtsov, A. A. 1998, Astrophys. J., 507, 417.

Longcope, D. W. & Pevtsov, A. A. 2003, Advances in Space Research, 32, 1845.

Longcope, D. W., Ravindra, B., & Barnes, G. 2007, Astrophys. J., 668, 571.

Longcope, D. W. & Welsch, B. T. 2000, Astrophys. J., 545, 1089.

Low, B. C. 2001, J. Geophys. Res., 106, 25141.

MacNeice, P., Antiochos, S. K., Phillips, A., Spicer, D. S., DeVore, C. R., & Olson, K. 2004, Astrophys. J., 614, 1028.

Magara, T. & Longcope, D. W. 2001, Astrophys. J. Lett., 559, L55.

Magara, T. & Tsuneta, S. 2008, PASJ, 60, 1181.

Martin, S. F. 1994, in Astronomical Society of the Pacific Conference Series, Vol. 68, Solar Active Region Evolution: Comparing Models with Observations, eds. K. S. Balasubramaniam & G. W. Simon (San Francisco: ASP), 68, 264.

—. 1998, Sol. Phys., 182, 107.

Martin, S. F., Bilimoria, R., & Tracadas, P. W. 1994, in NATO Science Series C, Vol. 433, Solar Surface Magnetism, eds. R. J. Rutten & C. J. Schrijver (Dordrecht: Kluwer), 303.

Martinez Pillet, V., Lites, B. W., & Skumanich, A. 1997, Astrophys. J., 474, 810.

Martres, M. J. 1989, Sol. Phys., 119, 357.

McIntosh, P. S. 1990, Sol. Phys., 125, 251.

McKenna-Lawlor, S. M. P., Dryer, M., Kartalev, M. D., Smith, Z., Fry, C. D., Sun, W., Deehr, C. S., Kecskemety, K., & Kudela, K. 2006, Journal of Geophysical Research (Space Physics), 111, 11103.

Mehltretter, J. P. 1974, Sol. Phys., 38, 43.

Metcalf, T. R., Leka, K. D., Barnes, G., Lites, B. W., Georgoulis, M. K., Pevtsov, A. A., Balasubramaniam, K. S., Gary, G. A., Jing, J., Li, J., Liu, Y., Wang, H. N., Abramenko, V., Yurchyshyn, V., & Moon, Y. 2006, Sol. Phys., 237, 267.

Mikic, Z., Barnes, D. C., & Schnack, D. D. 1988, Astrophys. J., 328, 830.

Min, S. & Chae, J. 2009, Sol. Phys., 258, 203.

Moon, Y., Chae, J., Choe, G. S., Wang, H., Park, Y. D., Yun, H. S., Yurchyshyn, V., & Goode, P. R. 2002a, Astrophys. J., 574, 1066.

Moon, Y., Chae, J., Wang, H., Choe, G. S., & Park, Y. D. 2002b, Astrophys. J., 580, 528.

Moon, Y., Choe, G. S., Wang, H., Park, Y. D., & Cheng, C. Z. 2003, Journal of Korean Astronomical Society, 36, 61.

Moore, R. L., Sterling, A. C., Hudson, H. S., & Lemen, J. R. 2001, Astrophys. J., 552, 833.

Muller, R. 1975, Sol. Phys., 45, 105.

Nindos, A. & Zhang, H. 2002, Astrophys. J. Lett., 573, L133.

Nindos, A., Zhang, J., & Zhang, H. 2003, Astrophys. J., 594, 1033.

November, L. J. & Simon, G. W. 1988, Astrophys. J., 333, 427.

Pallavicini, R., Serio, S., & Vaiana, G. S. 1977, Astrophys. J., 216, 108.

Pariat, E., Démoulin, P., & Berger, M. A. 2005, Astron. Astrophys., 439, 1191.

Park, S., Chae, J., & Wang, H. 2010, Astrophys. J., 718, 43.

Park, S., Lee, J., Choe, G. S., Chae, J., Jeong, H., Yang, G., Jing, J., & Wang, H. 2008, Astrophys. J., 686, 1397.

Pearce, G. & Harrison, R. A. 1990, Astron. Astrophys., 228, 513.

Penn, M. J. & Livingston, W. 2006, Astrophys. J. Lett., 649, L45.

Pevtsov, A. A. 2008, Journal of Astrophysics and Astronomy, 29, 49.

Pevtsov, A. A., Canfield, R. C., & Latushko, S. M. 2001, Astrophys. J. Lett., 549, L261.

Pevtsov, A. A., Canfield, R. C., & Metcalf, T. R. 1995, Astrophys. J. Lett., 440, L109.

Phillips, A. D., MacNeice, P. J., & Antiochos, S. K. 2005, Astrophys. J. Lett., 624, L129.

Priest, E. R. & Forbes, T. G. 2002, Astron. Astrophys. Rev., 10, 313.

Qiu, J. & Yurchyshyn, V. B. 2005, Astrophys. J. Lett., 634, L121.

Régnier, S. 2009, Astron. Astrophys., 497, L17.

Richardson, R. S. 1951, Astrophys. J., 114, 356.

Romano, P., Contarino, L., & Zuccarello, F. 2003, Sol. Phys., 218, 137.

—. 2005, Astron. Astrophys., 433, 683.

Rust, D. M. 1999, in Magnetic Helicity in Space and Laboratory Plasmas, eds. M. R. Brown, R. C. Canfield, & A. A. Pevtsov (Washington: American Geophysical Union), 221.

—. 2001, J. Geophys. Res., 106, 25075.

Rust, D. M. & Kumar, A. 1996, Astrophys. J. Lett., 464, L199.

Rust, D. M. & Webb, D. F. 1977, Sol. Phys., 54, 403.

Sakurai, T. & Hagino, M. 2003, Advances in Space Research, 32, 1943.

Sakurai, T., Shibata, K., Ichimoto, K., Tsuneta, S., & Acton, L. W. 1992, PASJ, 44, L123.

Scherrer, P. H., Bogart, R. S., Bush, R. I., Hoeksema, J. T., Kosovichev, A. G., Schou, J., Rosenberg, W., Springer, L., Tarbell, T. D., Title, A., Wolfson, C. J., Zayer, I., & MDI Engineering Team. 1995, Sol. Phys., 162, 129.

Schmieder, B., Hagyard, M. J., Guoxiang, A., Hongqi, Z., Kalman, B., Gyori, L., Rompolt, B., Demoulin, P., & Machado, M. E. 1994, Sol. Phys., 150, 199.

Schrijver, C. J. 2009, Advances in Space Research, 43, 739.

Schrijver, C. J., De Rosa, M. L., Metcalf, T., Barnes, G., Lites, B., Tarbell, T., McTiernan, J., Valori, G., Wiegelmann, T., Wheatland, M. S., Amari, T., Aulanier, G., Démoulin, P., Fuhrmann, M., Kusano, K., Régnier, S., & Thalmann, J. K. 2008, Astrophys. J., 675, 1637.

Schrijver, C. J., De Rosa, M. L., Metcalf, T. R., Liu, Y., McTiernan, J., Régnier, S., Valori, G., Wheatland, M. S., & Wiegelmann, T. 2006, Sol. Phys., 235, 161.

Schuck, P. W. 2005, Astrophys. J. Lett., 632, L53.

—. 2006, Astrophys. J., 646, 1358.

Schwenn, R. 2006, Living Reviews in Solar Physics, 3, 2.

Sivaraman, K. R., Rausaria, R. R., & Aleem, S. M. 1992, Sol. Phys., 138, 353.

Sofia, S., Heaps, W., & Twigg, L. W. 1994, Astrophys. J., 427, 1048.

Spirock, T. J., Yurchyshyn, V. B., & Wang, H. 2002, Astrophys. J., 572, 1072.

Stenborg, G. & Cobelli, P. J. 2003, Astron. Astrophys., 398, 1185.

Sterling, A. C. 2000, Journal of Atmospheric and Solar-Terrestrial Physics, 62, 1427.

Sterling, A. C. & Hudson, H. S. 1997, Astrophys. J. Lett., 491, L55.

Sterling, A. C., Hudson, H. S., Thompson, B. J., & Zarro, D. M. 2000, Astrophys. J., 532, 628.

Stix, M. 2004, The Sun: an introduction (Berlin: Springer Verlag).

Sturrock, P. A. 1966, Nature, 211, 695.

Su, J., Liu, Y., Liu, J., Mao, X., Zhang, H., Li, H., Wang, X., & Xie, W. 2008, Sol. Phys., 252, 55.

Su, Y., Golub, L., & Van Ballegooijen, A. A. 2007, Astrophys. J., 655, 606.

Tang, F. 1985, Sol. Phys., 102, 131.

Tian, L., Wang, J., & Wu, D. 2002, Sol. Phys., 209, 375.

Title, A. M., Frank, Z. A., Shine, R. A., Tarbell, T. D., Topka, K. P., Scharmer, G., & Schmidt, W. 1993, Astrophys. J., 403, 780.

Title, A. M., Tarbell, T. D., & Topka, K. P. 1987, Astrophys. J., 317, 892.

Török, T. & Kliem, B. 2005, Astrophys. J. Lett., 630, L97.

Tousey, R. 1973, Space Research XIII, Vol. 2, eds. M. J. Rycroft & S. K. Runcorn (Berlin: Akademic Verlag), 713.

Tran, T., Bertello, L., Ulrich, R. K., & Evans, S. 2005, Astrophys. J. Suppl. Ser., 156, 295.

Tsuneta, S., Acton, L., Bruner, M., Lemen, J., Brown, W., Caravalho, R., Catura, R., Freeland, S., Jurcevich, B., & Owens, J. 1991, Sol. Phys., 136, 37.

Tsuneta, S., Ichimoto, K., Katsukawa, Y., Nagata, S., Otsubo, M., Shimizu, T., Suematsu, Y., Nakagiri, M., Noguchi, M., Tarbell, T., Title, A., Shine, R., Rosenberg, W., Hoffmann, C., Jurcevich, B., Kushner, G., Levay, M., Lites, B., Elmore, D., Matsushita, T., Kawaguchi, N., Saito, H., Mikami, I., Hill, L. D., & Owens, J. K. 2008, Sol. Phys., 249, 167.

Uchida, Y. 1980, in Proceedings of the Japan-France Seminar on Solar Physics, eds. F. Moriyama & J. C. Henoux (Tokyo: Tokyo Astronomical Observatory), 83.

Ulrich, R. K., Bertello, L., Boyden, J. E., & Webster, L. 2009, Sol. Phys., 255, 53.

Švestka, Z., Fárník, F., Hudson, H. S., & Hick, P. 1998, Sol. Phys., 182, 179.

van Ballegooijen, A. A. & Martens, P. C. H. 1989, Astrophys. J., 343, 971.

Vršnak, B., Sudar, D., & Ruždjak, D. 2005, Astron. Astrophys., 435, 1149.

Waldmeier, M. 1938, Zeitschrift fur Astrophysik, 15, 299.

—. 1955, Ergebnisse und Probleme der Sonnenforschung (Leipzig: Akademische Verlagsgesellschaft Geest and Portig).

Wang, H., Ewell, Jr., M. W., Zirin, H., & Ai, G. 1994, Astrophys. J., 424, 436.

Wang, H., Jing, J., Tan, C., Wiegelmann, T., & Kubo, M. 2008, Astrophys. J., 687, 658.

Wang, H., Liu, C., Deng, Y., & Zhang, H. 2005, Astrophys. J., 627, 1031.

Wang, H., Liu, C., Qiu, J., Deng, N., Goode, P. R., & Denker, C. 2004a, Astrophys. J. Lett., 601, L195.

Wang, H., Spirock, T. J., Qiu, J., Ji, H., Yurchyshyn, V., Moon, Y., Denker, C., & Goode, P. R. 2002, Astrophys. J., 576, 497.

Wang, J., Zhou, G., & Zhang, J. 2004b, Astrophys. J., 615, 1021.

Welsch, B. T., Abbett, W. P., De Rosa, M. L., Fisher, G. H., Georgoulis, M. K., Kusano, K., Longcope, D. W., Ravindra, B., & Schuck, P. W. 2007, Astrophys. J., 670, 1434.

Wheatland, M. S. 2001, Sol. Phys., 203, 87.

Wheatland, M. S., Sturrock, P. A., & Roumeliotis, G. 2000, Astrophys. J., 540, 1150.

Wiegelmann, T. 2004, Sol. Phys., 219, 87.

Wiegelmann, T., Inhester, B., & Sakurai, T. 2006, Sol. Phys., 233, 215.

Wiegelmann, T., Thalmann, J. K., Schrijver, C. J., De Rosa, M. L., & Metcalf, T. R. 2008, Sol. Phys., 247, 249.

Wittmann, A. D. 1997, Sol. Phys., 171, 231.

Yan, X., Qu, Z., Xu, C., Xue, Z., & Kong, D. 2009, Research in Astronomy and Astrophysics, 9, 596.

Yashiro, S., Gopalswamy, N., Michalek, G., St. Cyr, O. C., Plunkett, S. P., Rich, N. B., & Howard, R. A. 2004, Journal of Geophysical Research (Space Physics), 109, 7105.

Yokoyama, T., Kusano, K., Maeshiro, T., & Sakurai, T. 2003, Advances in Space Research, 32, 1949.

Zhang, H., Ai, G., Yan, X., Li, W., & Liu, Y. 1994, Astrophys. J., 423, 828.

Zhang, J., Li, L., & Song, Q. 2007, Astrophys. J. Lett., 662, L35.

Zhang, Y., Tan, B., & Yan, Y. 2008, Astrophys. J. Lett., 682, L133.

Zhou, G. P., Wang, J. X., Zhang, J., Chen, P. F., Ji, H. S., & Dere, K. 2006, Astrophys. J., 651, 1238.

Zhukov, A. N. & Auchère, F. 2004, Astron. Astrophys., 427, 705.

Zirin, H. & Wang, H. 1993, Sol. Phys., 144, 37.

Zwaan, C. 1987, Annu. Rev. Astron. Astrophys., 25, 83.